INVESTIGATION OF WELD DEFECTS USING THERMAL IMAGING SYSTEM

INVESTIGATION OF WELD DEFECTS USING THERMAL IMAGING SYSTEM

By NIKHIL RAGHAVAN GUDURI, B. Tech

A Thesis Submitted to the School of Graduate Studies in Partial Fulfilment of the Requirements for the Degree Master of Applied Sciences

MASTER OF APPLIED SCIENCES (2021) McMaster University

Mechanical Engineering Hamilton, Ontario, Canada

TITLE: Investigation of Weld Defects Using Thermal Imaging System.

AUTHOR: Nikhil Raghavan Guduri,

B. Tech. (Mechanical Engineering)

SASTRA University, Thanjavur, India.

SUPERVISOR: Dr. Mohamed S. Hamed.

NUMBER OF PAGES: xv, 88.

Abstract

Continuous welding is one of the prominent techniques used in producing seamless piping used in many applications such as the mining and the oil and gas industries. Weld defects cause significant loss of time and money in the piping production industry. Therefore, there is a need for effective online weld defects detection systems. A laser-based weld defects detection (LBWDD) system has been developed by the industrial partner. However, the current LBWDD system can only detect some geometrically based weld defects, but not material inhomogeneity such as voids, impurities, inclusions, etc. The main objective of this study is to assess the predictability of a thermal imaging-based weld defects detection system (TIBWDD) using an IR camera that can be integrated with the current LBWDD system. The aim of the integrated detection system is to be able to detect a wider range of weld defects. A test rig has been designed and used to carry out a set of emissivity (ε) calculation experiments considering three different materials – Aluminum 5154 (Al), Stainless Steel 304L (SS), and Low Carbon Steel A131 (LCS) with two surface finishes 0.25 µm (FM) and 2.5 µm (RM), which are relevant to pipe welding operations. Al showed least change in ε varying from 0.162 to 0.172 for FM samples and from 0.225 to 0.250 for RM samples from 50°C to 550°C. LCS showed highest change in ε varying from 0.257 – 0.918 for FM samples and from 0.292 to 0.948 for RM samples. SS showed a consistent increase in ε for both FM and RM samples. Experimental and numerical analysis have been carried out mimicking two sets of possible weld defects investigating defect size, D_h, and distance between effect and sample surface, δ. Results showed that the δ based defects that are located within 3 mm can be detected by the IR camera. Defects with D_h = 1. 5 mm can be detected by the IR camera with and without glass wool. Laser welding simulations using 2D and 3D Gaussian heat source models have been carried out to assess the predictability of a set of possible weld defects. The heat source models have been validated using experimental data. Three sets of defects were considered representing material-based inhomogeneity, step and inclined misalignment defects. For material-based inhomogeneity in thin plates all defects located at 1.25 mm from the surface are found detectable as ΔT (temperature difference obtained on surface) > ΔT_{min} (detectability limit of TIBWDD system). For inhomogeneity defects in thick plates, except defects of 2.5 mm in square size all other defects were found detectable as $\Delta T > \Delta T_{min}$. All step misalignment defects were detected for thin and thick plates. In the case of inclined misalignment defects, for thin plates, the misalignment error in the thin plate had to be $\geq$ 0.275 mm to be detected. In the case of thick plates, the misalignment error had be $\geq$ 0.375 mm to be detected. Overall, results of the present study confirm that thermal imaging can be successfully used in detecting material-based and geometry-based weld defects.

Key Words: Laser Welding; Emissivity; Laser-based Weld Defects Detection System; Thermal-Imaging based Weld Defects Detection System; Gaussian Heat Source Model.

Acknowledgments

Firstly, I would like to take this opportunity to thank my graduate supervisor, Dr. Mohamed Hamed, for his trust, support, and guidance throughout my pursuit of master's degree at McMaster University. I am utmost happy and grateful that Dr. Hamed took me on as a master's student to work under his guidance and continued to have faith in me over the years.

Secondly, I would like to thank Mr. Greg Cooke, product manager at Xiris Automation Inc. for providing me with the thermal imaging camera which is an essential part of my experimental work. Also, I would like to thank Dr. Sumanth Shankar, for his guidance and support during my research amid the pandemic. I would also like to express my gratitude to The Department of Mechanical Engineering for their support which helped me achieve my goal.

Finally, I would like to thank my parents, and sister for all the support and sacrifice they did for me to have a good career and their constant support to achieve my goals and dreams.

Table of Contents

Contents

List of Tables

List of Figures

Chapter 1. **Introduction**

Pipelines are the most popular, economic, and efficient means of transportation of various fluids such as crude oil and natural gas, be it on land or seaways. They are essential for mankind to carry the fuel to warm their homes, drive their vehicles, or travel by plane, train, or bus. However, oil spills and pipeline leaks are encountered regularly at some places in the world. In the United States, since 1986 pipeline accidents have leaked an average of 76,000 barrels of oil per year [1]. This is equivalent to 200 barrels every day. These outbreaks not only cause a major impact on the economy but also harm human health. These spills contaminate the water bodies which pose a serious threat not only to human health but also to wildlife and marine culture. For instance, 70 barrels of an oil spill in the Baltic Sea led to the death of more than 60000 long-tailed ducks [2], whereas a 2,400 barrel spill of condensate in Alberta led to the extinction of a species of caribou and grizzly bear [3]. Hence there is an alarming need to cease these detrimental outbreaks for making the world a better place to live. According to the US department of transportation [1], poor welding/metal failure accounts for about 38% of pipeline spills. Lack of advanced welding technology and proper inspection systems are the main factors for pipeline failures. Welding methods and inspection technology had taken evolved from bronze-aged acetylene gas welding to modern laser welding. Thanks to advanced machines, modern computers, sensors, and dedicated software for making this possible.

Continuous pipe welding is one of the simple, variety specification, most efficient, and less equipment investment techniques used by pipe manufacturing industries. Fig. 1-1 shows the operational procedure of single seam pipe welding. Strength of these pipes depends on internal factors like material quality, welding method, weld parameters, and external factors like air humidity, working temperature, and power regulations. Weld defects can develop due to air voids, misalignment, and inhomogeneity in metal

that diminish the weld quality causing pipeline failures. Weld defects can be classified into geometry-based and material-based weld defects. Fig. 1-2 shows some of the commonly experienced weld defects.

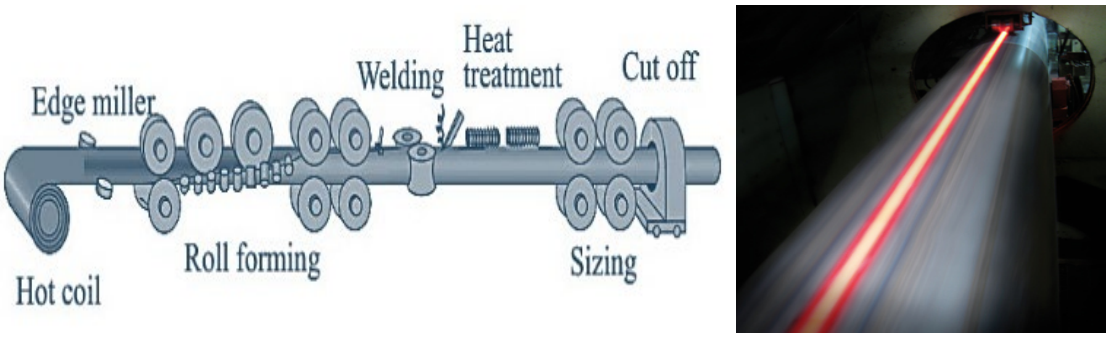

Figure 1-1: Schematic representation of continuous pipe welding operation [4].

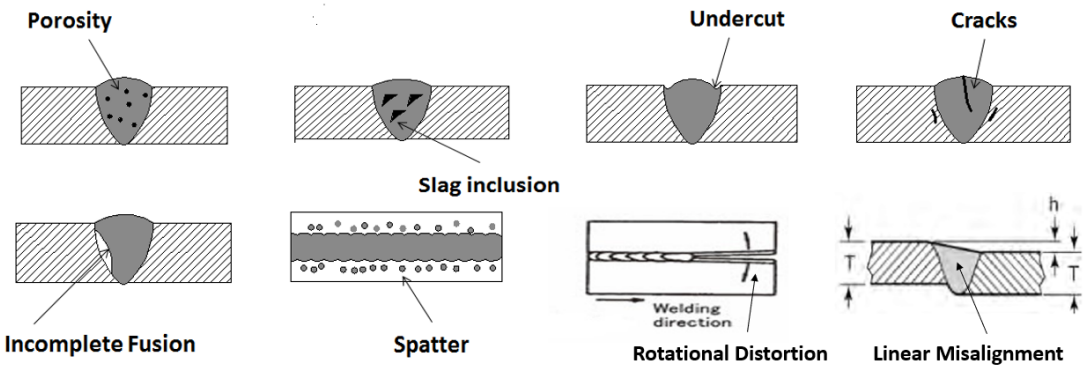

Figure 1-2: Common weld defects [5].

Stainless Steel (SS) is the most preferred metal for pipelines because of its significant resistance to oxidation than traditional Carbon Steel (CS) or Cast Iron. This promotes longer operating life for pipelines. In the first stage, the operation of single seam pipe welding begins with a hot coiled roll of SS passed through a series of rollers. Secondly, the two ends of the sheet metal are welded together by a welding unit, a gas torch, an induction coil, or a laser source. Subsequently, they are passed through sizing rollers to attain desired diameters and slashed for the required length. However, most commonly, inspection procedures are employed on the manufactured pipes in the final stage before packing as shown in Fig. 1-3.

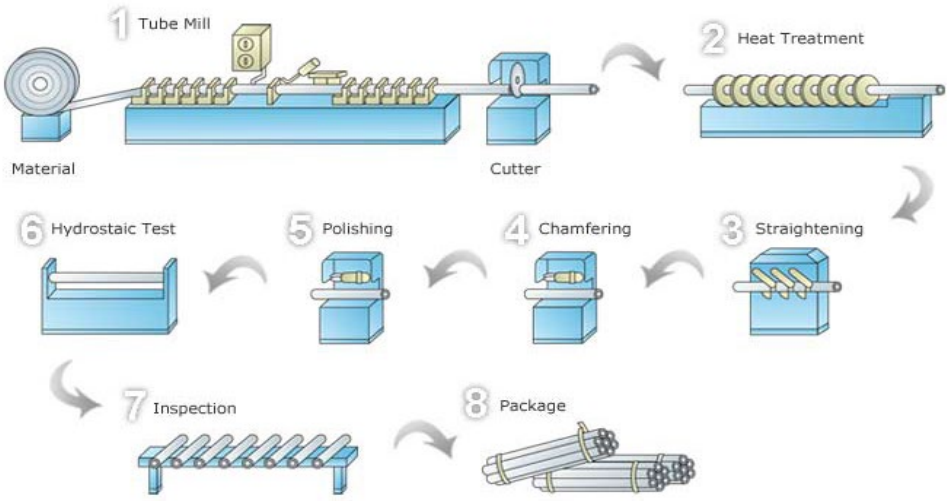

Figure 1-3: Flow chart of SS pipe manufacturing [6].

Therefore, identification of weld defects occurred during the welding stage is only carried out after production during the inspection phase, which results in rejects, significant scraping, and loss of time and money. Hence, there is a need to introduce an online weld quality monitoring system that would detect weld defects as they occur and implement online process adjustments to reduce rejects and scraping. Xiris Automation Inc., is a manufacturer of machine vision solutions for welding applications. They have developed a geometry-based weld defects detection system. Their Laser-based Weld Defect Detection (LBWDD) system is incorporated in laser-based pipe welding operations as shown in Fig. 1-4.

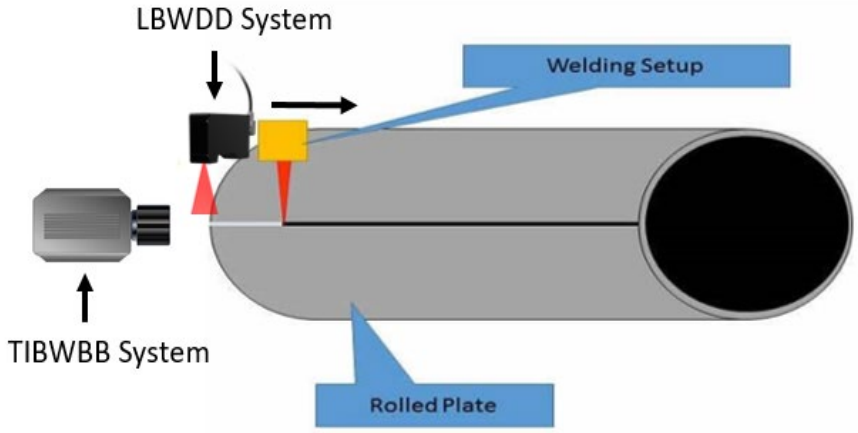

Figure 1-4: LBWDD System in single seam continuous pipe laser welding.

The LBWDD is only capable of capturing surface defects that are geometry-based, like spatter, undercut or surface cracks, etc. Nonetheless, it cannot capture in-metal material-based defects like porosity, incomplete fusion, or slag inclusion. Hence, there is a need for another inspection system to be incorporated along with the LBWDD system. Since the problem here is based on material inhomogeneity during welding temperatures, the use of a thermal imaging-based infrared system could be the right fit. Moreover, the advantage of using thermal imaging system over other techniques like ultrasonic or electromagnetic testing is that the thermal imaging-based infrared system is an online inspection method and it can identify the produced defects during the actual welding process unlike other techniques which identify defects during quality inspection check. Hence this technique would actually save a lot of time, cost and eliminate defects formation immediately during welding pipes. Therefore, an innovative weld detection system that incorporates a Thermal-Imaging based weld defect detection (TIBWDD) System along with the LBWDD system is proposed. Xiris Automation Inc. had a wide range of inspection systems and software designed for welding inspection. The proposed integrated system would incorporate an XI-400 Infrared Thermography (IRT) based weld spot finder camera and Xiris' WI3000 laser-based post-weld inspection system. Both are shown in Fig. 1-5 (a) and Fig. 1-5 (b).

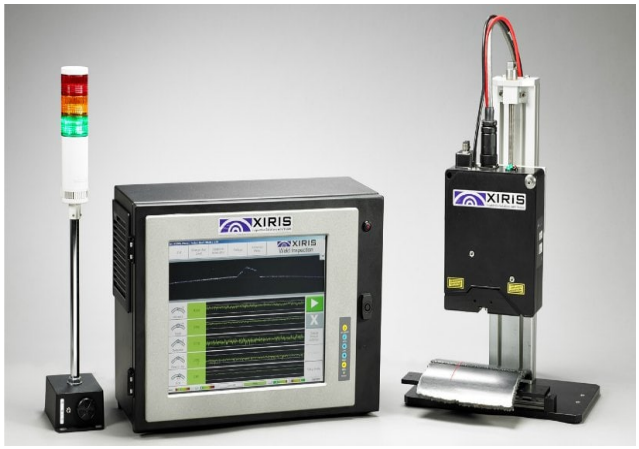

Figure 1-5 (a): Xiris WI3000 LBWDD System [7].

Figure 1-5 (b): Xiris XI400 spot finder camera [8].

IRT is used to record the real-time temperature field during the continuous welding operation. The thermographic data could be used to detect material-based weld defects. Emissivity is the principal quantity on which the working of the IRT camera depends. The accuracy of the thermal filed captured by the IRT depends on the correct emissivity value which depends on surface material, finish, and temperature. Usually, for temperature measurements using an IRT camera, the value of emissivity is assumed constant for the testing material. However, in real-time during welding, the molten metal undergoes drastic temperature changes, for example for SS temperature changes from 1450°C to 800°C in the first 10 seconds during the molten metal cooling phase. So, it is essential to evaluate the variation of the emissivity of the working material within the desired temperature range for acquiring precise thermographic data and images.

This thesis consists of six chapters starting with this Introduction chapter. Chapter 2 includes a literature review of previous work on the use of IRT in welding operations including defects detection and numerical modeling of welding operations. The main objectives of this study are presented in chapter 2. Details of the experimental setup used to calibrate the IR camera and validate the numerical results are presented in Chapter 3. Experimental work done for detecting geometry-based weld defects using the IR camera is presented and discussed in Chapter 4. Numerical work for detecting geometry-based defects and laser welding simulations based on Gaussian heat source models, their validation and use in investigating detectability thresholds of weld defects are presented in Chapter 5. Finally, a summary of the work carried in this study, the main conclusions and the recommendations for future work are covered in Chapter 6.

Chapter 2. Literature Review

In this chapter, a detailed review of existing research work done on IRT, calibration of IR camera, and use of it for defect detection analysis during welding operations is presented.

2.1 Infrared Thermography (IRT)

IRT is the method of utilizing an electronic device to measure thermal radiation emitted from a surface. The captured thermal image provides useful data about the thermal field, i.e., temperature distribution of the surface. IRT is one of the commonly employed Nondestructive Testing (NDT) techniques used for condition monitoring and quality maintenance. Maldague [9] provided a detailed introduction of the use of IRT in NDT. Maldague classified the application of IRT as passive and active. Passive thermography refers to the use of an IR camera without any application of external energy where there's already a noticeable temperature difference (hot/cold spots) on the object of interest. The best example for this is the thermal image used for building diagnosis shown in Fig. 2-1.

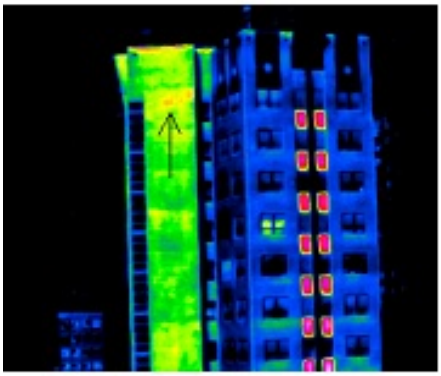

Figure 2-1: Passive thermal image used for building diagnosis [10].

Active Thermography refers to the use of an IR camera in applications where an external energy is used for thermal excitation. This external energy is necessary to generate a temperature contrast between the object and the hot or cold spots. The best example for this could be; application of heat on an inhomogeneous metal with internal flaws as shown in Fig. 2-2.

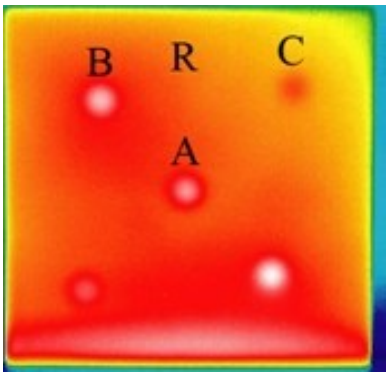

Figure 2-2: Subsurface defects on a metal plate being heated from behind [11].

There are many advantages and drawbacks when it comes to using an IRT camera for NDT. Some of the advantages are:

1) Faster Inspection rate;
2) Non-contact and no damage to test samples;
3) Safety (no high voltage equipment involved and no external radiation involved);
4) Easy to handle and results are universally interpretable (image format).

Contrarily, the drawbacks are as follows:

1) Thermal images depend on surface emissivity;
2) High cost of equipment;
3) Thermal losses due to conduction and convection might disturb thermal image;
4) Inspection is limited to the sample surface.

2.2 Calibration of an IR Camera

Calibration of an IR camera is the most important parameter to consider when using one. In real-time welding applications, the emissivity of the working metal depends on surface finish and temperature. So there is a need to have the right emissivity correlation for the metal over the desired range of temperature. So calibration of the IR camera is the primary requirement for its use in detecting welding defects. There had been some work carried out in the past regarding the calculation of temperature-

dependent emissivity graphs for various metals. Barreira et al. [12] measured the emissivity of ten different materials using a black tape of fixed known emissivity. Their study compared the emissivity results found using an IR Camera and an Emissometer. The differential thermopile emissometer camera used consisted of two thermopiles (black and reflective) for total hemispherical emittance measurement. In this experiment, the black tape used for reference was Scotch 3M +33 Super, of emissivity 0.90. They glued the tape onto the surfaces of various materials and heated them up to about 70°C for 24 hours. Later, the samples were placed in enclosed cardboard (to minimize reflection) with one open side. Each material was placed on a flat surface and emissivity was measured along with a standard emittance surface for calibration. Results showed that similar emissivity values were obtained using both IR camera and Emissometer except for stainless steel; that may be due to high reflectivity and low emissivity characteristics of steel which affected results of the IR camera. The average working temperature in this experiment was between 57°C and 69°C.

Wen et al [13], build an experimental rig to test the effects of surface roughness on emissivity of surfaces made from aluminum alloys. Four cartridge heaters controlled by a variable voltage transformer were used to heat a large aluminum block insulated with ceramic fiber. Thermocouples were used to measure the temperature of the test plate 1 mm below the surface, and the temperature gradient between the surface and thermocouple was neglected due to aluminum's high thermal conductivity. A fast-infrared array spectrometer (FIAS) was used to measure wavelengths and radiation intensity. All measurements were recorded when the sample has reached a steady state.

Lui et al [14] experimentally investigated the emissivity of surfaces made from various SS grades – 201, 304, and 321. All tests were conducted at a temperature in the range of 750K – 1150K at different heating times. The heating times were varied between 1 to 10 hours using a blackbody furnace. Two IR thermometers were used during the test, one was used to determine the emissivity of the blackbody (furnace wall), and the other was used to calculate the emissivity of the test sample. The spectral range

of the IR thermometer used in the test was 1.5 μm. The results showed that the emissivity of the samples increased with an increase in the heating time which was attributed due to oxidation layer formation. The heating time had a noticeable effect on the change of emissivity for the initial 3 hours of heating, however, it was negligible later on. A correlation between emissivity and temperature was developed. However, no data on the surface finish was provided. The results of the SS 321 sample showed a highest value of emissivity, however, no information was provided on the reason.

Wang et al. [15] investigated variation of the emissivity of steel and graphene with temperature and surface finish. The experimental setup used for this study involved the use of a high-frequency induction heater to produce dynamic heating conditions up to 1400 K. Using a Zn-Se lens and other mirrors, thermal radiation was guided towards a Fourier transform infrared (FT-IR) spectrometer. The surface temperature of the sample was first calculated by the multi-wavelength method used by the FT-IR spectroscopy and identified that the results were consistent with measurements taken from a two-color pyrometer. Based on the results, the normal emissivity of oxidized steel was about 0.76 and 0.91 for graphene. This value was used in the heat transfer analysis to determine the power required to heat a metal plate to 900°C.

2.3 Application of IR Camera in Welding Operations

U. Sreedhar et al. (2012) [16] conducted a study on online weld defect detection using thermal imaging technique on weld sections of a 9 mm thick plate made from Aluminum Alloy 2219 (AA2219). Their main objective was to detect the in-weld defects using IR camera placed at 60° normal of the plate surface. Multi-pass Tungsten Inert gas (TIG) welding was employed in their work. The thermal images were taken at the weld and steel clamp sections. The temperature distribution of the field of view varied from 76°C to 107°C and defects could be identified as hot spots due to non-homogeneity. No information on the working temperature of the weld section was provided. They compared their IR images with X-ray images

for qualitative defect detection. They developed an online technique to detect weld defects during TIG welding.

Glenn Washer et al. [17] investigate the use of IRT for NDT of steel welds. Specimens with induced defects and specimen manufactured with actual defects were tested with various heating techniques. Toe crack, lack of fusion, slag inclusion defects with varying size and depth were placed at known positions to calibrate the various testing systems and determine the optimum one. They tested various designs using IR cameras and resistive heaters. Thermal images were captured along the cooling time of the fresh weld joint from 700 F to 250 F by Conventional IR and IR- Ultra Time Domain (UTD) and the results were compared. Their results showed that the defects were more evident when a thermal gradient was applied along the weld section rather than uniform heating. IR-UTD detected more prominent defects with more accuracy than conventional IR.

Shen et al. [18] used IRT in detecting defects in high-pressure steam pipes. Defects were manually introduced. They used a thermal video system, TVS-2100. The operating temperature of the experiment was -40°C to 950°C. The frame rate was 30 frames per second. They tested a stainless steel pipe and three 20 carbon steel pipes of varying diameters with different holes drilled into the inner surface. Hot steam at 150°C was allowed to flow at 3 MPa in all of the four pipes. Thermal images were recorded and defects were identified. They also performed the same test with a cooling refrigerant employed on the outer surface to get better thermal contrasts in the image for more accurate defect detection. They found that the larger the thickness of the plate, the more time it took for detects to emerge. Thus, they considered the pipe thickness as a key factor affecting the IRT testing. Moreover, the testing sensitivity time for steel was around two minutes for detects to emerge, while it took only 30 sec for carbon steel, which meant the lower the thermal conductivity, the higher the sensitivity, and the higher the time needed for the detects to emerge. Comparing the results between inside heating and outside cooling, it was found that defect detecting sensitivity was higher for the former than the latter. Their results proved that the IRT

testing on pipes was safe to use for detecting defects caused by corrosion and flow erosion. On the contrary, the used method was not efficient in detecting inner defects at steady-state temperatures.

Schaumberger et al. [19] studies weld seam defects in copper within laser beam welding applications. The main challenge was copper high reflectance and high thermal conductivity. Temperature gradients around the pores vanished quickly, making it harder to detect minor defects. Their work was limited to identifying defects with a minimum diameter of 0.5 mm. Venkatraman et al. [20] used IRT in detecting incomplete penetration and depth estimation within TIG welding. To detect incomplete penetration, they performed a butt welding operation and used an IR camera capturing images along the rear end of the weld direction. The voids due to improper penetration created significant temperature gradients which was identified by IRT. In order to determine depth of penetration, they used plates with variable thickness. They showed that a complete penetration would cause a larger weld area of high temperatures, whereas a weaker penetration would create a smaller weld are with lower temperatures.

Shrestha Ranjit et al. [21] performed IRT technique on a stainless steel plate with holes of varying diameters and depths. They performed Finite element (FE) simulations at the same input thermal excitation frequencies employed in their experimental work, from 0.021 Hz to 0.182 Hz. They analyzed their experimental thermal data of the entire surface using an image processing technique using MATLAB. Their experimental results showed that the defects were not visible at the high frequency of 0.182 Hz. However, they were visible at the lower frequencies. On the contrary, defects were detectable in their FE results for all frequencies. However, better results were obtained at lower frequencies. They also indicated that better detectability can be achieved for defects with a radius to depth ratio of 1 or more.

2.4 Numerical Modelling of Welding Procedures

Numerical modeling is very popular in manufacturing processes and product development. The principal factor for its popularity is the demand for industries to increase their production, the efficiency of quality

standards, and getting better control over the regulation of various process parameters. Numerical modelling can be a powerful tool for the manufacturing and design engineers in optimizing parameters like heat flux, applied forces and thermal losses, etc.; during different phases of steel components production like welding, molding, forging, and casting. Simulation of welding operations is very complex and involves the concept of multi-physics analysis (thermal, structural, electro-magnetic, etc.). The common challenges that are usually encountered when performing numerical modelling of welding operations are:

1. Finding and using a model of the heat source that is valid and representative of the respective welding method (Laser, Arc, Induction welding, etc.).
2. Simulation of time-dependent welding operations is computationally more expensive.
3. The need of proper boundary conditions that represent real-time convective and radiation losses at the sample boundaries during the welding operation.
4. The need to consider temperature-dependent material thermos-physical properties.

The movement of the heat source used for welding (e.g., a laser beam) is usually fast, continuous, and smooth. Various mathematical models have been developed to simulate a volumetric heat flux moving along the welded surface. The first model was developed by Goldak et al. [22] which was double ellipsoidal in shape. They validated the resulting numerical temperature distribution using their heat flux model experimentally. Their results showed that their proposed heat source model was able to simulate temperature fields corresponding to deeply penetrated welds.

Capriccioli et al. [23] carried out numerical simulations of TIG and Laser root filling welding operations. Material properties of AISI steel for the TIG and INCONEL 625 for the Laser welding operations were considered. The heat-affected zone was analyzed.

Prasad et al. [24] carried out a numerical investigation of TIG welding of stainless steel pipes using ANSYS APDL. They investigated residual stresses developed due to the welding operation. The double ellipsoidal

heat source distribution model developed by Goldak et al. [22] was used. The welding parameters and material properties along the working temperature conditions were considered. Radiation and Convection losses along the weld joint and the adjacent pipe surface were simulated using the combined heat transfer coefficient for radiation and convection proposed by Dean Deng et al. [25] Experiments were performed and results were compared with the experimental data. Their numerical results were in good agreement with the experimental data.

Suresh Akkela [26] numerically investigated welding of dissimilar metals, 304 steel and copper, which is used in heat exchanger joints. Thermal analysis followed by structural analysis was carried out using ANSYS. A Gaussian heat flux distribution was used to represent a welding heat load of 2000W at the weld joint. Residual stresses were analyzed for the bimetallic joint.

Nikanorov A et al [27] simulated induction tube welding. This study had made a prominent contribution to induction welding simulations. To simulate a quasi-steady state coupled electromagnetic and thermal fields, a special algorithm for coupling the electromagnetic and thermal processes in space and time was implemented. The Joule heating due to the electromagnetic field was used as a moving heat source. Temperature-dependent electro-physical properties were used. Convection and radiation losses through all surfaces were considered. Two models namely full and local models were generated. The full model simulated the actual induction welding operation using coil, air for magnetic medium, impeder and tube. The local model used only air and tube with v angle, where pipes are welded by conduction from electric current. The results concluded that the full model is useful for optimizing induction heating parameters and geometry Whereas the local model is useful for studying temperature profiles near weld joints and computationally less expense than full model.

The literature review presented here confirms that Infrared thermography (IRT) can be used to detect material-based weld defects. However, the ability of IRT to detect material-based weld defects heavily depends on two factors: (a) the accuracy of the captured thermal image and (b) the detectability of these

defects. The first factor depends on the accuracy of the emissivity information of the welded surfaces. Therefore, one must have accurate correlations of the emissivity of relevant materials and surface finishes. The second factor depends on the type and size of the weld defects. Therefore, their detectability limits or threshold must be investigated and determined. Having said so, the main objectives of the present study are as follows:

1. Develop an experimental facility that can be used to calibrate thermal images captured by the IR camera, considering various materials and surface finishes of interest. The desired outcome of this objective is to develop a set of correlations of surface emissivity as function of surface temperature, material and surface finish. Experimental data will also be used to validate numerical results serving the second objective discussed below.
2. Examine detectability thresholds of a number of possible material-based weld defects using IRT. Since performing real-time laser welding operations is not possible in the lab, numerical simulations of such operations will be carried out using ANSYS-Mechanical as a viable alternative. Numerical simulations will be used to carry out a parametric study of investigating defects detectability thresholds.

Chapter 3. **Determination of Emissivity Correlations**

Xiris Automation Inc. is a developer of machine vision products for weld quality laser-based monitoring systems. They currently assess welds for arc, laser, and high-frequency induction welding, based on geometrical features, which are limited to detecting geometry-based weld defects. By integrating thermal imaging using Infrared Thermography (IT) their system will be able to detect material-based weld defects caused by material inhomogeneity, voids, etc. However, a known emissivity value must be inputted into the IR camera in order to obtain accurate surface temperature profiles. Emissivity values of material vary with temperature and surface finish.

The various materials, surface finishes and operating temperature ranges considered in this study are listed in Table 3-1. These particulars have been selected in consultation with the industrial partner. They are considered to be the most commonly encountered materials, finishers and temperature ranges in the manufacturing of single seam pipes.

Table 3-1: Various materials and surface finishes considered in this study.

Material	**Surface Roughness (µm)**		**Temperature Range**
	Fine Machined	*Rough Machined*	
Aluminum, 5154 Alloy	0.25	2.5	50°C – 550°C
Stainless Steel, Grade 304L	0.25	2.5	50°C – 800°C
Low Carbon Steel, ASTM A131	0.25	2.5	50°C – 800°C

The material samples used for this experiments were named as follows:

1. Aluminum 5154 Alloy (Al): Fine Machined (FM-Al), Rough Machined (RM-Al),
2. Stainless Steel 304L (SS): Fine Machined (FM-SS), Rough Machined (RM-SS),
3. Low Carbon Steel A131 (LCS): Fine Machined (FM-LCS), Rough Machined (RM-LCS).

3.1 Experimental Setup

3.1.1 Overview

The goal is to build a test rig to calculate temperature dependent emissivity correlation for various materials using the IR camera. Figure 3-1 shows the schematic diagram of the test setup. High-temperature heating cartridges rated for working temperatures till 800°C were used as heater as they consist of direct heating, which is very efficient highly efficient, reusable, and cost-effective. Two standard K type ungrounded thermocouples TC1 and TC2 were attached to the sample surface. TC1 is connected to a controller box which gives a feedback signal to VARIAC if the sample temperature is reached to the input given. TC2 connected to sample surface is connected to the Data Acquisition System (DAQ). DAQ is used to convert the electrical signal generated by TC2 to a temperature reading which can be monitored by a PC. VARIAC or variable transformer serves the purpose of converting the voltage from power supply to the voltage rated for the heater. The IR camera is connected to a PC and the recorded thermal images are studied using PIX Connect software.

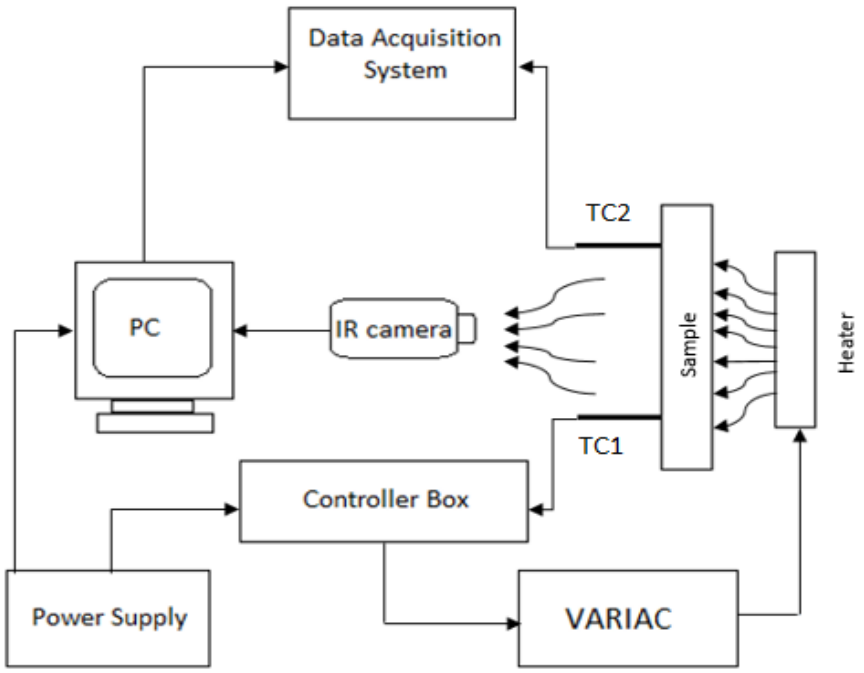

Figure 3-1: Details of the experimental test setup.

Firebricks are used as a primary source of insulation and base as they are inexpensive and highly energy efficient. Firebricks were used to house the test samples and were placed on all sides except for the front side that will be facing the IR camera as shown in Fig. 3 2. This minimizes the heat transfer between the samples and the surroundings. The IR camera is placed on a T-Bar sliding mechanism at a distance of 9-11 cm away from the test area to get clear focus on the test samples. A cooling system was used to protect the lens from the damage than can be caused by high working temperatures.

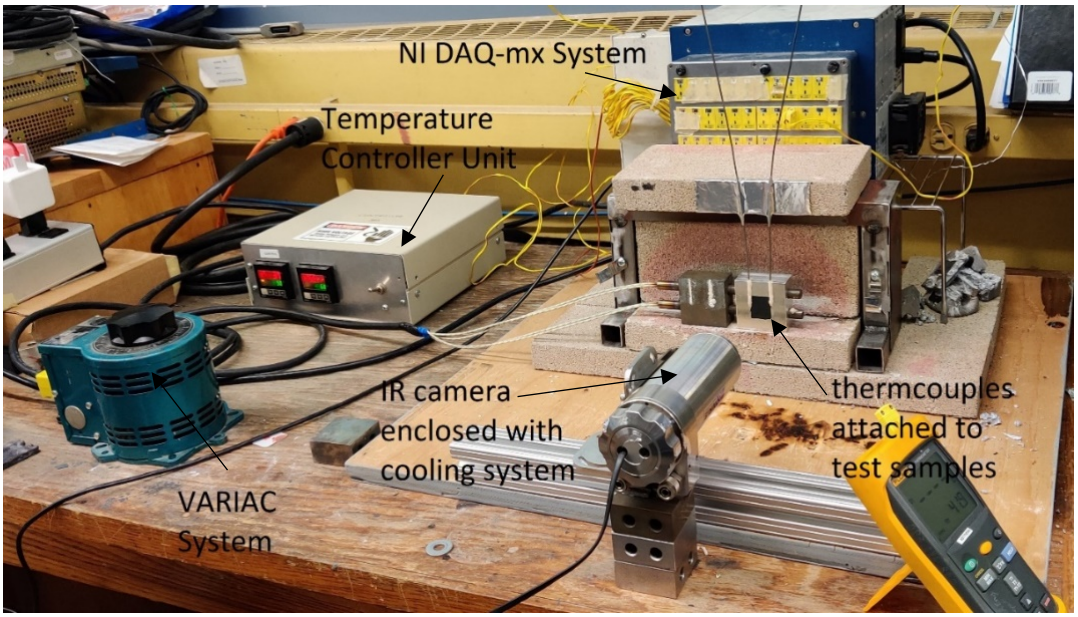

Figure 3-2: The experimental setup used for emissivity determination.

3.1.2 Sample Specifications

Figure 3-3 shows the sample dimensions with drilled holes to space the heating cartridges to get effective heat distribution along with the samples. At high temperatures, the heating cartridges may be constrained or become too loose in the test piece drilled holes after testing due to thermal expansion. The maximum interference of heat expansion of the holes was used to select a proper hole fit to ensure that heat cartridges would not be stuck for any of the tests. The ISO System of Limits and Fits (Tolerances) was used to determine the standard hole size for the test piece. To ensure the removal of the heat cartridges after heating test pieces, free-running clearance fits were selected for each test piece.

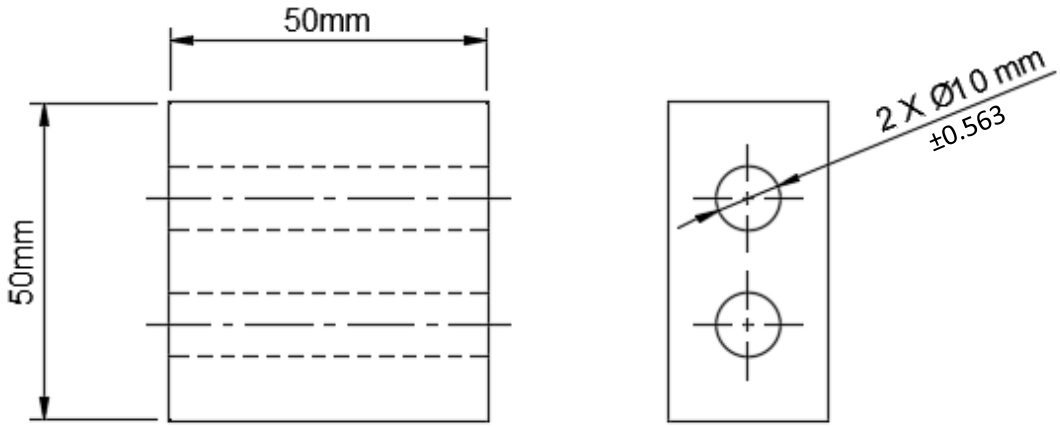

Figure 3-3: Front-view (left) and side-view (right) of test sample.

Each sample was machined on the test surface as per the required surface roughness values as per ANSI standards using a portable surface roughness tester [28]. The average value of roughness obtained over the test area of each sample is listed in Table 3-2 were in agreement with ones in Table 3.1.

Table 3-2: Surface Roughness of test samples

Material	**Average surface roughness obtained (µm)**	
	Fine Machined	*Rough Machined*
Aluminum, 5154 Alloy	0.2489	2.5087
Stainless Steel, Grade 304L	0.2516	2.4962
Low Carbon Steel, ASTM A131	0.2568	2.5428

3.1.3 Camera and Cooling System

The XI 400 IR camera was provided by the industrial partner. Specification of the IR camera are provided in Table 3-3.

Table 3-3: Specifications of the XI-400 IR camera

Technical Details of XI 400 IR Camera	
Temperature range	Scalable via software • -20°C – 100°C • 0°C – 250°C • 150°C – 900°C
Ambient Temperature	0°C – 50°C

Spectral range	8 – 14 µm
Optical Resolution	382 x 288 pixels
System Accuracy	± 2°C or ±2%
Spot Detectability Threshold	2°C or 2%
Noise Equivalent Temperature Difference (NETD)	80 mK
Relative humidity	10 – 95 %, non-condensing
Measuring Distance	9 – 12 cm away from lens

The IR camera was placed at a distance of 9-12 cm away from the test samples in order to obtain the best resolution and in-detail images. The maximum temperature of the camera should not exceed 50°C. A test was conducted where a SS sample was heated up to 800°C using three standard K type ungrounded immersion probe thermocouples namely TC1, TC2 and TC3. Thermocouple TC1 was used to measure temperature on the SS sample connected to the temperature controller box. Temperature on the SS sample was recoded using a Data Acquisition System (DAQ) with thermocouple TC2 attached to it. A steel plate mimicking the IR camera was placed at a distance of 9 cm is shown in Figure 3-4. Thermocouple TC3 was attached to the steel plate to monitor its surface temperature, which represents the temperature that IR camera would be exposed to.

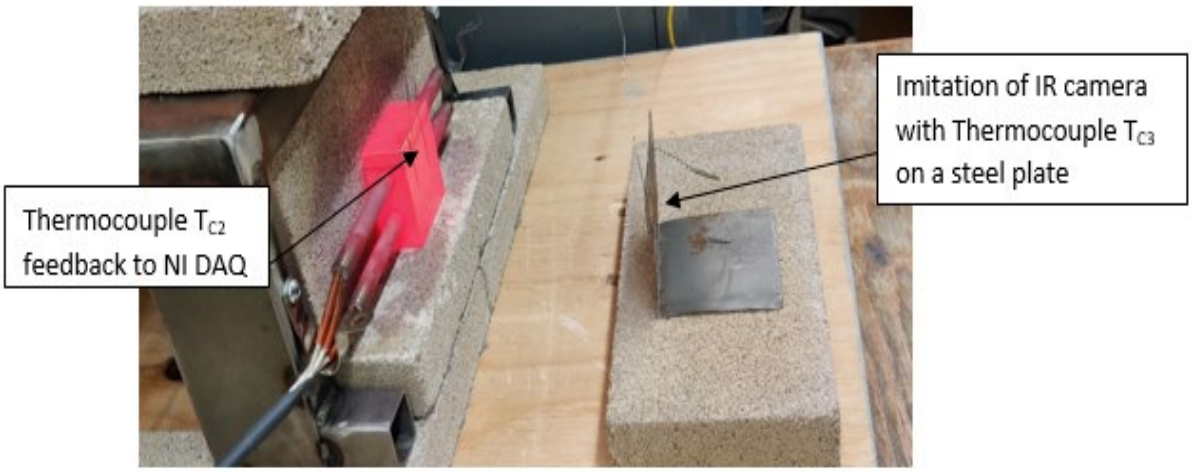

Figure 3-4: Testing maximum temperature the IR camera is exposed to.

Figure 3-5 shows the temperature-time curve for the sample and the steel plate during the heating phase. Steady-state temperature data was obtained every 100°C.Results showed that the camera would be exposed to a 120°C temperature which exceeds the maximum limit of 50°C.

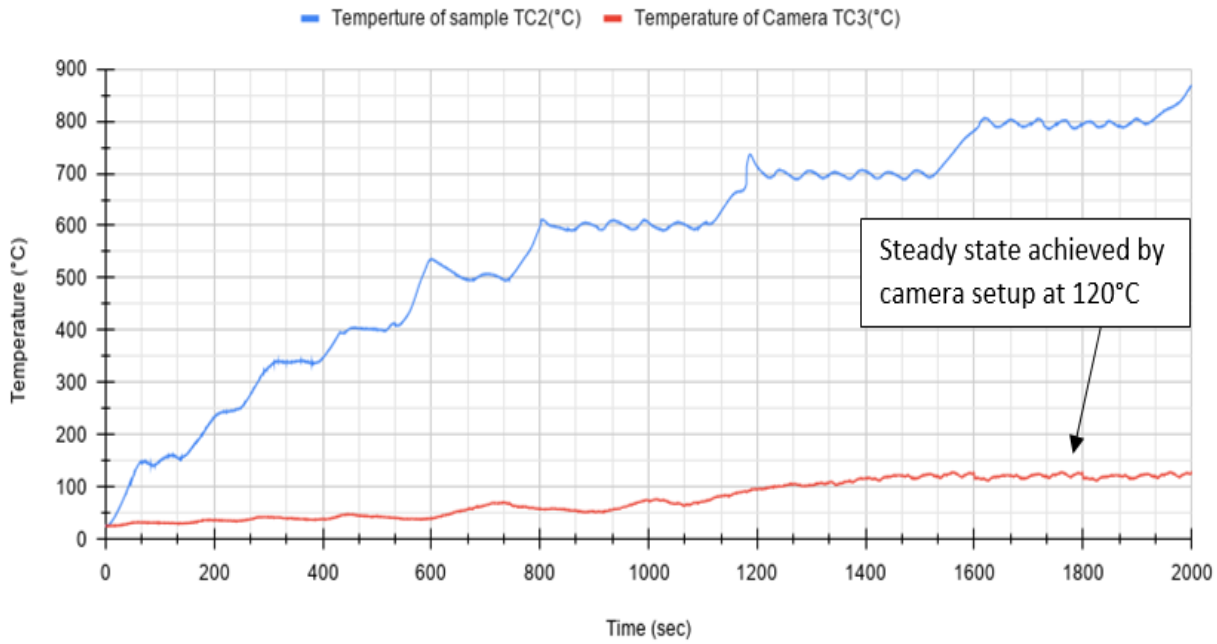

Figure 3-5: Temperature distribution graph during trail test

Therefore, a cooling system had to be used to protect the IR camera. The industrial provided a camera cooling assembly, which was used in all tests. The following parameters shown in Table 3-4 were set in-camera software – Pix Connect; for all the emissivity calculation tests. Temperature data were recorded using an initial reference emissivity of 1.0 which was then adjusted to the right emissivity value as per the thermocouple readings. The emissivity graph was plotted for every 50°C covering the desired temperature range for each sample.

Table 3-4: Parameters used during emissivity testing

Parameters used during Emissivity Test	
Temperature range	Scalable via software • -20°C – 100°C • 0°C – 250°C • 150°C – 900°C

Reference Emissivity	1.0
Ambient Temperature	22°C
Color Palette	Iron
Measuring distance	11 cm
Relative humidity	60 % (obtained through local weather report)

3.1.4 Power Supply Assembly

Specifications of cartridge heaters are listed in Table *3-5* specified below. To achieve steady-state conditions during heating the samples and also to regulate the power supply to the cartridge heaters a variable transformer (VARIAC) rated at 1.4 KVA, with a 120V input voltage delivering an output voltage of 0-120V and 10 A was used. The power was regulated in order to achieve the desired sample surface temperature using a temperature controller.

Table 3-5: Heater Cartridge Specifications.

Diameter (in)	Sheath length		Watt density		Voltage (V)	Wattage (W)
	in	*mm*	W/in^2	W/cm^2		
3/8	5	127.0	96	15	120	500

3.1.5 Thermocouples Positioning on Sample Surface

Two standard K-type ungrounded thermocouples with a working temperature range of 0 – 920°C were used to measure the temperature of the test sample surface. To secure the thermocouples on the sample surface, two grooves of 2 mm wide and 25 mm length were machined onto the test piece surface in order to embed the thermocouples flush onto the sample surface. High-temperature thermal cement was used to affix the thermocouple on place. Details of these grooves are provided in Figure 3.6. The slits were machined symmetrically at a fixed distance of 15 mm from the side edges of the samples considering the test areas as shown in Figure 3-6. One thermocouple TC1 was connected to the temperature control unit

to control the power input to the cartridge heaters while the other thermocouple TC2 was attached to the DAQ system to collect the sample surface temperature.

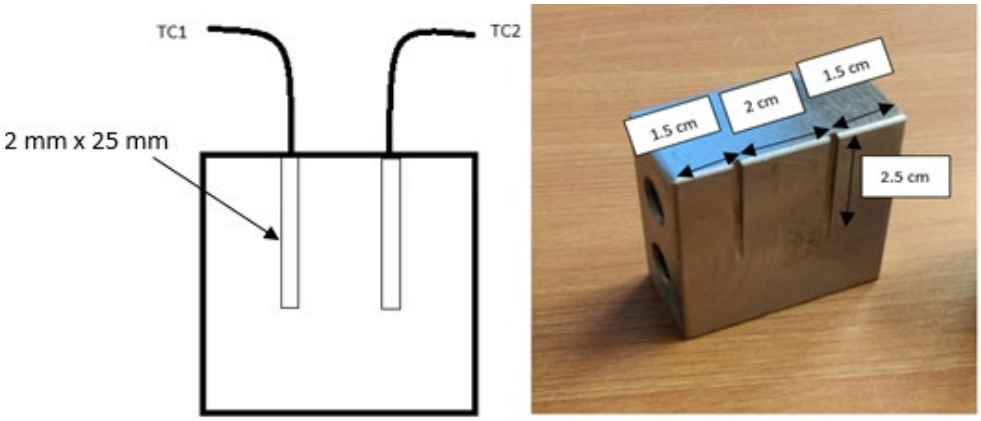

Figure 3-6: Details of grooves used to affix thermocouples to test sample surface.

3.1.6 High-Temperature Emissivity (ε) Paint

In order to determine surface emissivity, a surface with a reference known emissivity is needed. Part of the test sample was painted using a ceramic-based high-temperature high emissivity coating paint that has a working temperature up to 1316°C. The coating is made by Aremco [29]. This ceramic-based paint resembles a black body surface with ε = 1. Since the measuring area of IR camera is restricted to a 4 cm x 4cm area, the an area of 2cm x 2cm was coated with the paint leaving the other uncoated area to measure the test sample emissivity, as shown in Figure 3-7.

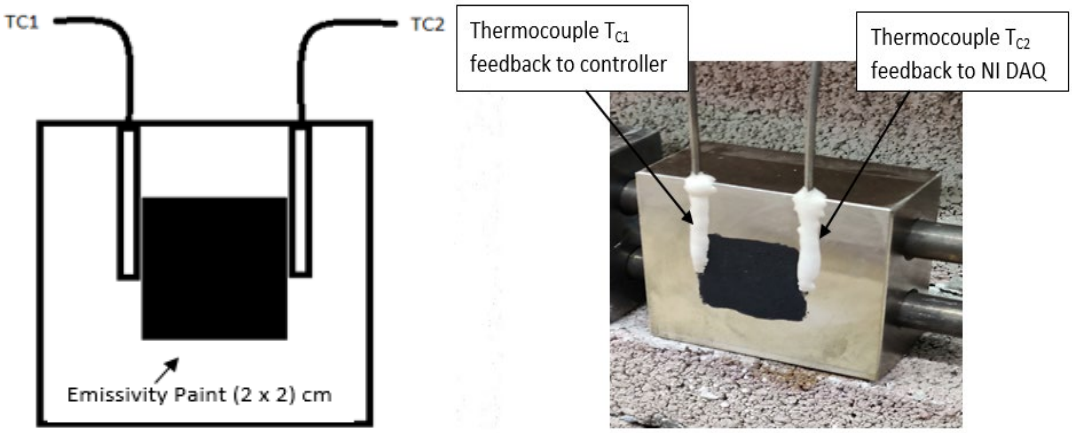

Figure 3-7: High emissivity ceramic coating area with thermocouple positions.

All the metal surfaces of the samples were cleaned to ensure they are free from itching agents and dust particles. Once coated, all samples were left overnight to air dry. The coating was then cured by placing all samples in a furnace and heating them up to 200 °F (93 °C), final curing was achieved at 500 °F (260 °C) for 2 hours. Samples were left inside the furnace till they cooled down to room temperature. Curing the paint is very important as liquid particles must evaporate completely. Curing is very important for ceramic-based coatings, as it affects the emissivity value and durability of the coating. The sample surface with the bare area was later cleaned with a rust removal agent as curing will leave oxidized metal on the surface which would affect the emissivity of the uncoated surface.

3.1.7 Data Acquisition System

A National Instruments (NI) DAQ-MX system was used to record the temperature data from the thermocouples. A LABVIEW program was used to record and monitor all data. Temperature data was collected every 0.1 sec.

3.1.8 Uncertainty of Instruments

Experiments are always driven by a certain amount of uncertainty with instruments or devices used. This uncertainty in results is referred to as an error. It is classified in two – Schematic errors and Random errors. Schematic errors are the ones that result from instruments that are not calibrated, which can be constantly large or small. These errors can be terminated by using a standard device or instrument for pre-calibration. Random errors on the other hand are the ones, which can fluctuate unpredictably from one value to other. These errors are mostly likely avoidable, but can be close to true value of measurement. In the experiment conducted for determining the emissivity correlations, all the devices are properly calibrated and errors were minimized as follows:

1. Standard K type ungrounded thermocouples used are batch calibration certified. Ungrounded thermocouples are used as experiments conducted are steady state and they have less noise

when compared to grounded thermocouples. So the readings recorded by them are highly accurate, and does not have any schematic or random errors.

2. NQ-DAQ system was used to measure the electric signal generated by the thermocouple, amplify it and convert into a temperature unit. However, during this conversion, a signal-to-noise error is created, which can cause a maximum random error of about 2%. This can be due to presence of dust particles near thermocouple terminals or female ports in DAQ system. These ports are regularly cleaned and calibrated for every 50°C till 1000°C to obtain accurate readings using a standard K type thermocouple.
3. The IR camera used can contribute a schematic error of ±2% as given by the specification sheet. However, when recording temperature and emissivity correlations, high temperature ceramic paint of known emissivity is used for reference to maintain accuracy in readings. Also the temperature values recorded by IR camera are evaluated with the readings of two standard K type thermocouples placed on the test samples, so that emissivity determined is accurate.

3.2 Results and Discussion

3.2.1 Emissivity Measurement Procedure.

The goal of the experiment is to determine emissivity of the coated and uncoated sample surfaces. Emissivity was measured at two uncoated (left and right) areas, UCL and UCR, which are 3 mm x 10 mm each located as shown in Fig. 3-8. Three coated (left, center and right) areas, CL, CM, and CR, which were 2 mm X 2 mm each. The uncoated areas are located at a distance of 5 mm from the thermocouple slits, and the coated areas are located 3 mm from each other so as to ensure that all the areas are at the steady-state condition when measuring temperatures and determining emissivity. All areas were given a reference value of ε=1 at the start of each test. Once the sample is heated and reached a steady state temperature at every 50°C, as indicated by TC1 and TC2, the emissivity value of all areas was adjusted

until the temperature reading of the IR camera was equal to the temperature recorded by TC1 and TC2. Hence, the emissivity of each area was determined.

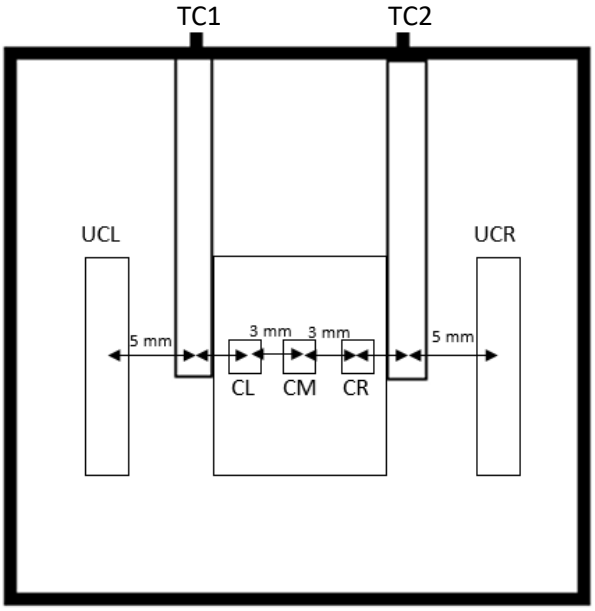

Figure 3-8: Coated and uncoated areas at which emissivity is measured on sample surface.

3.2.2 Emissivity for Aluminum Sample

The test was conducted for both the FM-Al and RM-Al sample. The emissivity values were determined as explained above using thermocouple readings and the IR camera Pix Connect software. Fig. 3-9 shows the thermal image captured for the FM-Al sample at 150°C. Data was obtained at every 50°C staring from 50°Cup to 550°C. Results are presented in Table 3-6 and Table 3-7 for the FM and RM samples, respectively.

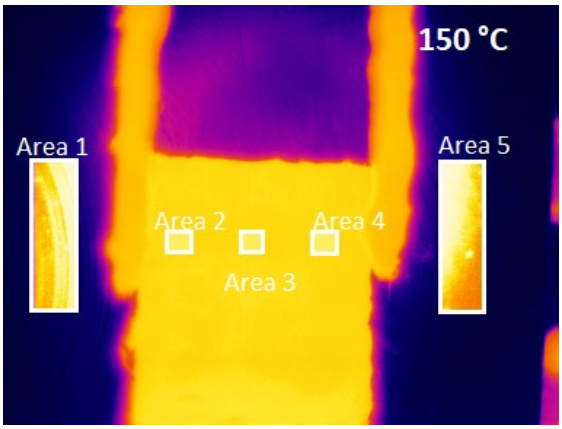

Figure 3-9: IR Image showing measure areas considered on FM-Al sample at 150°C.

Table 3-6: Emissivity data obtained for the FM-Al sample.

Scalable temp in software	TC1 (°C)	TC2 (°C)	Avg T at coated areas (°C)	Avg ε at coated areas	T at uncoated areas (°C)			ε at uncoated areas		
					UC1	*UC2*	*Avg*	*UC1*	*UC2*	*Avg*
(-20/100)°C	50	50	50.1	***1***	50.5	49.7	***50.1***	0.173	0.151	***0.162***
	100	100	100.2	***0.951***	100.9	99.6	***100.2***	0.101	0.094	***0.098***
(0/250)°C	151	150	149.9	***0.934***	150.6	149.8	***150.2***	0.101	0.094	***0.098***
	201	200	200.1	***0.945***	200.6	199.7	***200.1***	0.104	0.096	***0.100***
	251	250	250.3	***0.963***	250.9	249.6	***250.2***	0.107	0.101	***0.104***
(150/900)°C	301	299	299.8	***0.957***	300.6	300.1	***300.3***	0.131	0.124	***0.128***
	349	351	350.2	***0.955***	350.7	349.5	***350.1***	0.135	0.127	***0.131***
	401	400	399.8	***0.969***	400.8	399.8	***400.3***	0.146	0.14	***0.143***
	451	450	449.7	***0.972***	450.5	450.1	***450.3***	0.152	0.125	***0.139***
	502	500	500.3	***0.977***	500.6	500.2	***500.4***	0.161	0.151	***0.156***
	552	550	550.1	***0.993***	550.4	549.4	***549.9***	0.174	0.17	***0.172***

Table 3-7: Emissivity data obtained for the RM-Al sample.

Scalable temp in software	TC1 (°C)	TC2 (°C)	Avg T at coated areas (°C)	Avg ε at coated areas	T at uncoated areas (°C)			ε at uncoated areas		
					UC1	*UC2*	*Avg*	*UC1*	*UC2*	*Avg*
(-20/100)°C	50	50	50.1	***1.000***	50.3	49.4	***49.9***	0.229	0.22	***0.225***
	101	100	100.0	***0.972***	100.7	99.2	***100.0***	0.165	0.156	***0.161***
(0/250)°C	152	151	150.1	***0.954***	150.9	149.6	***150.3***	0.171	0.161	***0.166***
	201	200	200.2	***0.960***	200.7	199.4	***200.1***	0.172	0.163	***0.168***
	251	250	250.4	***0.974***	250.6	249.2	***249.9***	0.177	0.168	***0.173***
(150/900)°C	300	301	300.3	***0.969***	300.7	300.4	***300.6***	0.2	0.19	***0.195***
	349	351	350.1	***0.965***	350.5	349.2	***349.9***	0.204	0.197	***0.201***
	400	401	399.8	***0.975***	400.4	399.6	***400.0***	0.214	0.205	***0.210***
	450	452	449.7	***0.985***	450.6	450.0	***450.3***	0.219	0.213	***0.216***
	502	500	500.3	***0.998***	500.4	500.1	***500.3***	0.222	0.217	***0.220***
	551	550	550.1	***1.014***	550.1	549.0	***549.6***	0.252	0.247	***0.250***

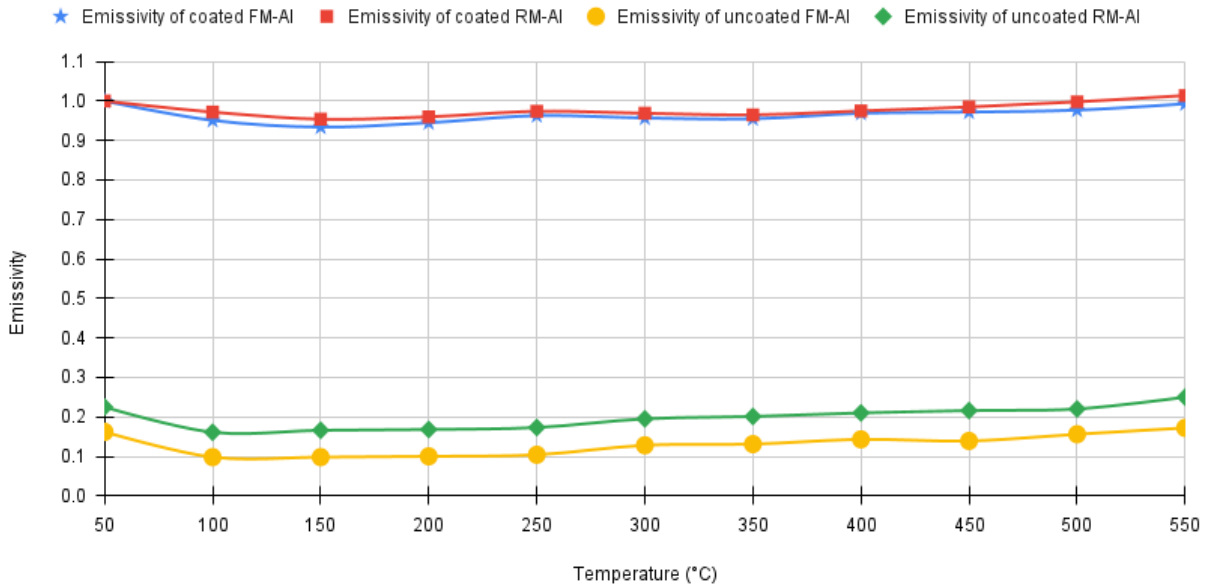

Figure 3-10: Emissivity data for the two Al samples considering coated and uncoated areas.

This graph is shown in Figure 3-10 clearly explains the emissivity of FM-Al and RM-Al samples with and without ceramic-based high emissivity paint. RM-Al sample showed higher emissivity when compared to FM-Al because FM surface exhibits higher reflectivity, and hence lower absorptivity and lower emissivity. Whereas, in case for RM surface finish, there is lower reflectivity and hence higher absorptivity and higher emissivity. Emissivity data of the uncoated Al-FM sample was correlated as function of temperature in the form of the following equation:

$$\varepsilon \approx 0.2660606 - 0.002840625\,T + 0.00015556T^2 - 3.285936e^{-8}T^3 + 2.438228e^{-11}T^4 \quad (3.1)$$

The fitting curve representing equation (3.1) is shown in Figure 3-11.

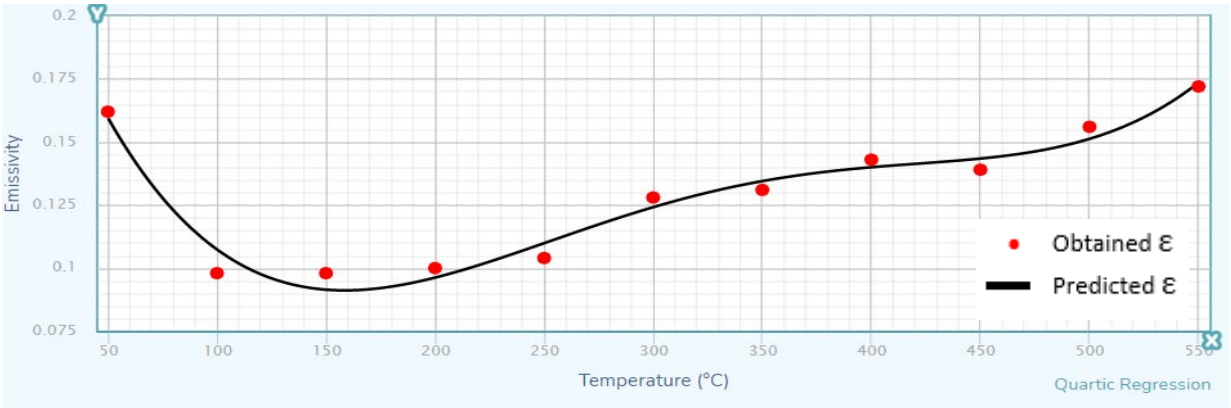

Figure 3-11: Fitting curve of Emissivity date obtained for the FM-Al sample.

Similarly the emissivity data obtained for the RM-Al sample has been fitted in equation (3.2). The fitting curve is shown in Figure 3-12.

$$\varepsilon \approx 0.3285455 - 0.002854064T + 0.0001602378T^2 - 3.453302e^{-8}T^3 + 2.61072e^{-11}T^4 \quad (3.2)$$

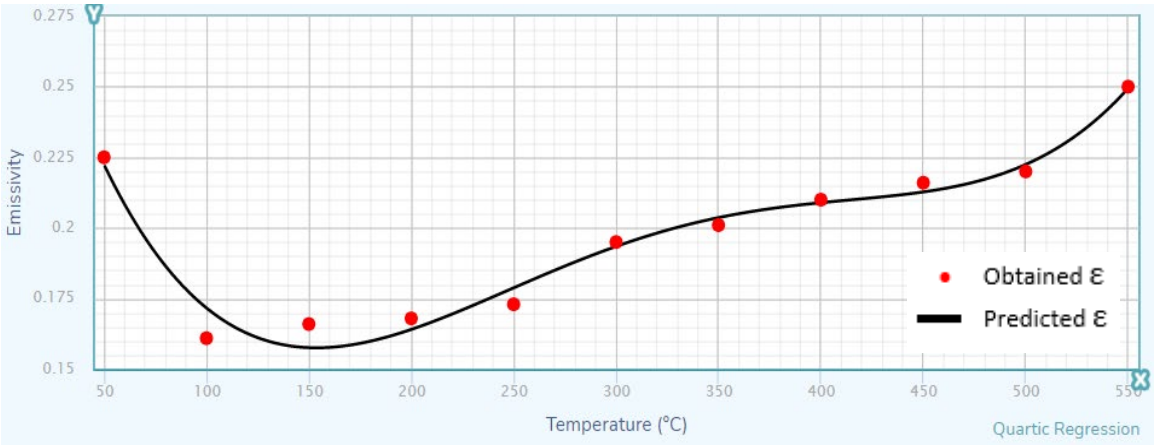

Figure 3-12: Fitting curve of Emissivity date obtained for the RM-Al sample.

3.2.3 Emissivity for Stainless Steel Sample

Similarly, tests were conducted on FM-SS and RM-SS samples from 50°C to 800°C, data being recorded for every 50°C on fixed areas as shown in Figure 3-13. It was made sure that the same heat load was applied for both samples. Table 3-8 and Table 3-9 shows the emissivity data for FM-SS and RM-SS samples.

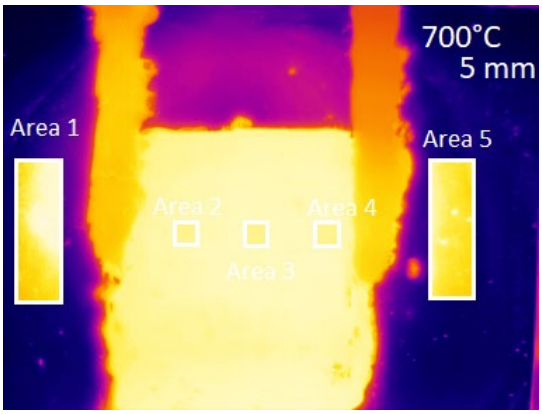

Figure 3-13: IR Image showing measure areas considered on FM-SS sample at 700 ℃.

Table 3-8: Emissivity data obtained for the FM-SS sample.

Scalable temp in software	TC1 (°C)	TC2 (°C)	Avg T at coated areas (°C)	Avg ε at coated areas	T at uncoated areas (°C)			ε at uncoated areas		
					UC1	*UC2*	*Avg*	*UC1*	*UC2*	*Avg*
(-20/100)°C	50	50	50.1	***1.000***	50.2	50.1	***50.2***	0.16	0.15	***0.155***
	99	100	100	***0.968***	100.8	100.1	***100.5***	0.174	0.167	***0.171***
(0/250)°C	150	150	150.2	***0.949***	150.1	149.8	***150.0***	0.209	0.189	***0.188***
	200	200	200.1	***0.959***	200.3	199.1	***199.7***	0.216	0.198	***0.194***
	251	250	250	***0.971***	250.5	250.2	***250.4***	0.222	0.21	***0.203***
(150/900)°C	300	302	300	***0.955***	300.9	299.7	***300.3***	0.247	0.237	***0.224***
	351	350	350	***0.961***	350.7	349.7	***350.2***	0.254	0.246	***0.232***
	402	401	400.1	***0.966***	400.3	400	***400.2***	0.262	0.256	***0.242***
	450	450	450.1	***0.976***	450.2	449.9	***450.1***	0.273	0.268	***0.248***
	501	500	500	***0.993***	500.6	500.2	***500.4***	0.286	0.283	***0.255***
	550	551	550.1	***1.004***	550.4	549.8	***550.1***	0.302	0.297	***0.266***
	602	600	600.1	***1.014***	600.7	599.5	***600.1***	0.316	0.315	***0.278***
	652	649	650.2	***1.031***	650.1	649.5	***649.8***	0.332	0.332	***0.298***
	702	701	700.1	***1.031***	700.4	699.5	***700.0***	0.329	0.319	***0.324***
	751	750	750.2	***1.030***	750.6	749.8	***750.2***	0.325	0.319	***0.322***
	802	800	800.1	***1.029***	800.2	799.4	***799.8***	0.330	0.327	***0.329***

From Table 3-8, at temperatures above 550°C, emissivity for the coated surface is greater than 1 which is realistically impossible. However, although this is counter-intuitive, it can be possible in two cases. Firstly, the pre calibration work done for the IR camera must be done using a grey body of ε<1 as a reference object. Secondly, the emissivity of a little particle, in relative disconnection from different particles, can be more than one. This is best perceived if one thinks about scattering or absorption as the correlative to emissivity. It is generally realized that finite, detached particles can frequently scatter or absorb more light than would spatially come under the entire area of interest [30]. Emissivity, generally for similar reasons,

can surpass unity under comparable conditions. Similarly, tests were conducted for RM-SS and results were plotted in Table 3-9.

Table 3-9: Emissivity data obtained for RM-SS sample.

Scalable temp in software	TC1 (°C)	TC2 (°C)	Avg T at coated areas (°C)	Avg ε at coated areas	T at uncoated areas (°C)			ε at uncoated areas		
					UC1	*UC2*	*Avg*	*UC1*	*UC2*	*Avg*
(-20/100)°C	50	50	50	***1.000***	50.2	50.1	***50.2***	0.234	0.203	***0.219***
	100	100	100.0	***0.956***	100.8	100.0	***100.4***	0.195	0.161	***0.178***
(0/250)°C	151	150	150.1	***0.945***	150.6	149.4	***150.0***	0.204	0.171	***0.199***
	201	200	200.0	***0.952***	200.4	199.8	***200.1***	0.209	0.178	***0.207***
	252	250	250.4	***0.964***	250.6	250.7	***250.7***	0.218	0.187	***0.216***
(150/900)°C	301	300	300.1	***0.954***	300.5	299.3	***299.9***	0.241	0.207	***0.242***
	352	350	349.8	***0.964***	350.2	349.4	***349.8***	0.25	0.213	***0.25***
	402	400	400.4	***0.968***	400.8	400.4	***400.6***	0.259	0.225	***0.259***
	452	450	449.9	***0.972***	450.6	449.9	***450.3***	0.265	0.231	***0.271***
	502	500	500	***0.980***	500.7	500.0	***500.4***	0.273	0.237	***0.285***
	552	550	550.1	***0.986***	550.4	549..9	***550.2***	0.282	0.249	***0.3***
	602	600	600.1	***0.999***	600.2	599.1	***599.7***	0.295	0.26	***0.316***
	653	649	650	***1.021***	650.6	649.7	***650.2***	0.317	0.279	***0.331***
	703	699	700.1	***1.038***	700.9	699.4	***700.2***	0.344	0.303	***0.324***
	754	749	750.3	***1.058***	750.4	749.3	***749.9***	0.367	0.320	***0.344***
	801	800	800.1	***1.058***	800.6	799.2	***799.9***	0.389	0.349	***0.369***

Figure 3-14 shows the IR and actual image captured by the XI-400 camera for FM-SS sample at a temperature of 700°C after calibration. This graph is shown in Figure 3-15 clearly explains the emissivity of FM-SS and RM-SS samples with and without high emissivity paint.

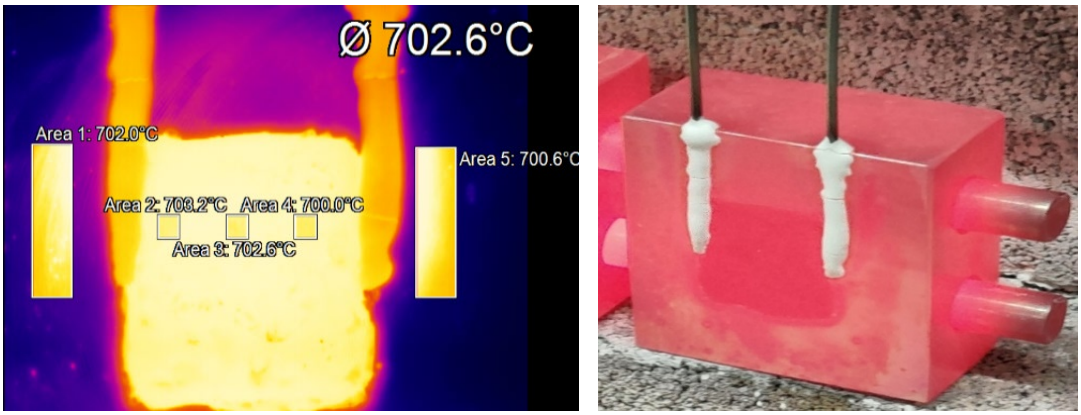

Figure 3-14: The IR image (left) and the actual image (right) of the FM-SS sample at 700°C.

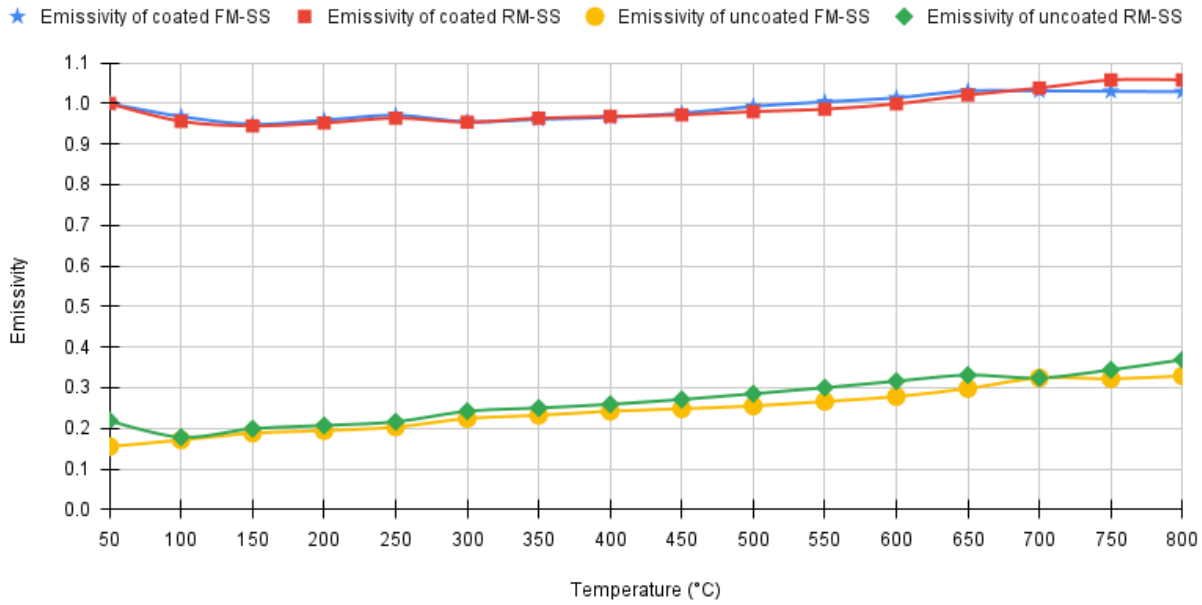

Figure 3-15: Emissivity data for the two SS samples considering coated and uncoated areas.

Emissivity data of the uncoated Al-FM sample was correlated as function of temperature in the form of the following equation:

$$\varepsilon = 0.1286298 + 0.005614459T - 0.0000014926T^2 + 2.44293e^{-9}T^3 - 1.320354e^{-12}T^4 \qquad (3.3)$$

The fitting curve representing equation ((3.3) is shown in Figure 3-16.

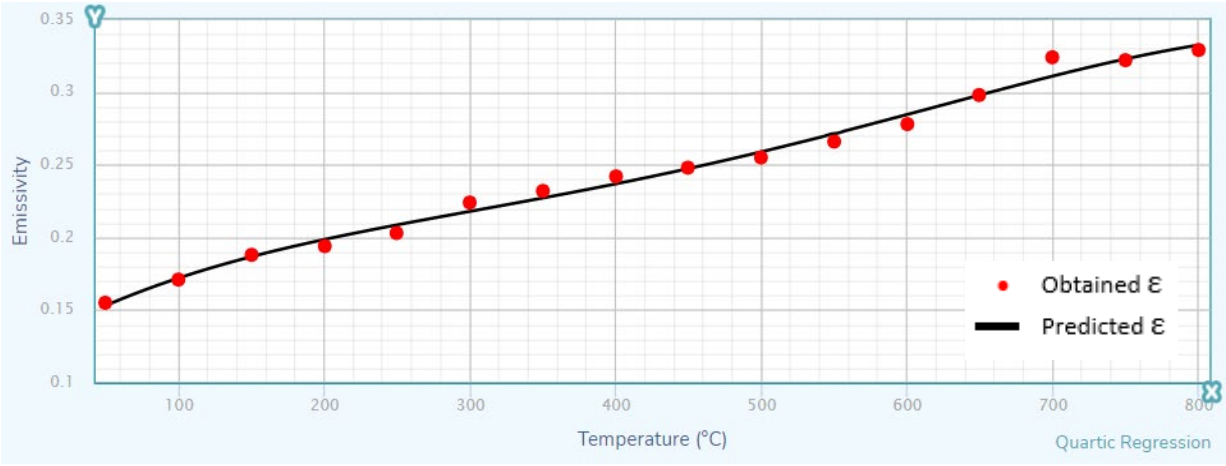

Figure 3-16: Fitting curve of Emissivity date obtained for the FM-SS sample.

Similarly the emissivity data obtained for the RM-SS sample has been fitted in equation (3.4). The fitting curve obtained was shown in Figure 3-17.

$$\varepsilon = 0.2375 - 0.0007492659T + 0.000004026592T^2 - 6.342066e^{-9}T^3 + 3.41748e^{-12}T^4 \qquad (3.4)$$

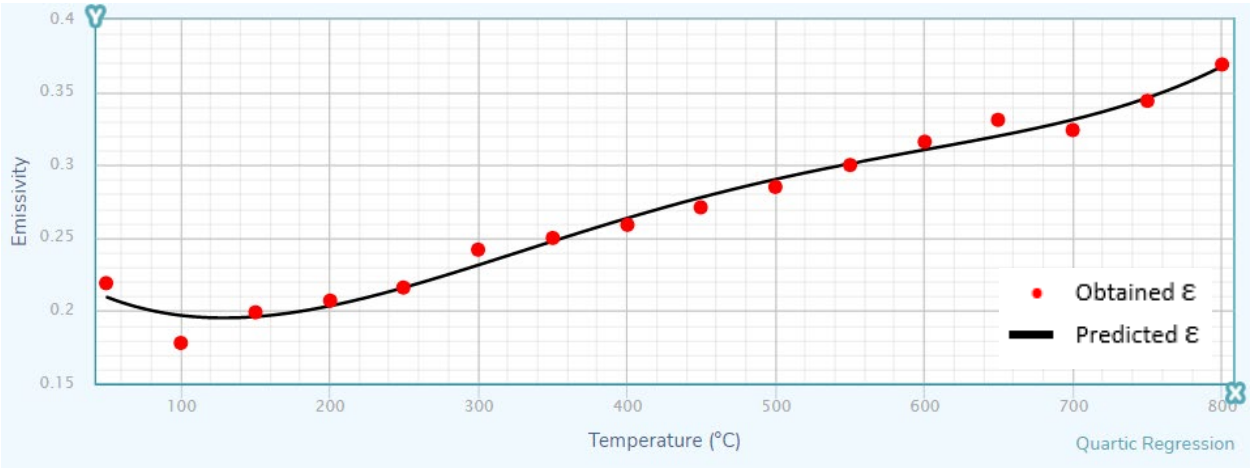

Figure 3-17: Fitting curve of Emissivity date obtained for the RM-SS sample.

3.2.4 Emissivity for Low Carbon Steel Sample

The emissivity behavior of LCS is unique when compared to the other two metals that were discussed earlier in this work. This is because of the presence of Iron (Fe) content of more than 99% due to which oxidation of ferrous particles occurs rapidly on the surface. Figure 3-18 shows the oxidation level of LCS

at a temperature of 600°C. Table 3-10 and Table 3-11 shows emissivity data for both FM-LCS and RM-LCS samples.

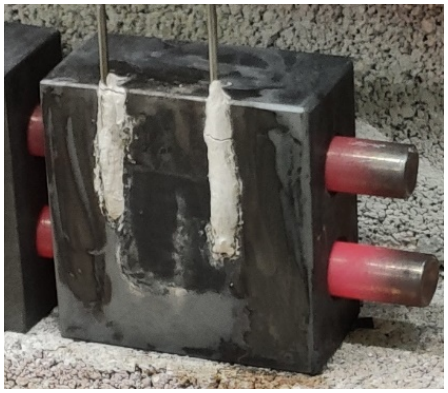

Figure 3-18: Oxidation of FM-LCS sample at 600°C.

Table 3-10: Emissivity data obtained for FM-LCS sample.

Scalable temp in software	TC1 (°C)	TC2 (°C)	Avg T at coated areas (°C)	Avg ε at coated areas	T at uncoated areas (°C)			ε at uncoated areas		
					UC1	*UC2*	*Avg*	*UC1*	*UC2*	*Avg*
(-20/100)°C	50	50	50	***0.980***	50	50.1	***50.1***	0.261	0.252	***0.257***
	101	99	100	***0.957***	100	100	***100.0***	0.195	0.189	***0.192***
(0/250)°C	152	150	150	***0.957***	150.1	150	***150.1***	0.215	0.207	***0.211***
	202	201	200.4	***0.955***	200.9	200.1	***200.5***	0.242	0.221	***0.232***
	253	251	249.8	***0.978***	251.7	250.1	***250.9***	0.251	0.237	***0.244***
(150/900)°C	303	299	300.2	***0.963***	300.7	300.0	***300.4***	0.278	0.265	***0.272***
	353	349	350.1	***0.979***	350.6	350.3	***350.5***	0.308	0.286	***0.297***
	403	400	400.3	***0.993***	400.9	400.3	***400.6***	0.425	0.371	***0.398***
	455	448	450.6	***1.008***	451.1	450.3	***450.7***	0.514	0.511	***0.513***
	506	499	500.2	***1.036***	501.2	500.2	***500.7***	0.812	0.795	***0.800***
	554	551	550.8	***1.049***	551.8	550.6	***551.2***	0.887	0.878	***0.883***
	605	600	601.3	***1.062***	601.1	600.5	***600.8***	0.907	0.907	***0.907***
	654	649	650.4	***1.069***	650.7	649.5	***650.1***	0.922	0.900	***0.911***
	703	699	700.5	***1.072***	700.8	699.9	***700.4***	0.936	0.912	***0.924***
	754	749	750.1	***1.075***	750.7	749.4	***750.1***	0.941	0.929	***0.935***
	801	800	800.2	***1.069***	800.8	799.5	***800.2***	0.923	0.913	***0.918***

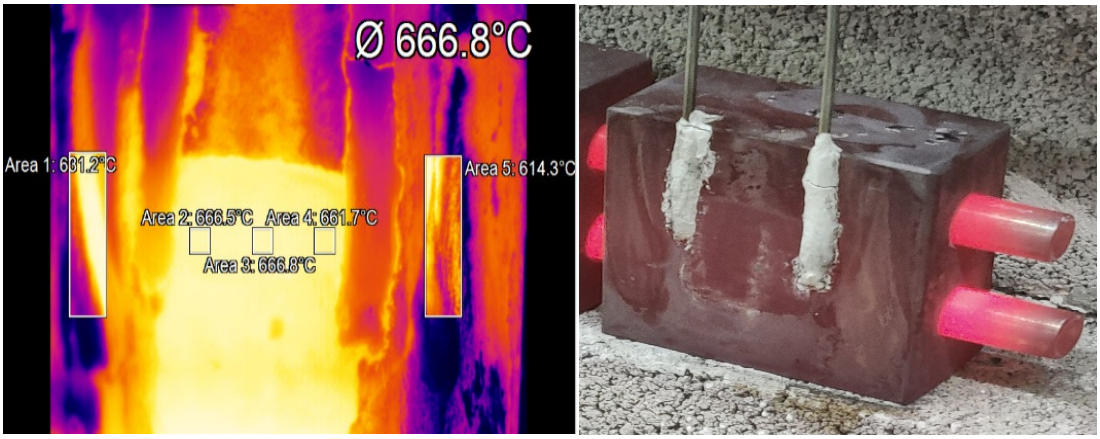

Figure 3-19: IR image (left) and actual image (right) of RM-LCS sample at 650°C.

From Figure 3-19 can be clearly seen from the IR image that oxidation occurs differently in both the uncoated areas (UC1 and UC2) due to which there is a slight variation in emissivity values.

Table 3-11: Emissivity data obtained for RM-LCS sample.

Scalable temp in software	TC1 (°C)	TC2 (°C)	Avg T at coated areas (°C)	Avg ε at coated areas	T at uncoated areas (°C)			ε at uncoated areas		
					UC1	*UC2*	*Avg*	*UC1*	*UC2*	*Avg*
(-20/100)°C	50	50	50.0	***1.000***	50.1	50.1	***50.1***	0.294	0.290	***0.292***
	101	99	100.0	***0.992***	100	100	***100.0***	0.204	0.199	***0.201***
(0/250)°C	151	150	150.0	***0.964***	150.1	150.1	***150.1***	0.305	0.301	***0.303***
	201	202	200.2	***0.977***	200.9	200.4	***200.6***	0.312	0.294	***0.305***
	252	250	249.9	***0.989***	251.7	250.0	***250.8***	0.318	0.307	***0.311***
(150/900)°C	301	299	300.1	***0.979***	300.7	300.1	***300.5***	0.278	0.265	***0.338***
	352	349	350.4	***0.985***	350.6	349.9	***350.3***	0.378	0.356	***0.362***
	401	400	400.1	***1.002***	400.7	400.1	***400.3***	0.432	0.411	***0.422***
	450	449	450.2	***1.032***	451.1	450.4	***450.7***	0.554	0.534	***0.544***
	502	500	500.0	***1.064***	501.2	500.1	***500.6***	0.852	0.832	***0.843***
	553	551	550.6	***1.075***	551.8	550.4	***551.1***	0.906	0.894	***0.900***
	604	600	600.8	***1.090***	601.1	600.3	***600.7***	0.927	0.927	***0.927***
	652	649	650.1	***1.090***	650.7	649.7	***650.2***	0.978	0.928	***0.946***

	702	699	700.2	***1.093***	700.8	699.8	***700.4***	0.946	0.912	***0.935***
	751	749	750.4	***1.092***	750.7	749.3	***750.2***	0.961	0.929	***0.948***
	799	800	800.1	***1.095***	800.8	799.3	***800.1***	0.963	0.913	***0.948***

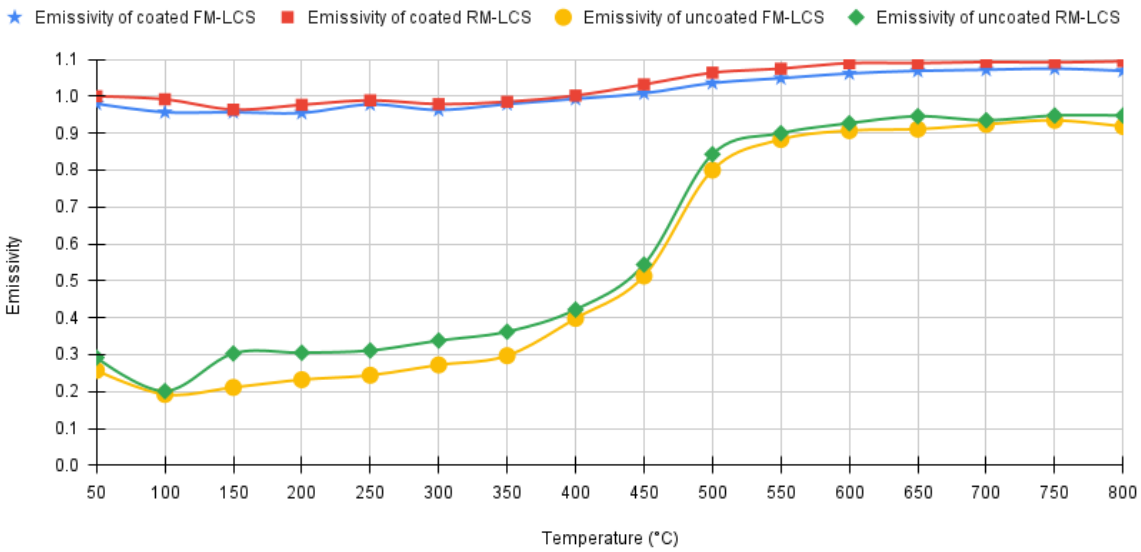

Figure 3-20: Emissivity data for the two LCS samples considering coated and uncoated areas.

The emissivity curve is plotted for FM-LCS and RM-LCS on coated and uncoated areas is shown in Figure 3-20. Emissivity data for the uncoated FM-LCS sample is fitted into the equation (3.5). Figure 3-21 shows the emissivity fitting curve for FM-LCS sample.

$$\varepsilon \approx 0.9322111 + \frac{(0.2385478 - 0.9322111)}{(1 + (T/453.7761)^{11.69771})} \qquad (3.5)$$

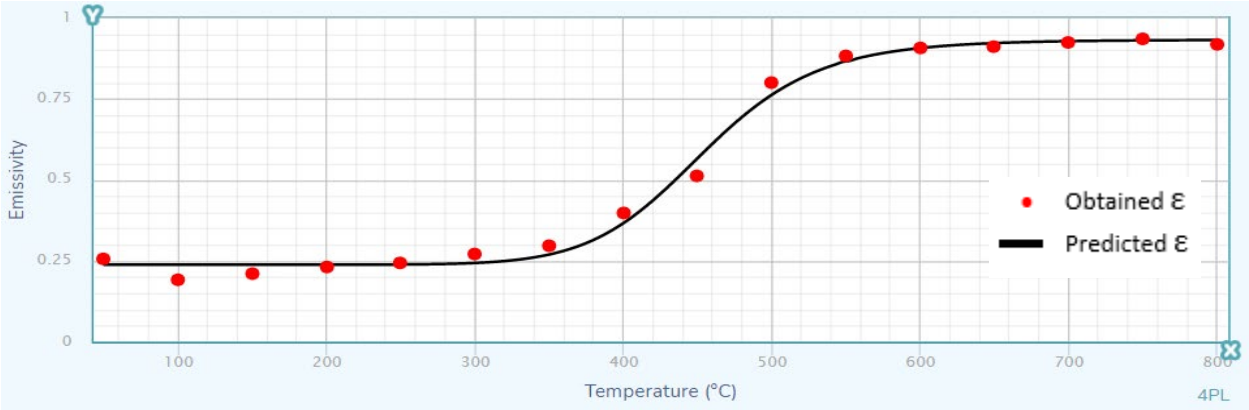

Figure 3-21: Fitting curve of Emissivity date obtained for the FM-LCS sample.

Equation ((3.6)) represents the emissivity of RM-LCS sample and fitted into a curve as shown in Fig. 3-22.

$$\varepsilon \approx 0.9492394 + \frac{(0.2989873 - 0.9492394)}{(1 + (T/456.5037)^{13.30414})} \quad (3.6)$$

Figure 3-22: Fitting curve of Emissivity date obtained for the RM-LCS sample.

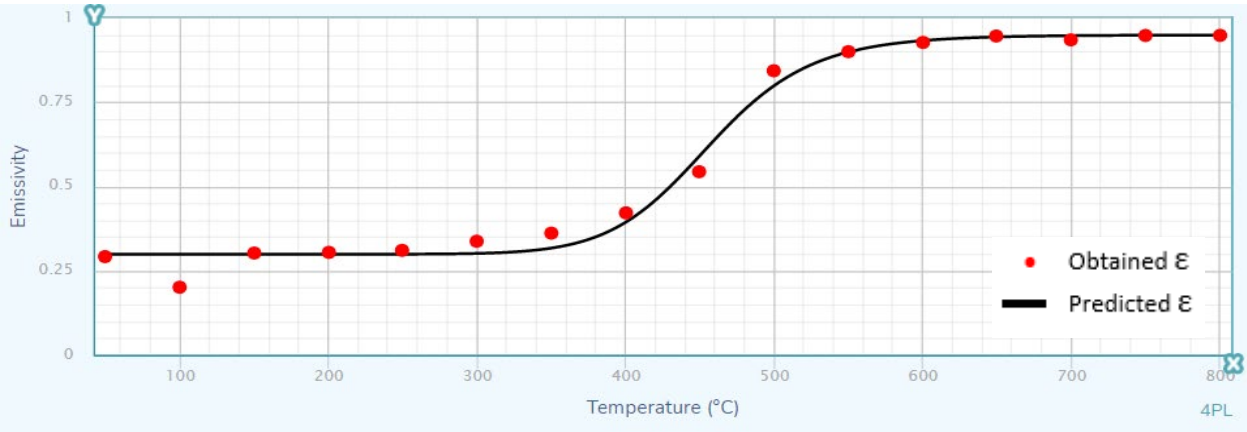

3.2.5 Effect of Base Material on Emissivity of the coated surfaces

Emissivity of coated samples surfaces made from different materials has been measured. Results have been analyzed to determine the effect of base material on the emissivity of the coated surface. Results shown in Fig. 3.23 indicate that both base material and surface finish have an effect on the emissivity of the coated surfaces. In terms of the effect of the base material at 500°C, coated FM-LCS sample showed the highest emissivity of 1.036, while coated FM-Al sample showed the lowest of 0.977, while coated FM-SS sample showed an intermittent value of 0.993. May be this is attributed to the lower emissivity of aluminum when compared to stainless steel and low carbon steel. In terms of the effect of surface finish, the rough samples showed higher emissivity than the fine samples. For example at 500°C, coated FM-Al has an emissivity of 0.977, whereas coated RM-Al showed an emissivity of 0.998. Similar results were observed in case of stainless steel and low carbon steel as shown in Fig 3-23.

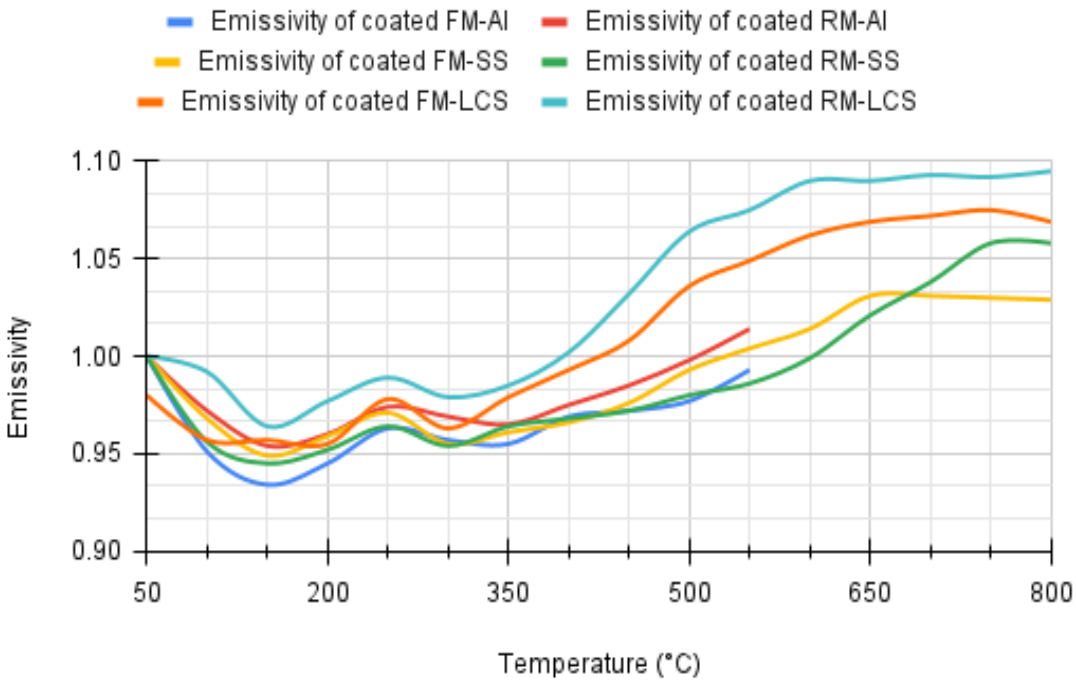

Figure 3-23: Emissivity of coated materials.

Chapter 4. Defects Detection using the IR Camera

Active Thermography is the most practiced contact-free Non Destructive technique (NDT) used for quality control in manufacturing industries. It can be classified into – Lock-In Thermography and Pulse Phase Thermography [4]. Pulse Phase thermography refers to applying continuous heat (constant energy pulse) to a test sample to achieve a desired temperature and cut off the heat supply to study the temperature decay curve to assess defects, whereas Lock-In thermography refers to the supply of periodic energy waves (e.g., microwave, thermal flash lamps etc.) onto the surface of the sample and study how the waves are phase-shifted and partially reflected (due to inhomogeneity) and obtained on the other end of sample for defect detection analysis. In this work, defect detection experiments are conducted based on the Pulse Phase technique using electric heaters. The distribution of heat and hence the resulted thermal field is affected/controlled by material inhomogeneity and defects, hence it can be identified by using an IR camera, as shown in Fig. 4-1.

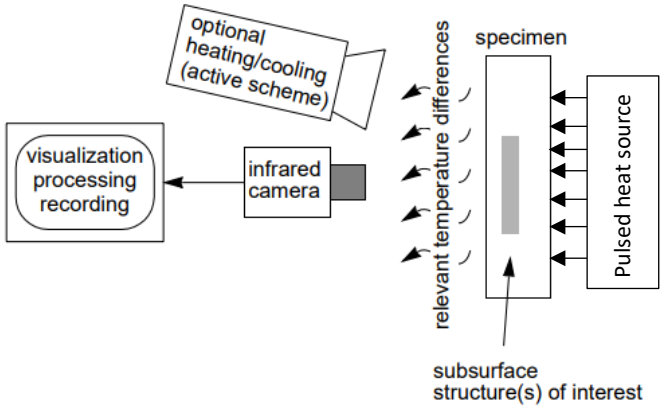

Figure 4-1: Working principal of using IRT for non-destructive defects detection [4].

Detecting weld defects during an actual laser welding operation was not possible in the laboratory. Alternatively, following the working principle depicted in Fig. 4-1, experiments have been carried out to assess the ability of the IR camera to detect a selected set of geometry-based defects impeded in a Stainless Steel test sample.

4.1 Test Sample Preparation

Since Stainless Steel is the most commonly used material in pipeline manufacturing, all defect detectability tests have been conducted on the FM-SS sample (see Table 3-1). Defects in the form of holes drilled through the test sample have been used to mimic material voids inside the welded material. Therefore, defect detectability considered in this study depends on the hole diameter, D_h, and on the distance between the defect (the hole end) and the test sample surface, δ. In order to investigate the effect of these two variables on defect detectability considered here, two sets of defects have been considered and tested. The first set is considered to investigate the effect of δ, while the second set is used to investigate the effect of D_h. Table 4-1 and Fig. 4-2 and Fig. 4-3 provide details of these sets. Values of δ and D_h have been chosen in consultation with the industrial partner.

Table 4-1: Details of tested defects.

Set	Defect name	D_h (mm)	δ (mm)
1	D11	5	3.0
1	D12	5	4.0
1	D13	5	2.0
2	D21	1.0	1.25
2	D22	1.5	1.25
2	D23	1.25	1.25

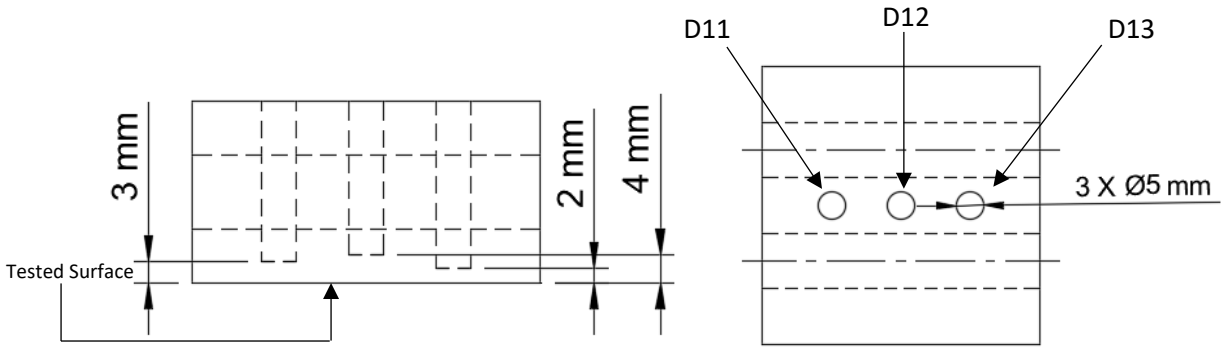

Figure 4-2: Top view (left) and rear view (right) of Set – 1 defects considered to investigate the effect of δ.

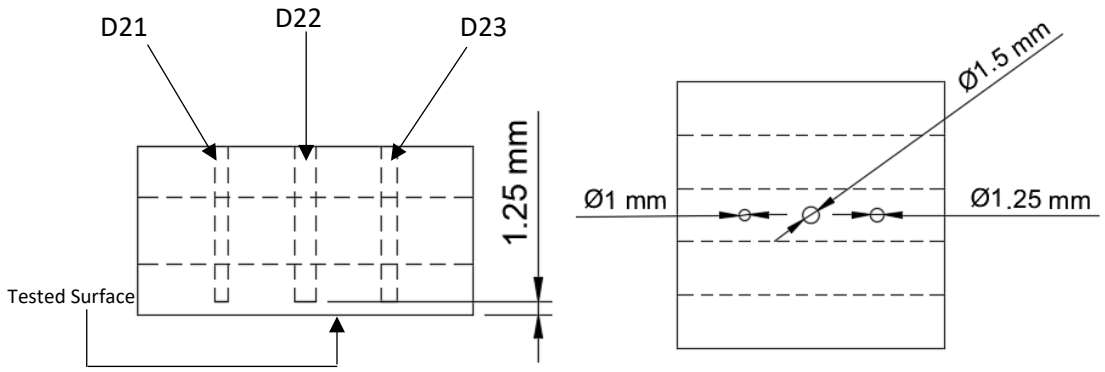

Figure 4-3: Top view (left) and rear view (right) of Set – 2 defects considered to investigate the effect of D_h.

4.2 Experimental Investigation of Defect Detectability

The same experimental setup discussed in Chapter 3 that was used to measure emissivity has been used to conduct the defects detectability experiments. The emissivity data obtained for the FM-SS sample was used as an input to the software of the IR Camera. Experiments were conducted for the two defect sets discussed above. It is worth noting here, that the defect detectability is required within the heat-affect weld zone during the cooling down period that follows the welding operation. Therefore, all detectability tests have been carried out at the maximum temperature of 800 °C that was considered in the emissivity measurement tests discussed in Chapter 3. Proper care was taken to ensure that samples were heated at the same rate from ambient to 800 °C similar to the emissivity measurement tests. Once test sample reached steady-state at the required temperature, the power was automatically turned off by the temperature controller. The heating time was about 1000 sec for the sample to achieve a uniform temperature of 800°C. Defect detection was investigated from the thermal images collected during the cooling down period.

4.3 Results and Discussion

Pix Connect software used along with the IR camera measures temperature on the sample surface at 160*120 pixels. It compares the surface temperature on defect areas with the surface temperature of

area surrounding the defects. Provided the experimental surface temperature drop (ΔT_{exp}) obtained from the difference between the two temperature values, the image processing capability of the software will recognize the defects. Based on the IR camera specifications listed in Table 3.3, the minimum temperature difference the IR camera can detect is about 2% of the recorded maximum temperature. So for e.g. at 800 °C, the minimum temperature difference (ΔT_{min}) that the IR camera can detect is equal to 16 °C. Therefore, any defect that causes a $\Delta T_{exp} > \Delta T_{min}$ (based on the recorded maximum temperature that the camera can recognize) during that time is considered detectable. The value of the detectability threshold has been adjusted based on the maximum sample surface temperature.

4.3.1 Results of the First Set of Defects – Effect of δ

The first type of defects was introduced by drilling holes inside the test sample, which is not necessarily the case that one would experience with a plate having an internal material void. The existence of the hole will affect the rate of heat transfer by convection and radiation. Hence, it is expected to affect the resulting temperature difference on the sample surface, which could affect the defect detectability. In an attempt to remedy this issue, two sets of experiments were carried out. One set of experiments were carried out while the holes were filled in with glass wool insulating material.

4.3.1.1 Set One Experiments - without Glass Wool (GW)

The test sample without GW was heated to about 800° C for about 1000 sec. The power supply was cut off and the sample surface temperature distribution was observed during the cooling down period. It is worth noting here that no defects were detected during the heating period. This is because the thermal diffusivity of stainless steel is lower than that of air, and hence the temperature difference observed on the surface during the heating phase is minimal. However, the defects started to appear during the cooling phase as there the heat transfer by convection from the solid surface to ambient air is higher than heat lost through the air cavity within each defect. The D11 and D13 defects were detected after 7 seconds in the cooling period causing a surface temperature drop (ΔT_{exp}) of 34 °C and 42 °C. However, for

D12 defect, the ΔT_{exp} observed was about 11°C, which was less than ΔT_{min} (~15.4 °C for 768 °C). Hence, D12 was not detected by IR camera. Fig. 4-4 shows the captured IR image 7 sec in the cooling period. Table 4-2 shows the temperature data observed near the defect regions.

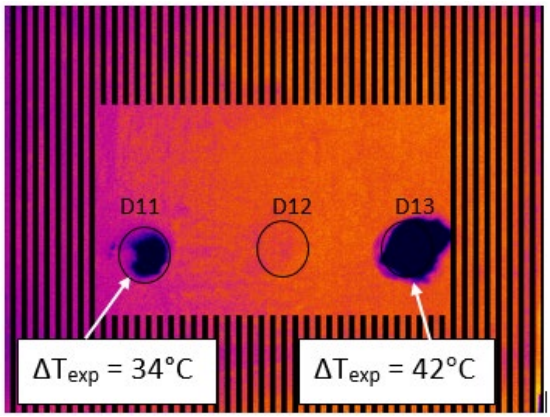

Figure 4-4: An IR image obtained during the test conducted on the Set – 1 defects without GW.

Table 4-2: Temperature data obtained 7 seconds in the cooling period for Set – 1 defects without GW.

Defects	Average Temperature on surface above the defect (°C)	Average Temperature on surface surrounding the defect(°C)	ΔT_{exp} (°C)	Detectability
WGW-D11	731	765	34	Yes
WGW-D12	757	768	11	No
WGW-D13	724	766	42	Yes

4.3.1.2 Set One Experiments - with Glass Wool (GW)

Tests were conducted by placing glass wool into the holes leaving a gap about 5 mm, as shown in Fig. 4-5.

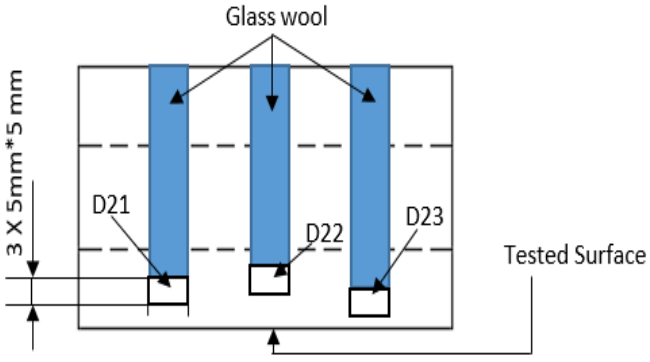

Figure 4-5: Sectional view of sample with Set – 1 defects with GW.

Results of this test were somewhat similar to the without GW test results. Only defects D11 and D13 were detectable. However, after about 12 seconds in the cooling period. The extra 5 seconds observed in the sample with GW test is believed to be due to the higher heat loss from the holes occurred during the without GW test. The corresponding ΔT_{exp}, observed on the surface was 26 °C and 34 °C, respectively. However, no trace of the D12 was observed test because it resulted in a small ΔT_{exp} of 6 °C, which is significantly lower than the ΔT_{min} (~15. 5 °C at 775 °C) that the IR camera can detect. Table 4-3 shows the temperature data obtained neat the defect regions for first set of defects with GW at 1012 sec.

Table 4-3: Temperature data obtained 12 seconds in the cooling period for Set – 1 defects with GW.

Defects	Average Temperature on surface above the defect (°C)	Average Temperature on surface surrounding the defect(°C)	ΔT_{exp} (°C)	Detectability
GW-D11	753	779	26	Yes
GW-D12	781	775	6	No
GW-D13	742	776	34	Yes

4.3.1.3 Summary of Effect of δ on Set – 1 Defects detectability

From the results, it was clear that there is an effect of both δ and glass wool, on detectability of Set -1 defects. Considering the effect of δ without GW, the defects WGW-D11 and WGW-D13, located at 2 mm and 3 mm from the surface, were detected by the IR camera with a ΔT_{exp} of 34 °C (as $\Delta T_{min} \approx 15.3$ °C for 765 °C) and 42 °C (as $\Delta T_{min} \approx 15.3$ °C for 766 °C) respectively. No trace of WGW-D12, located at 4 mm from the surface, as ΔT_{exp} recorded was only 11°C, which is less than ΔT_{min} (~15.4 °C for 768°C). Similarly with GW, the effect of δ, resulted in finding defects GW-D11 and GW-D13 because $\Delta T_{exp} > \Delta T_{min}$ at both the defects. No trace of GW-D12, as ΔT_{exp} observed is only 6 °C, which is less than ΔT_{min} (~15. 5 °C at 775 °C). From the tests, it can be concluded that the δ based defects located at 2 mm and 3 mm were identified, but no trace of defects at 4 mm, because homogeneity in 4mm thickness of stainless steel making it harder for $\Delta T_{exp} > \Delta T_{min}$. Also, defects with GW showed less ΔT_{exp} than the defects without glass wool.

4.3.2 Results of the Second Set of Defects – Effect of D_h

Tests were conducted on samples with the second set of defects to study the effect of varying hole diameter, D_h on defect detectability. Tests were conducted on samples with and without glass wool.

4.3.2.1 Set Two Experiments - without Glass Wool (GW)

Samples were heated for about 1000 sec to 800°C then left to cool down to room temperature. Similar to the results of the first set, no defects of the second set were observed during the heating period. Temperature data from the thermocouples was recorded and thermal images was captured by the IR camera during the cooling down period. After about 9 sec in the cooling period, defects D22 and D23 were detected with ΔT_{exp} of 31 °C and 17 °C, respectively. The corresponding detectability limits are 15.7 °C (at 785 °C) and 15.4 °C (at 773 °C). The ΔT_{exp} caused by defect D21 was about 3 °C. These results indicate that defect D21 was clearly undetectable, defect D22 was clearly detectable, while defect D23 was somewhat border line, yet detected. Fig. 4-6 shows the IR image obtained during the without GW test after 9 sec in the cooling down period. Temperature data obtained during the without GW test is shown in Table 4-4.

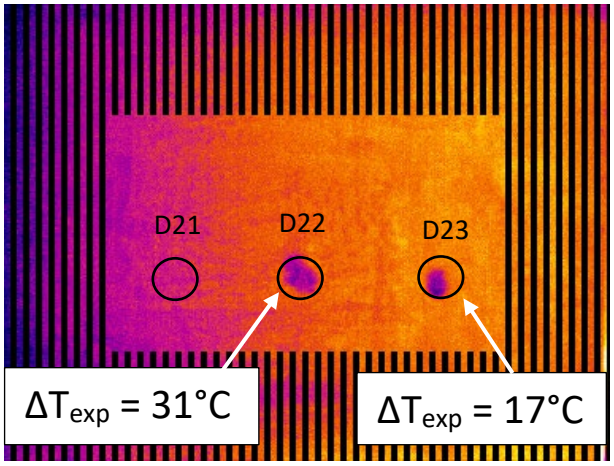

Figure 4-6: An IR image obtained during the test conducted on the Set – 2 defects without GW

Table 4-4: Temperature data obtained 9 seconds in the cooling period for Set – 2 defects without GW.

Defects	Average Temperature on surface above the defect (°C)	Average Temperature on surface surrounding the defect(°C)	ΔT_{exp} (°C)	Detectability
WGW-D21	755	758	3	No

WGW-D22	754	785	31	Yes
WGW-D23	756	773	17	Yes

4.3.2.2 Set Two Experiments - with Glass Wool (GW)

Glass Wool was inserted into the sample of the second set of defects leaving a gap of 1.5 mm for air to accumulate to the sample surface as shown in Fig. 4-7.

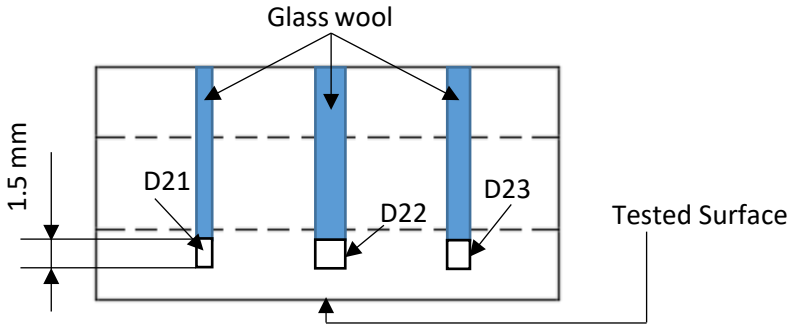

Figure 4-7: Sectional view of sample with Set – 2 defects with Glass Wool.

Tests have been conducted and temperature data was recorded. No defects were observed during the heating period. Only defect D22 was detected after 14 seconds in the cooling down period resulting in a ΔT_{exp} of about 26 °C. Defects D21 and D23 resulted in ΔT_{exp} of about 4 °C, and ΔT_{min} required to be detectable are 15° (at 754 °C) and 14.9 (at 748 °C) which rendered both defects undetectable. Fig. 4-8 shows the IR image captured after 14 sec in the cooling period. Temperature data obtained during the test with glass wool for the second set of defects is provided in Table 4-5.

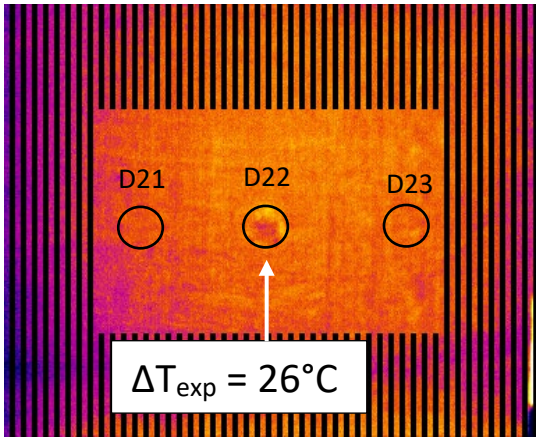

Figure 4-8: IR image obtained during the GW test of Set – 2 defects with Glass Wool.

Table 4-5: Temperature data obtained 14 second in the cooling down period of Set – 2 defects with Glass Wool.

Defects	Temperature on defect region (°C)	Temperature on defect surrounding (°C)	ΔT_{exp} (°C)	Detectability
GW-D21	749	754	4	No
GW-D22	730	756	26	Yes
GW-D23	744	748	4	No

4.3.2.3 Summary on Effect of D_h on Set – 2 Defects detectability

The results on samples with varying hole diameter D_h on Set - 2 defects clearly indicated that as D_h increases, the more chances for the defect to be detectable. For the sample without GW, the defect WGW-D22, of D_h = 1.5 mm, was found detectable as ΔT_{exp} (31 °C)> ΔT_{min} (15.7 °C). Defect WGW-D23, of D_h = 1.25 mm, showed a ΔT_{exp} of 17 °C which was very close to ΔT_{min} (15.4 °C), however recognized by the IR camera software. No trace of WGW-D21, with D_h = 1 mm, as $\Delta T_{exp} < \Delta T_{min}$. For the sample with GW, only defect GW-D22 was detected by the IR camera as ΔT_{exp} (26 °C) > ΔT_{min} (15.1 °C). Defects GW-D21 and GW-D23 were not detected as $\Delta T_{exp} < \Delta T_{min}$.

Chapter 5. Defect Detection during Actual Welding Operations

Detecting weld defects during actual welding operations was not possible in the laboratory. Alternatively, studying the detectability of weld defects during actual welding processes using numerical modelling is possible provided that numerical results are validated using accurate experimental data. Therefore, a numerical model has been developed using the commercial computational package ANSYS-Mechanical. Numerical simulations of the conditions considered in the experimental tests conducted on the two sets of defects imparted in the stainless steel sample have been carried out. Numerical results have been validated using experimental data discussed in chapter 3. The validated numerical model has been modified and used to investigate weld defect detectability during an actual laser welding process. Details and results of this numerical study are presented below.

5.1 Numerical Model

5.1.1 Geometry and Material Properties

The transient thermal module of in ANSYS was used to study defect identification in test samples. A 3D CAD model of the required sample geometrical specifications was created using SOLIDWORKS. The STEP files were then imported in ANSYS. The temperature-dependent Stainless Steel 304L properties that have been experimentally determined by Kim [31] were used in the numerical model.

5.1.2 Boundary Conditions

Temperature-dependent heat transfer coefficients along all exposed surfaces were considered and taken from the ANSYS library. Temperature-dependent emissivity data of the Stainless Steel FM sample obtained from our emissivity measurement tests was introduced in ANSYS.

5.1.3 Mesh Optimization

Transient simulations are usually computationally expensive. Several ways exist to reduce the computational time. Time step and mesh size play an important role in optimizing the computational time. In this study, adaptive meshing was employed to obtain finer elements for accurate temperature results near the areas of interest (defect regions) and relatively larger element used elsewhere. Mesh size of $5x10^{-4}$ m was chosen near the defect region, front face and heating area to ensure proper co-relation with experimental work. Mesh size of $1x10^{-3}$ m was chosen for the overall sample. CFX was used for mesh physics preference with smooth transition. Total elements of 88,740 were created with 213,841 nodes. Time steps of 1 sec and 0.2 sec were taken during and heating and cooling phases.

5.1.4 Validation of the Numerical Results

Set of numerical simulations of the same conditions considered in the experiments discussed in chapter 3 has been carried out. Temperature of a point on the surface, point "P" shown in Fig. 5-1, was monitored during the heating and cooling down period. Numerical and experimental temperature-time data is compared in Fig.5-2. These results show a reasonable agreement.

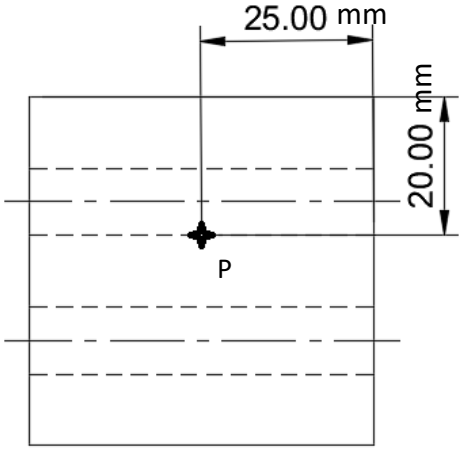

Figure 5-1: Position of temperature measurement probe at "P" on the sample surface.

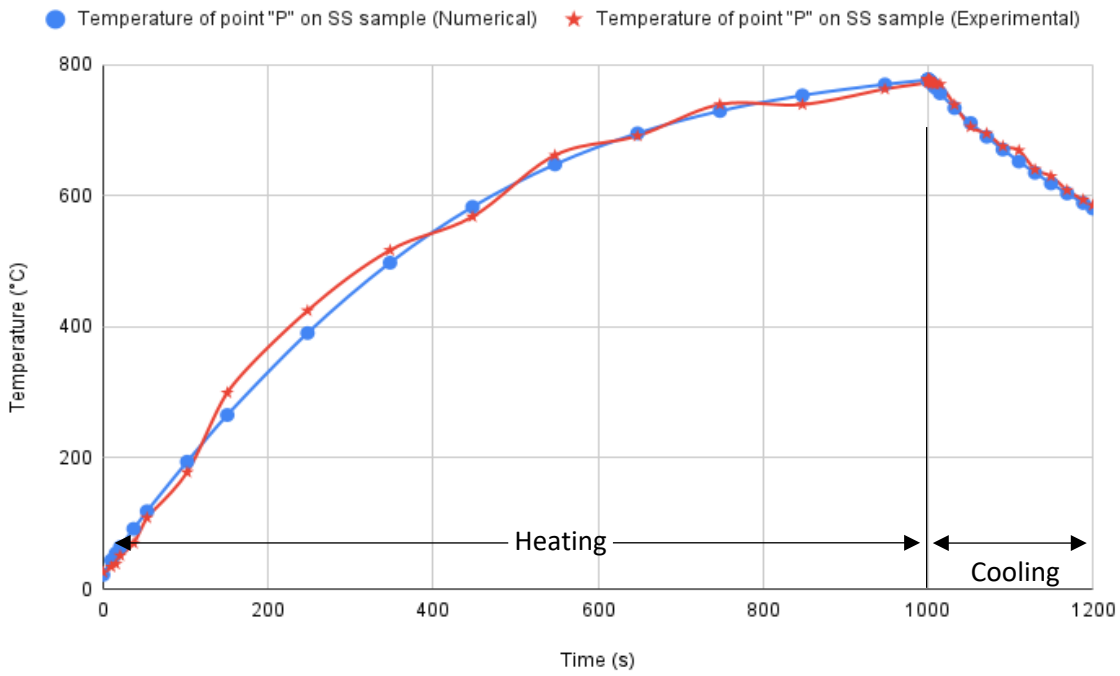

Figure 5-2: Comparison of temperature-time curves at point "P" obtained experimentally and numerically.

5.1.5 Results and Discussion

Temperature profiles were captured from the numerical simulations at the same time steps where the defects were observed during the experiments.

5.1.5.1 Results of the First Set of Defects – Effect of δ based.

5.1.5.1.1 Set One Simulations – without Glass Wool (GW)

Simulations were performed on stainless steel samples with Set – 1 defects as per hole specifications given in Fig. 4-2. The analysis was done for 1000 sec of heating period and another 200 seconds of cooling down period like in experiments. Data path of 10 mm each was plotted on the sample surface over the position of defects to record the temperature difference (ΔT_{num}) obtained on the defect surface when compared with the surface surrounding the defects. It was worth noting here that no defects were detected during heating period like in experiments. The D11 and D13 defects after 7 seconds in the cooling period caused a surface temperature drop (ΔT_{num}) of 31.2 °C and 32.4 °C. Based on the corresponding detectability limit (~15.2 °C at 764 °C and 15.3 at 767 °C) that the IR camera can detect, the obtained numerical values on

sample surface shows that these defects are detectable. Defect D21 showed ΔT_{num} = 9 °C which is less than ΔT_{min} (15.3 °C) making it impossible to be detected. Fig. 5-3 shows the simulation image captured on the sample surface after 7 seconds during the cool-down period.

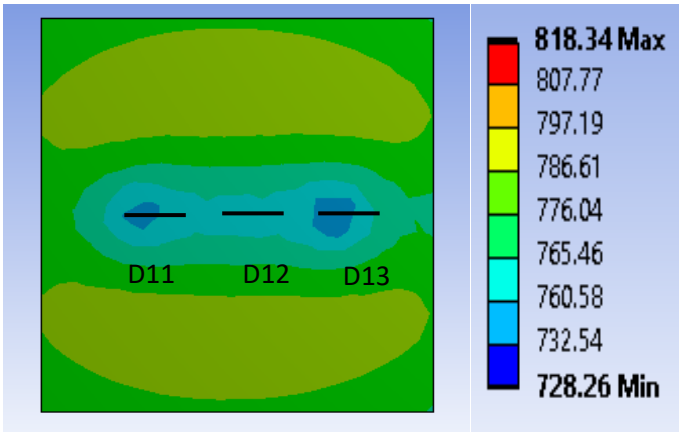

Figure 5-3: Thermal Simulation image obtained during the test conducted on Set – 1 defects without GW after 7 seconds of cooling period.

Fig. 5-4 shows the comparison of numerical and experimental temperature data obtained after 7 seconds during the cooling period on defect locations. The maximum deviation of numerical values with experimental data on defect locations – (ΔT_{en}) is only 5 °C which is a result of temperature sensitivity error, or emissivity correlation error caused by the IR camera from experiments.

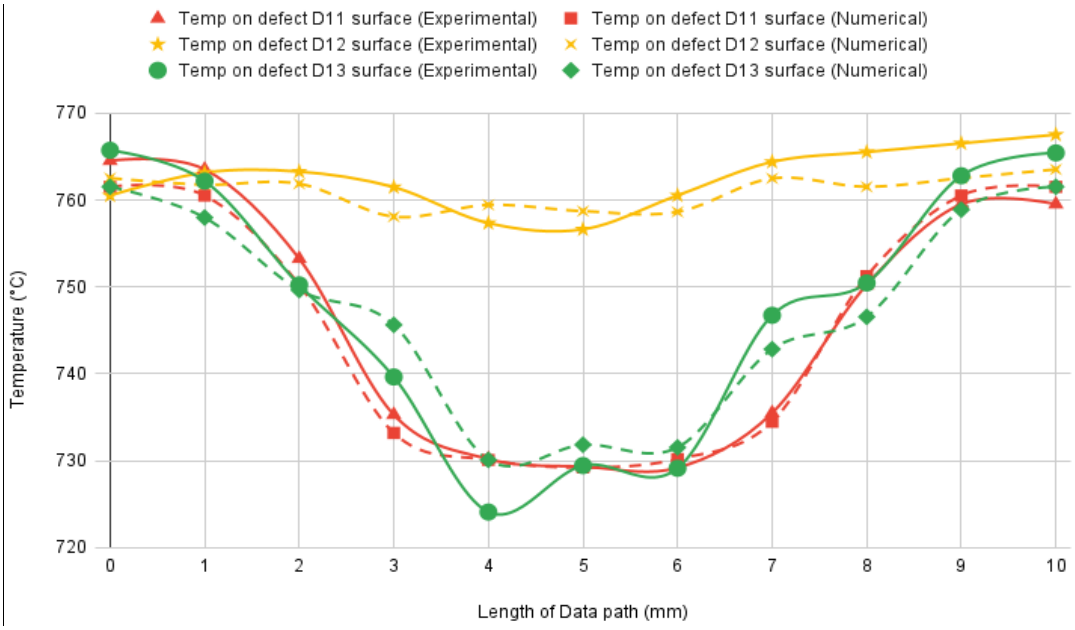

Figure 5-4: Temperature distribution on δ based defect surfaces without GW after 7 seconds of cooling period.

5.1.5.1.2 Set One Simulations – with Glass Wool (GW)

Simulations had been performed on sample with glass wool being introduced in the sample holes as per specifications given in Fig. 4-5. Temperature dependent material properties of glass wool are chosen from ANSYS Material Library. Fig. 5-5 shows the comparison of numerical and experimental temperature data obtained after 7 seconds during the cooling period on defect locations. Defects D11 and D13 showed ΔT_{num} of 21°C ($\Delta T_{min} \approx 15.5$ °C at 776 °C) and 38 °C ($\Delta T_{min} \approx 15.6$ °C at 778 °C), hence making D11 and D13 to be detectable by the IR camera. Defect D12 cannot be detected as ΔT_{num} (4 °C) < ΔT_{min} (15.5 °C at 777 °C).The maximum deviation, ΔT_{en} obtained was only 7 °C which is due to emissivity correlation error, or IR camera sensitivity error from experiments.

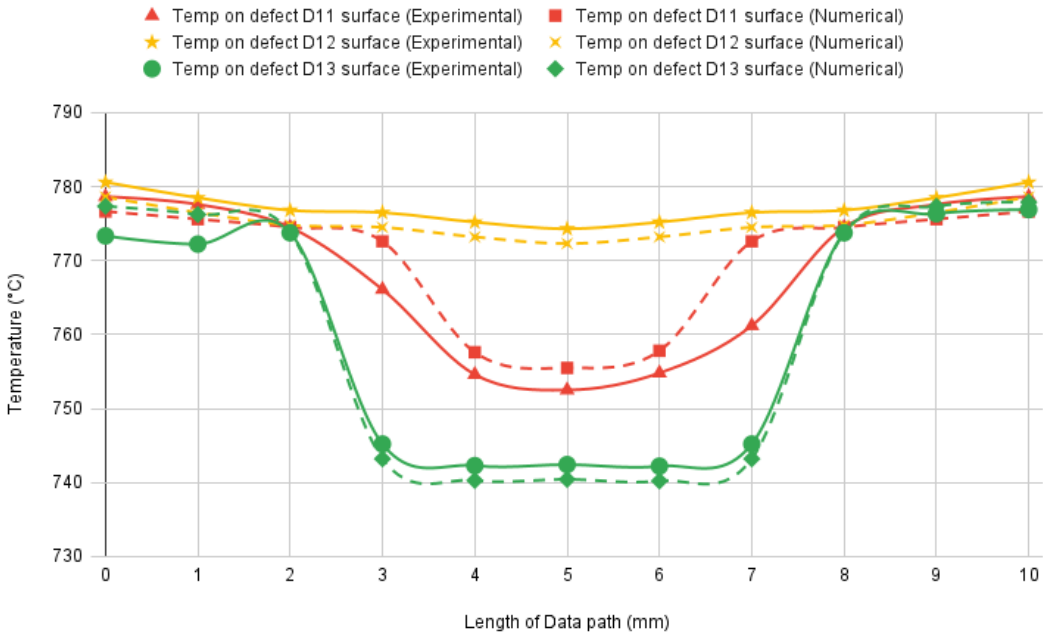

Figure 5-5: Temperature distribution on δ based defect surfaces with GW after 12 seconds of cooling period.

5.1.5.2 Results of the Second Set of Defects – Effect of D_h

5.1.5.2.1 Set Two Simulations – Without Glass Wool (GW)

Simulations had been performed on samples with second set of defects without GW and temperature data was assessed using data paths of 5 mm. Similar to the first set, no temperature difference on sample defect surfaces was recorded during heating period. Fig. 5-6 shows the thermal simulation image obtained

at 9 seconds of cooling period where defect D22 showed a considerable ΔT_{num} of 26.3 °C and which can be detected by the IR camera based on its corresponding detectability limit (~15.7 °C at 783 °C). Defects D21 and D23 showed a ΔT_{num} of 4 °C and 11 °C, which the IR camera cannot detect. However for D23, from experimental results ΔT_{exp} = 17 °C, which the IR camera was able to detect, but numerical results only showed 11 °C. Fig. 5-7 shows the comparison of temperature distribution data obtained on the sample defect surfaces with D_h based defects experimentally and numerically after 9 seconds of cooling period. The deviation ΔT_{en} obtained was only 6 °C, which can be due to emissivity correlation error or camera sensitivity error caused during experiments.

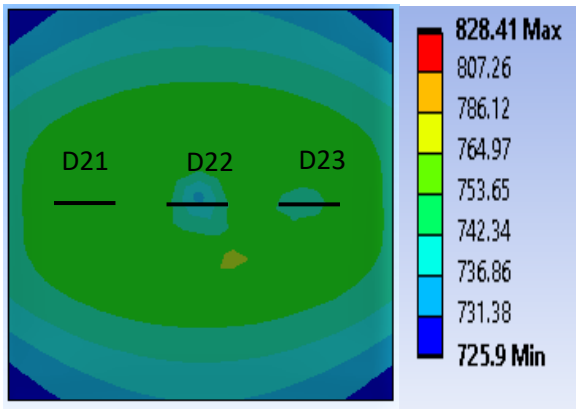

Figure 5-6: Thermal Simulation image obtained during the test conducted on the D_h based defects without glass wool after 9 seconds of cooling period.

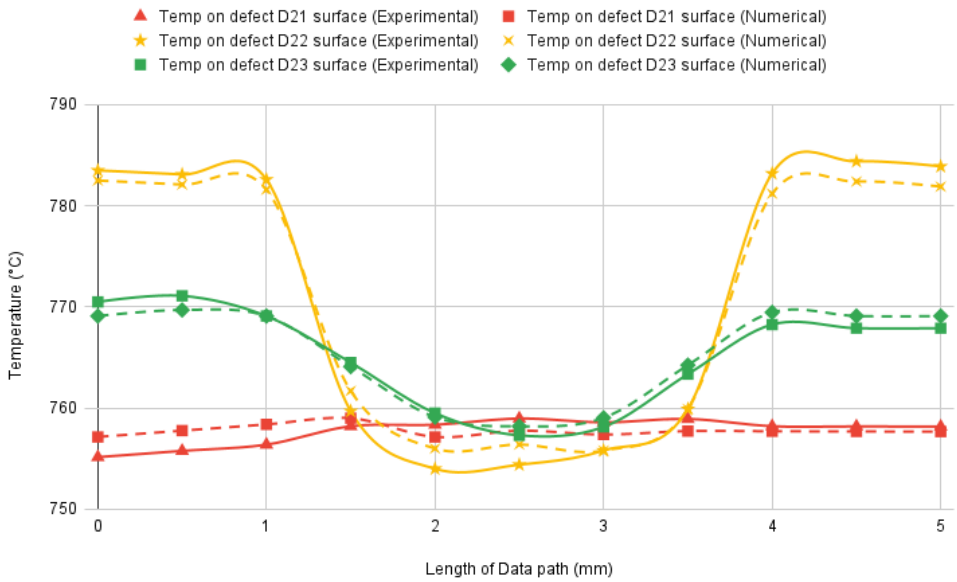

Figure 5-7: Temperature distribution on D_h based defect surfaces without glass wool after 9 seconds of cooling period.

5.1.5.2.2 Set Two Simulations – with Glass Wool (GW)

Simulations had been performed on samples with D_h based defects with GW inserted as in Fig. 4-7. Thermal simulation Image obtained after 14 seconds of cooling period was shown in Fig. 5-8. Numerical data obtained was compared with the experimental data collected on D_H based defects with glass wool as shown in Fig. 5-9. The obtained numerical results showed that only defect D22 showed a sufficient ΔT_{num} of 22.1 °C on the surface that can be detected by the IR camera based on its detectability threshold (~15 °C at 750 °C). Same as in experiments, D21 and D23 defects showed very less ΔT_{num} of 2 °C and 8 °C respectively which the IR camera cannot detect.

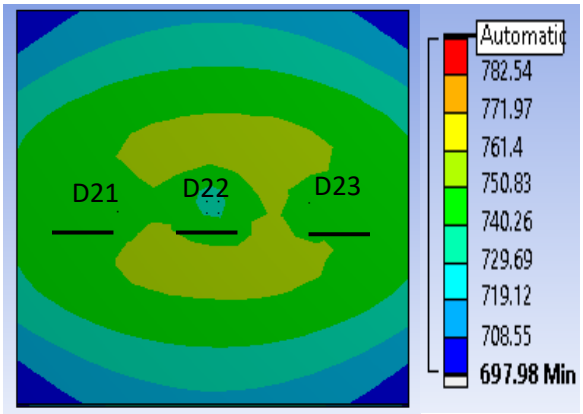

Figure 5-8: Thermal Simulation image obtained during the test conducted on D_h based defects with GW after 14 seconds of cooling period.

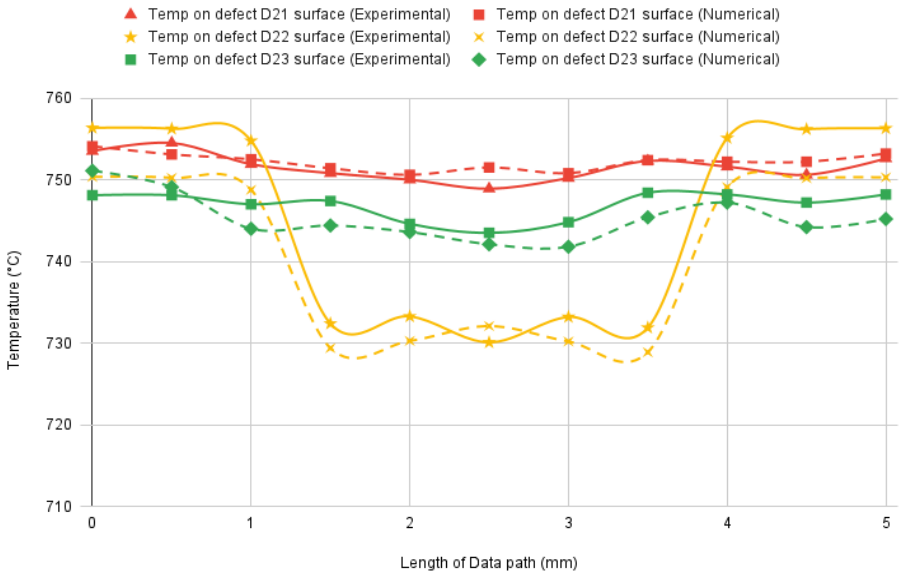

Figure 5-9: Temperature distribution on D_h based defect surfaces with GW after 14 seconds of cooling period

5.2 Numerical Modelling of Laser Welding Operations

Laser welding is one of the advanced and effective welding methods to join metals. Unlike, conventional methods, e.g., arc or plasma welding, laser welding does not require any filler material. As a matter of fact, the output energy from the laser beam source is very high compared to arc or plasma. In this regard, many deep and tapered welds can be generated at the joint, without much spatter. Since laser welding experimental setup is expensive and relatively hard to perform, computational simulations to study the welding behavior would be ideal, before manufacturing. GuoMing [32] performed laser welding simulation on SS 304 L using a floating heat source model. To reduce the computational cost, only half of the work piece is simulated due to symmetricity. The weld zone measurements, depth, and width of penetration etc. were in agreement with experiments performed using a PRC4000 CO_2 laser welder. Different computational strategies had been performed for laser welding with experimental validation which helped a lot to perform simulations [33-38].The movement of heat flow during the welding process is numerically given by the heat flow equation (5.1).

$$\rho C_p \frac{\partial T}{\partial t} + \rho C_p v \nabla T + \nabla q = h_f \qquad (5.1)$$

Where

ρ $[g/mm^2]$ = density of the working metal as a function of temperature,

$C_p[J/(g.K)]$ = specific heat of the working metal as a function of temperature,

T $[K]$ = Temperature in the vector field,

v $[mm/s]$ = velocity field,

q $[W/mm^2]$ = heat flux lost to surroundings due to a combination of conduction, convection, and radiation,

h_f $[W/mm^2]$ = heat flux of laser source.

The heat lost to surroundings is given by the equation (5.2).

$$-q = \varepsilon\sigma\,(T_r^4 - T^4) + h(T_r - T) \qquad (5.2)$$

Where

ε = Emissivity of metal surface (0.3 for Aluminum and 0.5 for Titanium),

σ = Stephen Boltzmann Constant i.e. $5.67 \times 10^{-8}\ W/(m^2.K^4)$,

T_r = Room temperature i.e. 293 K,

h = convective heat transfer coefficient i.e. 20 $W/(m^2K)$ for air, and 200 $W/(m^2K)$ for the bottom surface.

5.2.1 Validation of the Heat Source Model

D'Ostuni et al. [39] performed laser welding simulations using 2D and 3D Gaussian heat source distribution models. It was performed on two dissimilar metals Aluminum (AA5754 grade) and Titanium (Ti6Al4V grade). Temperature-dependent material properties were considered for both titanium and aluminum grades. Emissivity was assumed to be constant for both metal surfaces; 0.5 for Ti6Al4V and 0.3 for AA5754. Convection heat transfer coefficient for air loss is considered constant of $20\mathrm{W}/(\mathrm{m}^2\mathrm{K})$. Since the bottom surface of the plates would be in contact with a support base plate, heat transfer coefficient was considered $200\mathrm{W}/(\mathrm{m}^2\mathrm{K})$. Contact conductance of $30{,}000\mathrm{W}/(\mathrm{m}^2\mathrm{K})$ was used near the two metal plate's intersection. Adaptive meshing technique was used to obtain very fine mesh near the weld region. COMSOL Multi-physics is used for FEA solver purposes. Experiments were performed using an YLS-CUT laser welding machine by IPG Photonics [40]. The technical specifications of the laser welding machine were shown in Table 5-1. The laser beam was deposited at a distance of 1 mm on the titanium plate from the center of both plates. This is because aluminum had a relatively low melting temperature, it could vaporize the metal if deposited along the centerline. Also, thermocouples were placed on both the plates at a distance of 2 mm for the centerline, to monitor the temperature distribution during welding.

Table 5-1: IPG Photonics YLS-4000 Specifications [40].

Characteristic feature	Value
Max output Power	4 kW
Output fiber diameter	200 µm
Beam parameter product	6.3 mm·mrad
Wavelength	1.07 µm

5.2.2 2D Gaussian Heat Source model for thin plates

An ANSYS APDL finite element code for 2D Gaussian distribution created was used for laser heat source model for finite element method in ANSYS Mechanical. The method of heat distribution using this model takes place by surface. The moving laser heat source model based on 2D Gaussian distribution used in this works for thin plate welding is as shown in the Fig. 5-10 below.

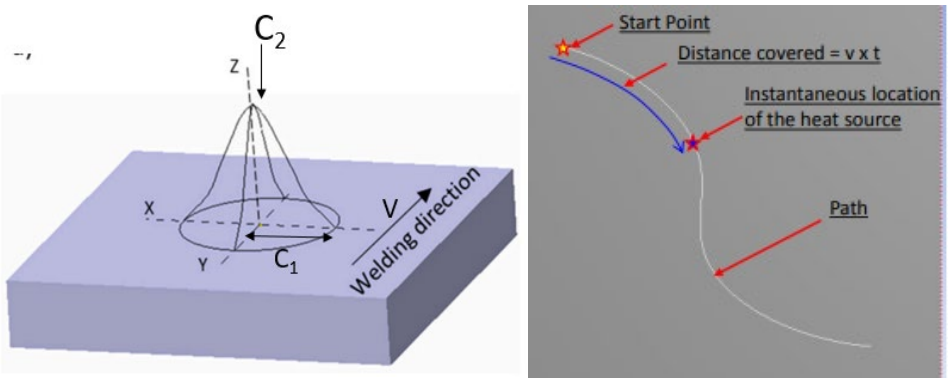

Figure 5-10: 2D Gaussian surface laser heat distribution model [41].

The equation for 2D heat flux for the laser source model for thin plate welding based on equation (5.3) as shown is substituted in the welding heat flow equation (5.1) for simulation analysis.

$$h_f = C_2 e^{\frac{-[(x-x_0)^2+(y-y_0)^2+(z-z_0)^2]}{C_1^2}} \quad (5.3)$$

Where,

h_f = desired heat flux in W/mm^2,

C1 = radius of the beam in mm,

C2 = Weld torch power intensity in W,

(x_0, y_0, z_0) = instantaneous position of the center of the heat flux along the weld path,

V = Velocity of moving heat source in mm/sec,

t = welding time in a sec,

(x, y, z) = welding starting location.

This model is limited to thin plates as volumetric heat considering depth is not used. Since the actual welding process is not static; the Transient Thermal module in ANSYS is to perform accurate analysis and

attain results. This heat source model is validated with the FEA code written and compiled using COMSOL Multiphysics from the work done by D'Ostuni et al. Fig. 5-11 shows the temperature profile of the 2D laser heat source. The shape of the weld pool perfectly simulated the laser beam without producing any teardrop like in reference work.

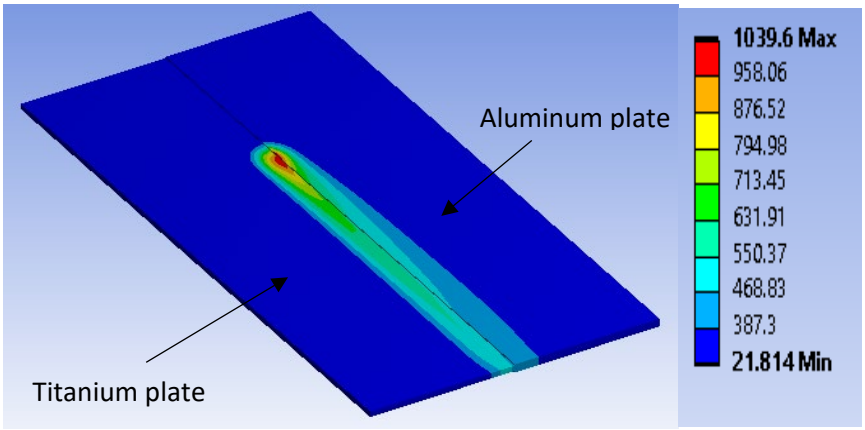

Figure 5-11: Temperature distribution using 2D Gaussian heat source model on Al-Ti plates.

Temperature data were recorded at a distance of 50 mm from the start point, at a distance of 2 mm from the weld centerline as shown in Fig. 5-12. This is because the laser beam takes some initial time to attain quasi-steady condition. Data were recorded and compared with the experimental and numerical data provided in work done by D'Ostuni et al.

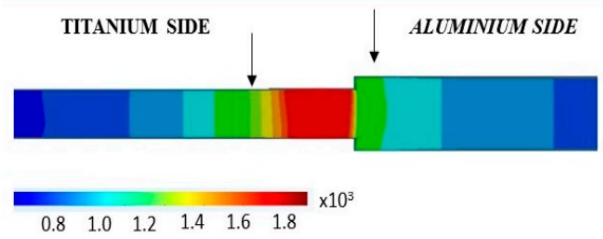

Figure 5-12: Position of data point at a distance of 2 mm from weld centerline [39].

The temperature cycle for the 2D Gaussian heat source model for Titanium and Aluminum plates is labelled as current results in Fig. 5-13 and Fig. 5-14. The results showed a good agreement with experimental and numerical work done by D'Ostuni et al. During the cooling phase, current results were more aligned to their experimental work when compared to their numerical work. This says that the heat

source model used was very reliable for temperature analysis and its weld pool shape obtained is alike with real weld pool shape, unlike teardrop.

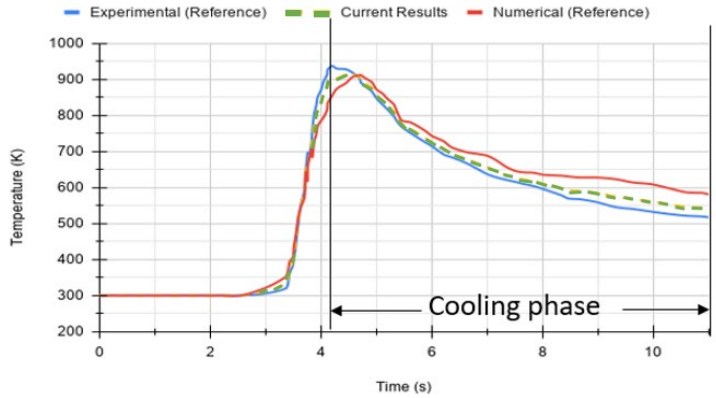

Figure 5-13: Numerical thermal cycle validation using 2D Gaussian heat source model for Ti plate.

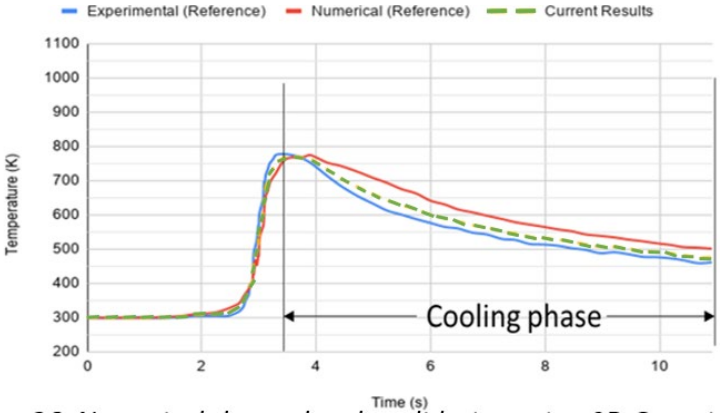

Figure 5-14: Numerical thermal cycle validation using 2D Gaussian heat source model for Al plate.

5.2.3 3D Gaussian Heat Source model for thick plates

Numerical simulations had been performed using a 2D heat source model for thick stainless steel plates of 5, 10, and 15 mm to check if the effect of depth is valid. Fig. 5-15 (a), (b), and (c) shows the images of 2D heat source moving on Al plates of 5, 10 and 15 mm in thickness. All the laser-based welding parameters were optimized accordingly to attain melting temperatures near the weld zone for these plates. However, since the 2D heat source model is only a surface model, it hasn't produced any feasible results for plates above 5 mm.

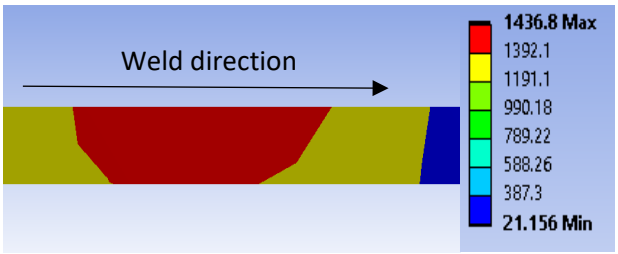

Figure 5-15 (a): Weld zone for 5 mm plate using 2D heat source.

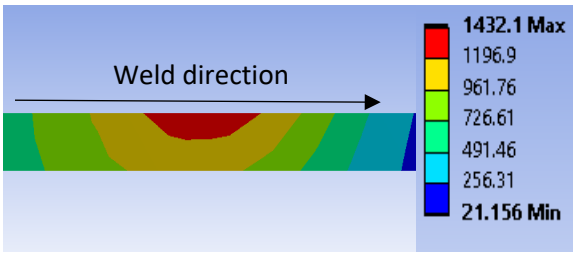

Figure 5-15 (b): Weld zone for 10 mm plate using 2D heat source.

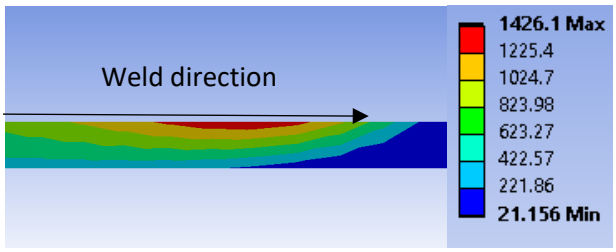

Figure 5-15 (c): Weld zone for 15 mm plate using 2D heat source.

As shown in Fig. 5-15 (b) and (c), the weld zone is complete only for a plate of thickness 5 mm, which makes the simulation non-feasible for plates above 5 mm thickness in welding process. In this connection, a 3D moving heat source model which can not only take the effect of weld radius, but also the depth of the weld pool is developed using 3D Gaussian distribution is chosen as in Fig. 5-16.

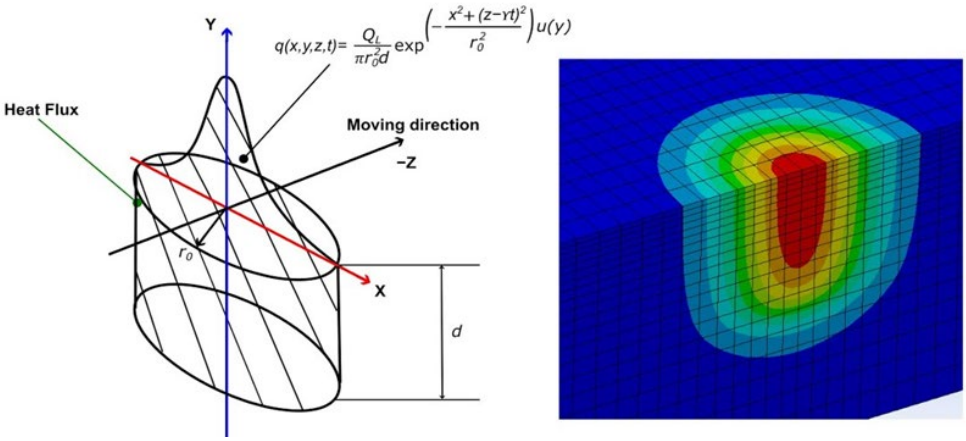

Figure 5-16: 3D Gaussian moving laser heat source model [42].

The equation for 3D moving laser heat source model used in this work for thick plates above 5 mm is based on equation (5.4) given.

$$h_f(x,y,z,t) = \frac{Q_L}{\pi r_0^2 d} e^{(-\frac{x^2+(z-yt)^2}{r_0^2})u(y)} \qquad (5.4)$$

Where,

$h_f(x, y, z, t)$ = 3D Gaussian laser heat flux distribution in W/mm^2

Q_L = Laser power in W,

r_0 = radius of the laser beam in mm,

d = depth of penetration of laser source in mm,

u (y) = welding speed in y-direction,

(x, y, z) = welding start position,

t = welding time.

An ANSYS APDL program was written based on 3D Gaussian heat distribution and to show the model used in this work is rational, validation was done with a 3D heat source model which was developed by D'Ostuni et al. Fig. 5-17 shows the 3D Gaussian heat source model for welding of Ti-Al plates. From the temperature distribution profile, though the welding is taking place along the titanium plate, it is clear that the heat transfer rate is relatively higher on the aluminum side than the titanium plate. This is because of the higher thermal conductivity of aluminum when compared to titanium.

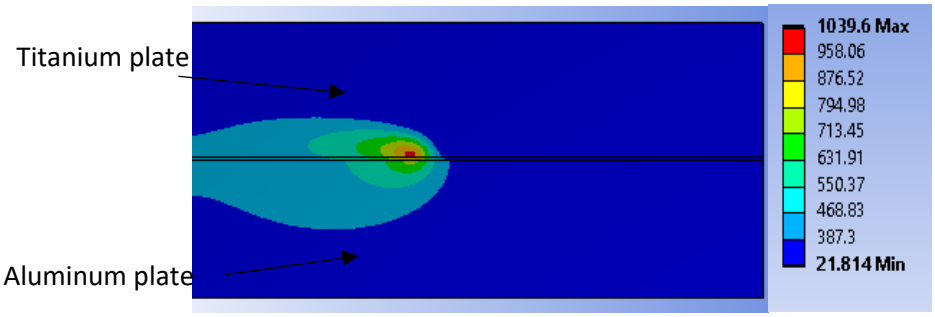

Figure 5-17: Temperature distribution using 3D Gaussian heat source model on Al-Ti plates.

Temperature data was collected at a distance of 2 mm from the weld centerline and 50 mm from the start point. This temperature cycle is compared and validated with experimental and numerical work done in reference work as shown in Fig. 5-18 and Fig. 5-19. It was evident that the temperature measurements during both the welding and cooling phase were in line with the experimental and numerical data collected from the reference work.

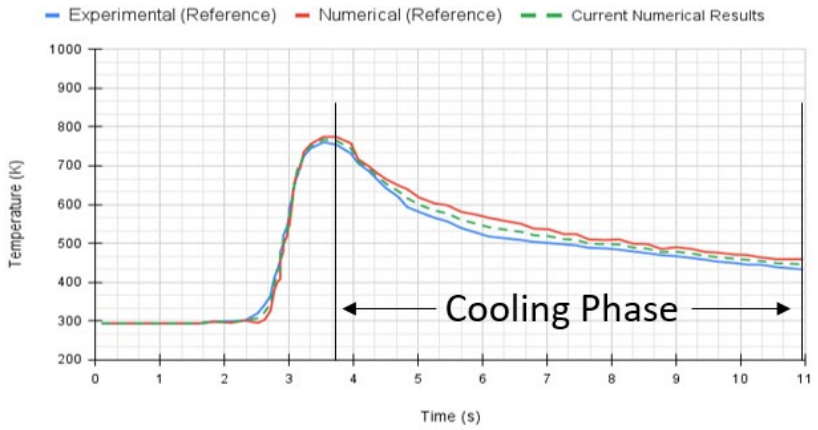

Figure 5-18: Numerical thermal cycle validation using 3D Gaussian heat source model for Al plate.

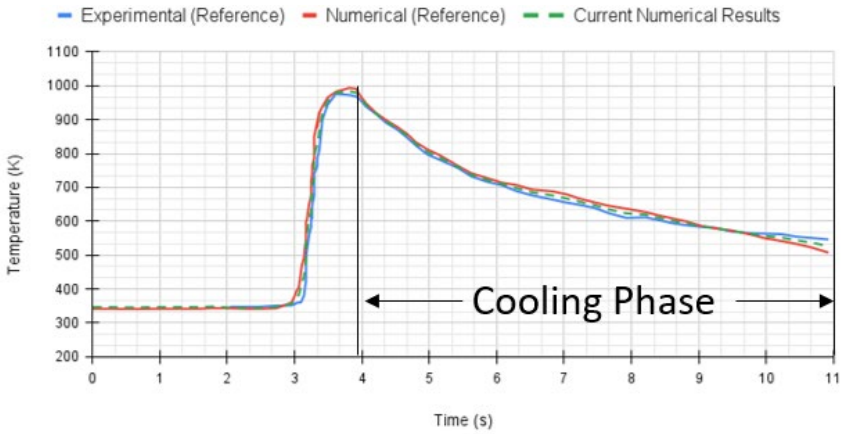

Figure 5-19: Numerical thermal cycle validation using 3D Gaussian heat source model for Ti plate.

Simulations were conducted on 10 mm and 15 mm stainless steel plates to see if the temperature profile was feasible for the whole plate thickness. Weld zone temperature profiles for 10 mm and 15 plates using 3D Gaussian laser heat source model are shown in Fig. 5-20 (a), and (b). Heat affected zone (HAZ), also called weld bead profile, shows complete penetration depth for effective welding. In this regard, the heat source model used in this work is validated and proven to work for thick plates.

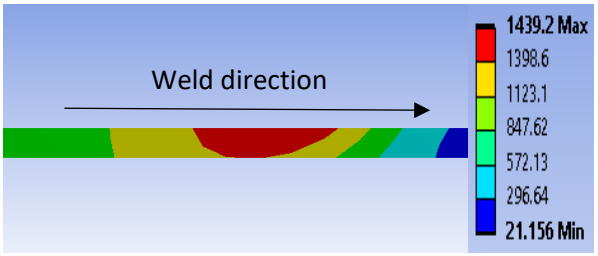

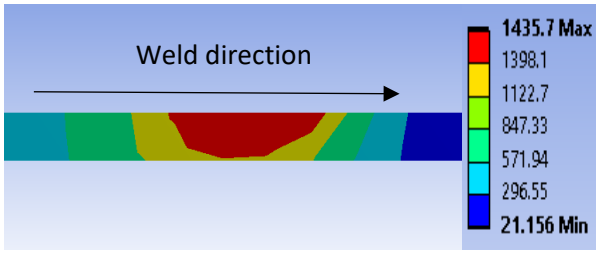

Figure 5-20 (a): Weld zone for 10 mm plate using 3D heat source *Figure 5-20 (b): Weld zone for 15 mm plate using 3D heat source*

5.3 Identification of defects within the weld zone during laser welding

Since experiments cannot be conducted to assess inhomogeneity and geometrical based defects using laser-based welding systems, computational simulations were performed. In this section, numerical simulations of welding operations of two Stainless Steel 304L plates – thin (5mm thickness) and thick (15 mm thickness), with and without defects were compared and the extent to which these defects can be detected depending on size and location. In this connection, the effect of emissivity of material during the cooling phase after welding is very crucial for IRT study. From the emissivity graph calculations done for FM-SS and RM-SS samples, the tests show only results till 800 °C. However, welding operations take place for steel take place anywhere between 1300°C – 1500 °C depending on grade. For stainless steel, the melting point is between 1399 °C (solidus) – 1425 °C (liquid). So based on the graphs obtained during the calibration test between 50 °C – 800 °C, emissivity graph for stainless steel samples had been extrapolated for temperatures between 800 °C – 1450 °C as shown in Fig. 5-21.

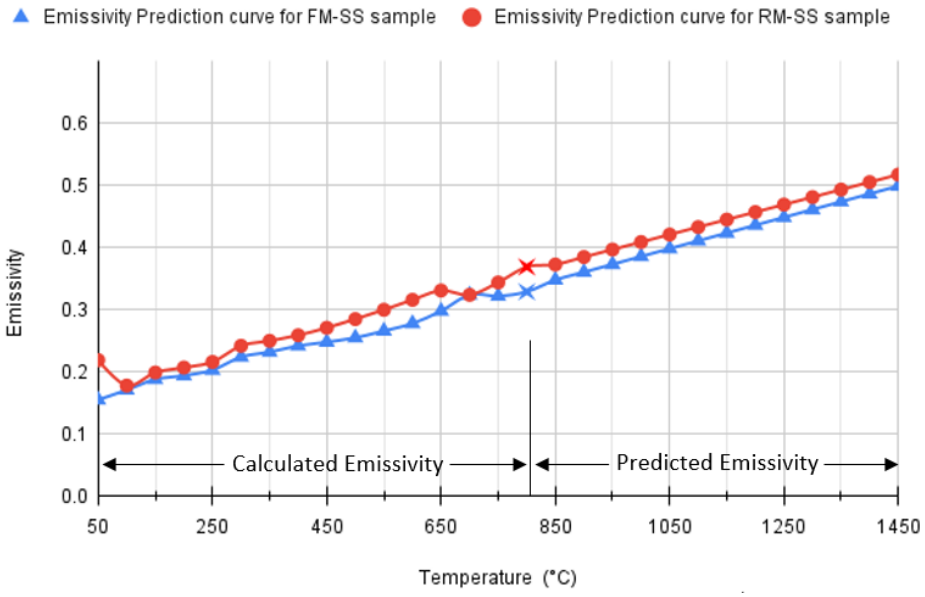

Figure 5-21: Predicted Emissivity graph for SS samples.

5.3.1 Defect detection in thin plates

2D Gaussian heat source model is used for simulation of thin SS plates. As there is no filler material used in laser welding, no material combination for thermo-mechanical behavior assessment is used. Temperature-dependent mechanical and thermal properties of stainless steel were used for transient thermal study in ANSYS. Temperature dependent convective heat transfer coefficient for air is used for convection heat loss from all the exposed plate faces. A predicted emissivity graph obtained for FM-SS sample was used as radiative heat loss. Based on the data specification provided for welding 5 mm thick stainless steel plates by IPG YLS 4000 laser welding machine [40], moving heat flux parameters used for laser welding operation were shown in Table 5-2 below.

Table 5-2: Laser parameters for welding 5 mm thick SS plates.

Parameter	Value
Power	0.75 kW
Welding Speed	10 mm/sec
Radius of beam	2 mm
Laser Specifications	1.07 μm, Infrared

5.3.1.1 Material based Inhomogeneity defects

One of the ordinary defects formed during laser welding is porosity. Porosity refers to the inclusion of cavities in the weld metal caused by the trapping of gases released from the molten metal in the weld zone as it solidifies. These defects may form either on the surface or inside the metal pool. Slag inclusion, another problematic issue in the welding process, refers to the entrapment of small volumes of flux be it gas, or foreign material which prevents complete penetration of the weld for its depth. Incomplete fusion is a discontinuity defect that occurs between molten weld metal and fusion faces. This defect results in cracking and breakage of the weld joint. Whereas identification of surface defects like an undercut, spatter, misalignment or distortion defects is easy using a Laser-based weld defect detection (LBWDD) system, identification of all these in-metal defects in real-time during welding is quite hard using this NDT

technique. So the incorporation of a Thermal-Imaging-based weld defect detection (TIBWDD) system would be innovative.

Thin Stainless Steel plates of (50 x 5 x 200) mm were used for welding simulations. To study the degree to which defect sizes inside the plates can be predicted using the TIBWDD system, various square defects on different sizes as shown in Table 5-3 and depths as shown in Fig. 5-22 were placed at the weld region. The size of the defects and depth at which they were created is based on second set of defects that were considered in Chapter 4. Simulations were also performed on thin plates without any defects and the temperature distribution was compared with the plates with weld defects obtained on the surface.

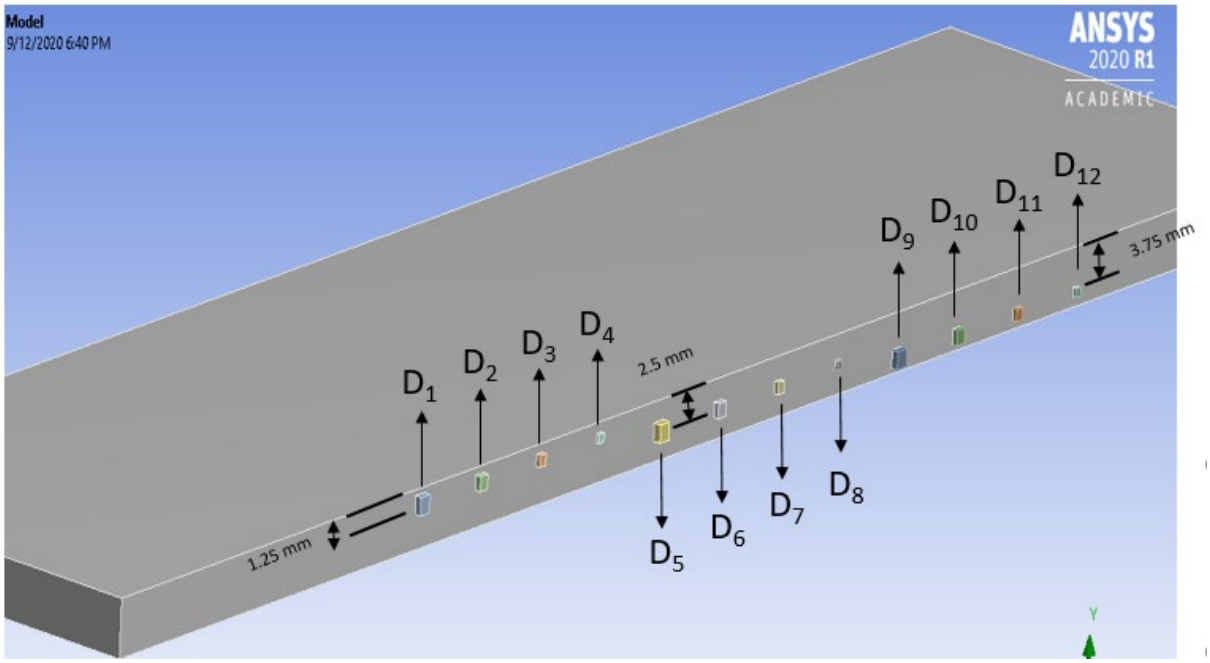

Figure 5-22: Position of defects and their location in a thin SS plate defective model.

Table 5-3: Size of defects in thin SS plates.

Name of Defect	Each side length of the square defect
D1	1.5 mm
D2	1.25 mm
D3	1 mm
D4	0.75 mm
D5	1.5 mm
D6	1.25 mm
D7	1 mm
D8	0.75 mm
D9	1.5 mm
D10	1.25 mm
D11	1 mm
D12	0.75 mm

Data paths each of 10 mm were placed on the defect location surfaces for defective and non-defective plate models. Data were collected with a sampling distance of every 0.25 mm to maintain accuracy. The position of the data path over the defect location surface was shown in Fig. 5-23 below.

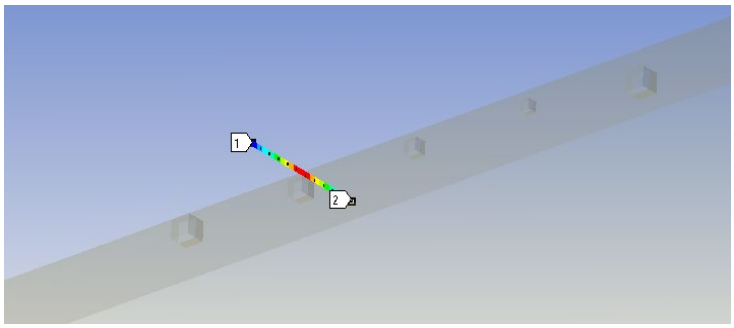

Figure 5-23: Position of data path on the surface of defective model on D2.

Temperature data were recorded for both the plate with and without defects for every 0.1 sec to predict when these defects can be captured by the TIBWDD system. Fig. 5-24 shows the maximum temperature difference (ΔT) captured from the numerical analysis at the data path above defect D1 at 6.5 sec. It was evident that a positive ΔT of 220°C was recorded on the plate with a defect inside. This is because the thermal diffusivity of air is very less compared to steel, and showed a temperature imbalance on the surface. Similarly, temperature distribution graphs were plotted for other defects like D2, D5, and D6

located at various depths. From the graphs, it was clear that the defects that are closer to the surface are more likely to show up, where are deeper they are, harder it is to be captured by the TIBWDD system.

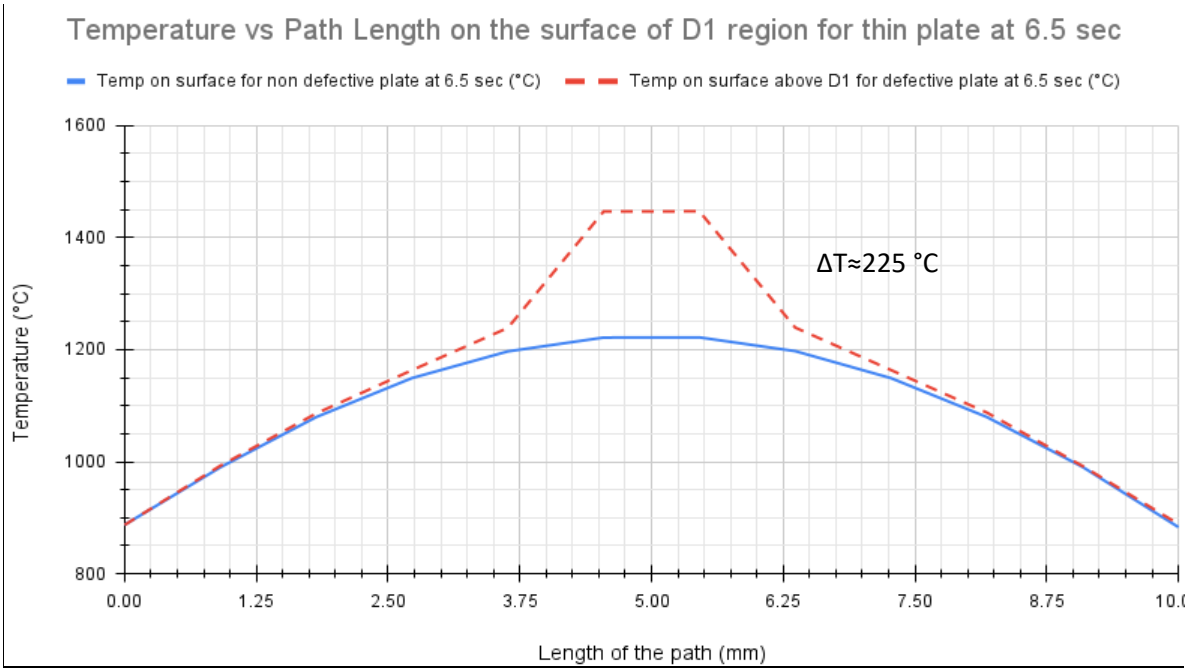

Figure 5-24: Temperature comparison graph between defective and non-defective models on the surface above D1 at 6.5 sec

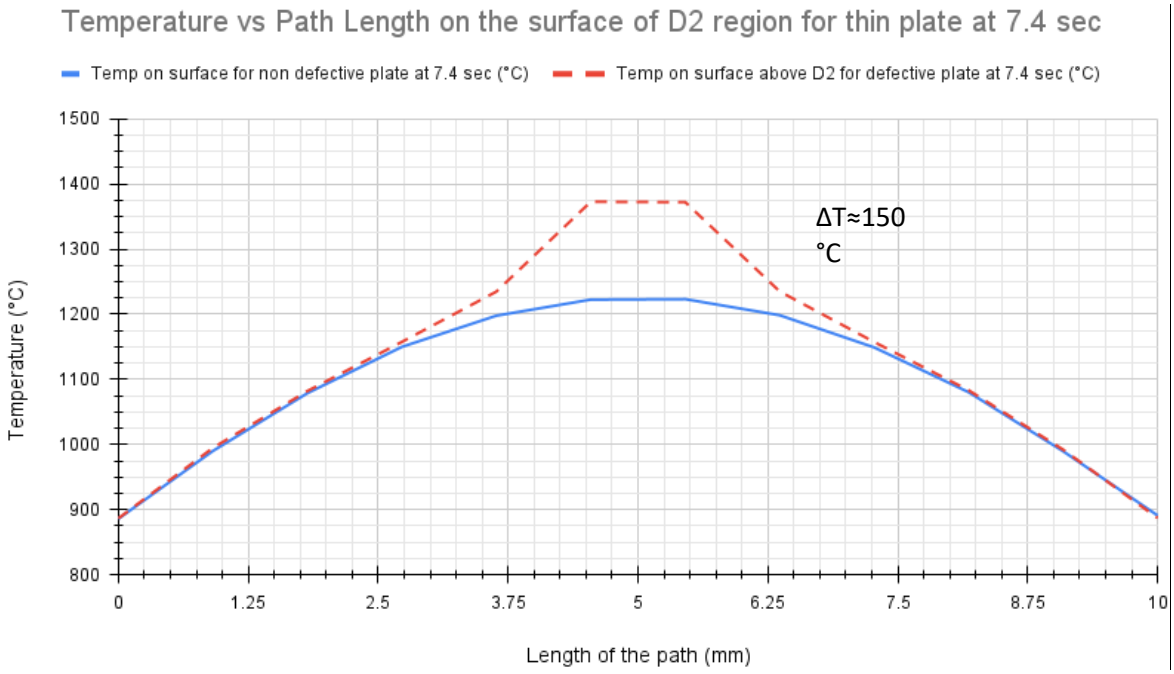

Figure 5-25: Temperature comparison graph between defective and non-defective models on the surface above D2 at 7.4 sec.

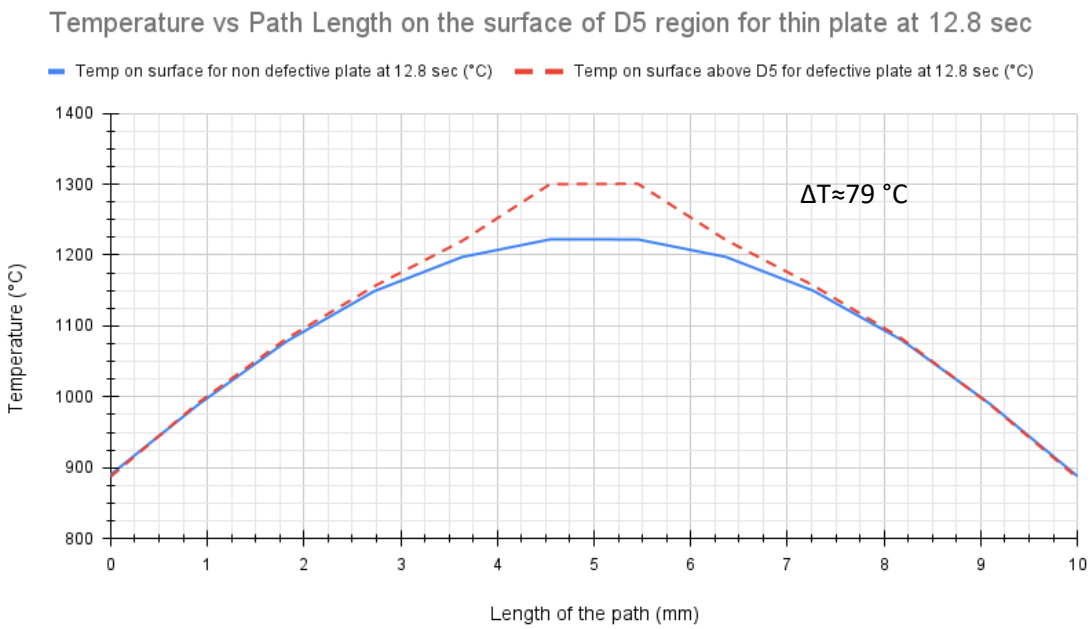

Figure 5-26: Temperature comparison graph between defective and non-defective models on the surface above D5 at 12.8 sec.

From the Fig. 5-24 and Fig. 5-26 above, even though defects D1 and D5 are of the same size and shape, it clearly shows that the deeper they are, the less ΔT it made on the surface. For the defect D6 with a square side of 1.25 mm, only ΔT ≈ 25°C was captured on the defect plate as shown in Fig. 5-27.

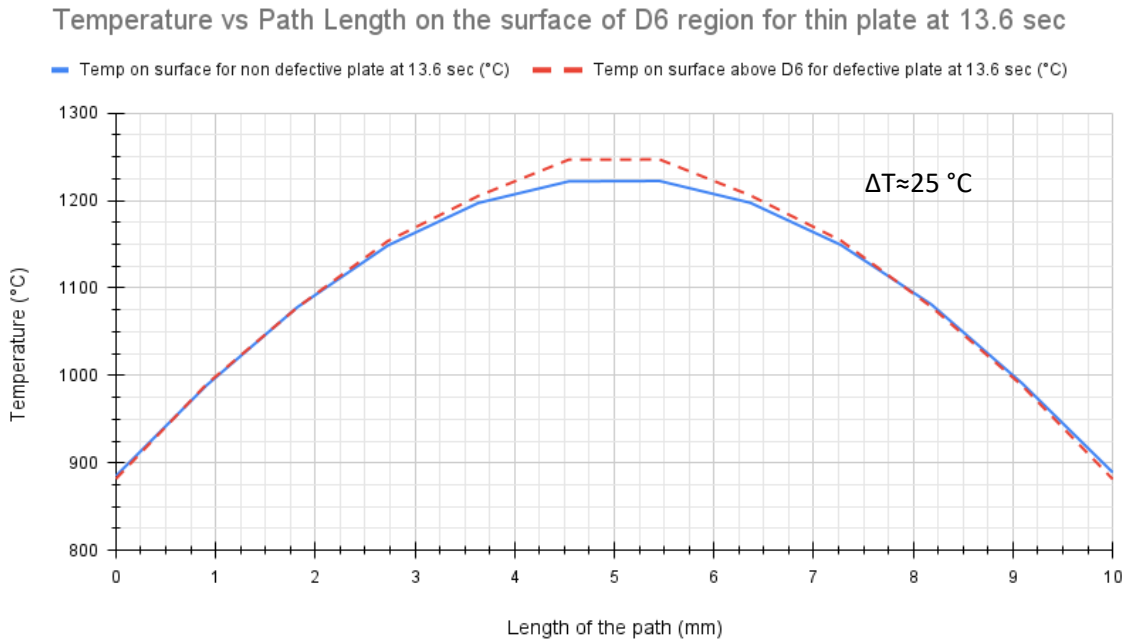

Figure 5-27: Temperature comparison graph between defective and non-defective models on the surface above D6 at 13.6 sec.

Similarly, temperature data was recoded for all the defects at their surfaces at different time steps. The time at which maximum temperature difference observed on defect plate when compared to non-defective plate is shown in Table 5-4. The spot detectability threshold that the IR camera needed as per specifications is 2 °C per 100 °C. So, for the working welding temperatures of 1400 °C – 1500 °C, the maximum temperature that difference a camera can fail to detect is calculated.

Defect Detectability limit (ΔT_{min}): 2 % = (1500*20)/100 = 30 °C.

So for all the temperature differences above 30 °C between welding temperatures of 1400 °C – 1500 °C, the camera can be able to detect them.

Table 5-4: Detectability of material based defects in thin SS plates at various location.

Name of Defect	ΔT on surface (°C)	Detectability
D1	224.9	Yes
D2	150.2	Yes
D3	86.5	Yes
D4	39.3	Yes
D5	78.6	Yes
D6	24.9	No
D7	7.3	No
D8	2.6	No
D9	5.9	No
D10	2.8	No
D11	1.4	No
D12	0.6	No

It was clear that all the defects that are located at a depth of 0.25 mm from the surface (D1, D2, D3, and D4) can be captured by the TIBWDD system (as per XIRIS XI 400 camera threshold). Whereas, except D5 which is located at 2.5 mm depth and 1.5 x 1.5 mm in size, no other defects produced sufficient ΔT on the surface to be detectable.

5.3.1.2 Misalignment defects

The other application where the TIBWDD system can be incorporated during continuous welding is for the identification of misalignment defects. The existing laser-based system can detect these defects but

is limited to the scanning area. Since the LBWDD system is a point source laser, it cannot detect misalignment defects over the weld region area. So TIBWDD system would be able to capture these defects in during welding operations so that the plates can be corrected for feasible pipe manufacturing. Tests had been conducted on two different misalignment defects – Step Misalignment defects, and Inclined Misalignment defects.

1. Step Misalignment Defects:

Computational Simulations using a 2D Gaussian heat source model had been performed on thin Stainless Steel plates with different misalignment error values. Table 5-5 shows different misalignment errors considered for detection of these defects using 2D heat source model. Fig. 5-28 shows the geometry of the welding plates with an error of 2 mm.

Table 5-5: Misalignment values for step misalignment detection.

Misalignment models	Error Value
2D-SM-0.5	0.5 mm
2D-SM-1.0	1.0 mm
2D-SM-1.5	1.5 mm
2D-SM-2.0	2 mm

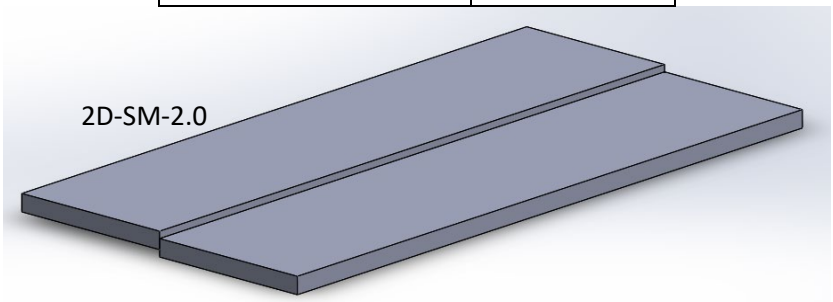

Figure 5-28: Step Misalignment defect of 2 mm error along the weld region of thin SS plates.

Simulations had been performed on all the misalignment plate models with different error values and temperature was recorded on the surface at a distance of 60 mm from the start position. This is to ensure that the moving laser heat source attains a steady welding temperature of about 1399 -1425 °C. Fig. 5-29 shows the temperature distribution on the surface of misaligned plate models at 7.5 sec.

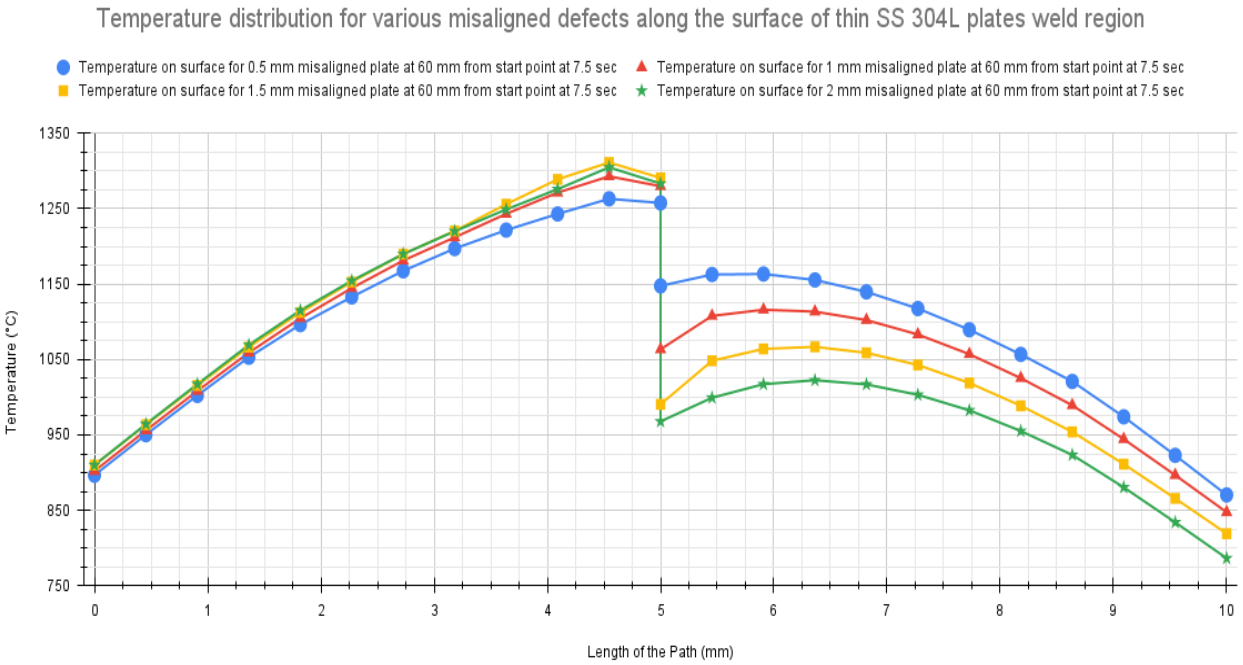

Figure 5-29: Temperature distribution of various step misaligned plates on weld surface of thin SS plates.

Table 5-6 shows the minimum temperature difference (ΔT) obtained on the step misaligned welded thin plates that can be detected by the TIBWDD system based on its sensitivity error.

Table 5-6: Detectability of step misalignment defects in thin SS plates

Misalignment models	Min ΔT °C	Detectability
2D-SM-0.5	98.6	Yes
2D-SM-1.0	178.2	Yes
2D-SM-1.5	241.5	Yes
2D-SM-2.0	284.8	Yes

The results showed that all the step misaligned defect models, whenever they had an error, the TIBWDD system can capture it. This is because the laser beam is very focused to a certain radius and this results in overshooting the temperature on the upper plate and undershooting the lower plate which causes thermal imbalance and poor welding quality. So further evaluation had been done to identify what minimum value of deflection error is required for the TIBWDD system for defect identification using Inclined Misalignment defects in the below section.

2. Inclined Misalignment Defects:

Inclined Misalignment is another common type of defect encountered during continuous pipe welding. These defects arise when there's a shift in the roller's position or angle. However, there is need a need for an online weld seam monitoring system that can capture these defects in real-time so that this error can be fixed. The accuracy to which the TIBWDD system can identify these defects is analyzed using two plates with an overall inclined misalignment of 0.5 mm. Computational simulations were performed using a 2D laser heat source model on thin plates of 50 x 5 X 200 mm each with a gradually inclined error of 0.5 mm as shown in Fig. 5-30.

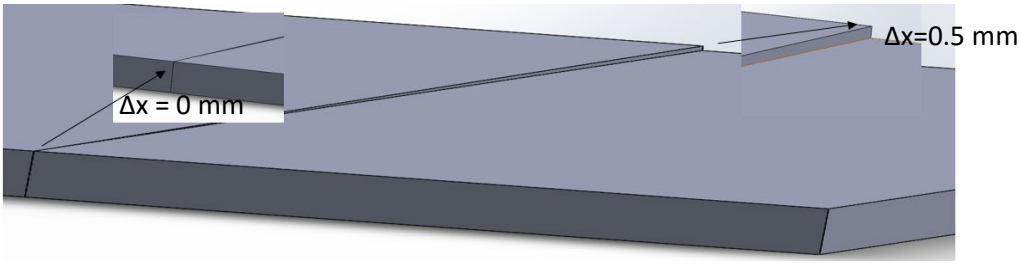

Figure 5-30: Inclined misalignment defect of 0.5 mm error along the weld region in thin SS plates.

Temperature data was recorded at the weld region on the plate surfaces by the TIBWDD system at every 20 mm at respective time steps with 0.5-sec delay after welding, from the start position using data paths. Fig. 5-31 shows the temperature data obtained on the surface on the inclined plates.

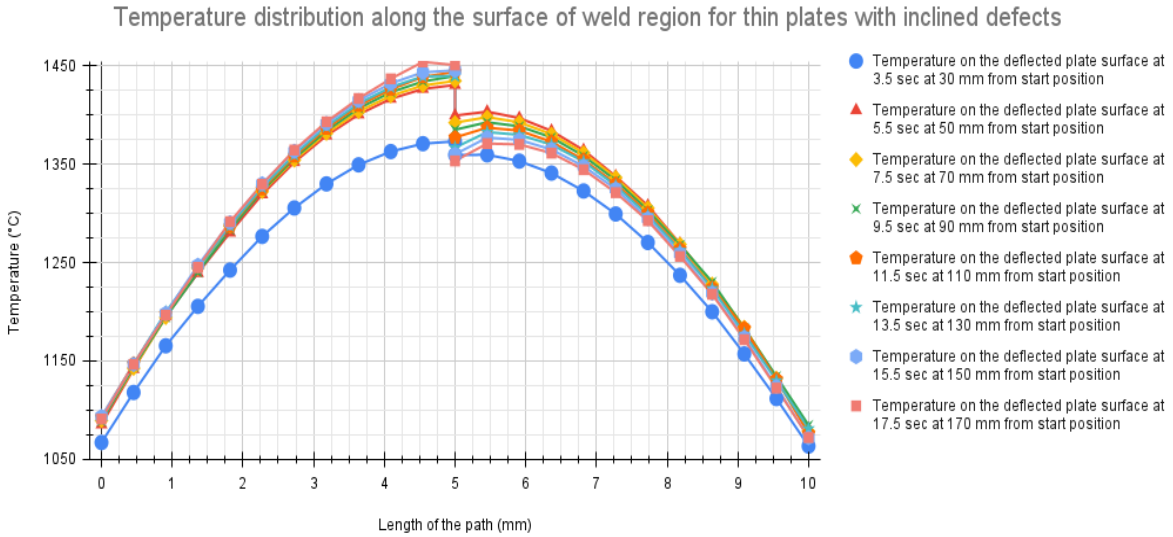

Figure 5-31: Temperature distribution curve of inclined misalignment defects on the surface of thin SS plates at various locations

The ΔT created by the laser source when falling on inclined plates and considering the sensitivity of the TIBWDD system, the extent to which these defects can be detected is shown in Table 5-7. From the results it was clear that at a location of 110 mm from the start point where the deflection is 0.275 mm at the weld centerline, a temperature difference of 51.2 °C is recorded on the surface. So, if the TIBWDD system is provided with the emissivity function for FM-SS steel and properly calibrated, this deflection can be detected, and the moving rollers can be adjusted to fix this issue during pipe welding.

Table 5-7: Detectability table for inclined misalignment defects for thin SS plates.

Distance from weld start region (mm)	Plate deflection error (mm)	Min ΔT obtained (°C)	Detectability
30	0.075	14.8	No
50	0.125	24.6	No
70	0.175	27.1	No
90	0.225	29.8	Maybe
110	0.275	51.2	Yes
130	0.325	54.6	Yes
150	0.375	67.2	Yes
170	0.425	79.1	Yes

5.3.1.3 Summary of Defects Detection in thin plates

Based on the results obtained for inhomogeneity defects in laser welding simulation for thin stainless steel plates, it can be concluded that, all the defects that are located at 1.25 mm depth (D1, D2, D3, and D4) from the surface, irrespective of their size, showed $\Delta T > \Delta T_{min}$ that can be recognized by the TIBWDD system. However, for defects that are located at a depth of 2.5 mm from the surface – D5, D6 D7 and D8, only defect D5 showed ΔT ≈ 79 °C which the TIBWDD system can detect. No trances of all other defects located at 3.75 mm depth, as $\Delta T < \Delta T_{min}$. For step misalignment defects, all plates with different error values, showed sufficient $\Delta T > \Delta T_{min}$ (based on minimum detectability limit). From the results for inclined misalignment defects, the minimum error value between the plates had to be at least 0.275 mm, so that ΔT obtained is 51.2 °C, which the TIBWDD system can detect. However, near the error value of 0.225mm,

the ΔT obtained (29.6 °C) is almost close to ΔT_{min} (30 °C), possibility for defect to be detected exist. No chances for detectability below error value of 0.225 mm as $\Delta T < \Delta T_{min}$.

5.3.2 Defect detection in thick plates

3D Gaussian heat source model is used for defect analysis in thick stainless steel plates of 15 mm, being the heat source model used in this defect detection analysis is proven valid for thick plates above 5 mm. All the boundary conditions – radiation and convection heat loss coefficients were similar to the conditions used for 2D heat source model. Based on the data specification sheet of IPG YLS 4000 [40], laser welding parameters optimized to attain proper welding temperatures for stainless steel plates of 15 mm are provided in Table 5-8. Fig. 5-32 shows the cross section of stainless steel plates near weld zone with moving 3D laser heat source based on the parameters given.

Table 5-8: Laser parameters for welding 15 mm thick SS plates

Parameter	Value
Power	1.75 kW
Welding Speed	6 mm/sec
Radius of beam	3 mm
Laser Specifications	1.07 µm, Infrared

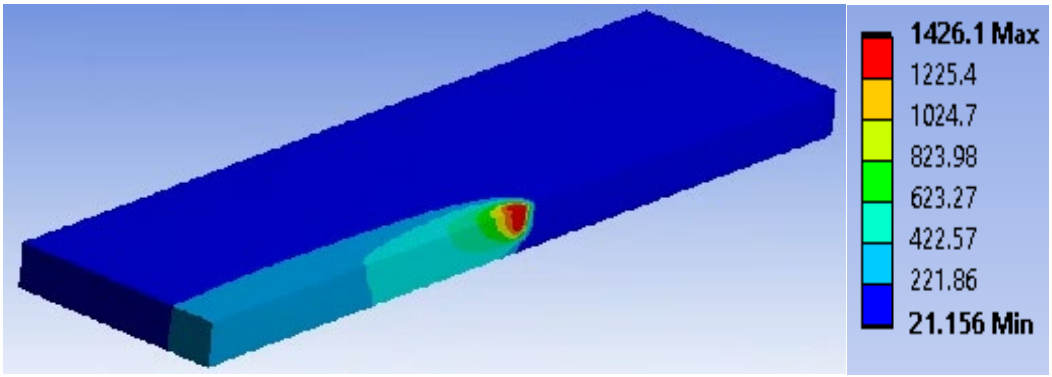

Figure 5-32: Moving 3D Gaussian heat source model on cross section of thick SS plates.

5.3.2.1 Material based Inhomogeneity defects

Inhomogeneous defects of different sizes were considered in thick stainless steel plates similar to thin plates. However, the size of these defects and their depths is varied and the parameters used in Chapter 4 for first set of defects were taken into account. A defect identification test was conducted with thick

plates, each of (200x50X15) mm in dimensions. Defects were introduced at the weld region as shown in Fig. 5-33 below. The dimensions and position of the defects at which they were placed is shown in Table 5-9 below.

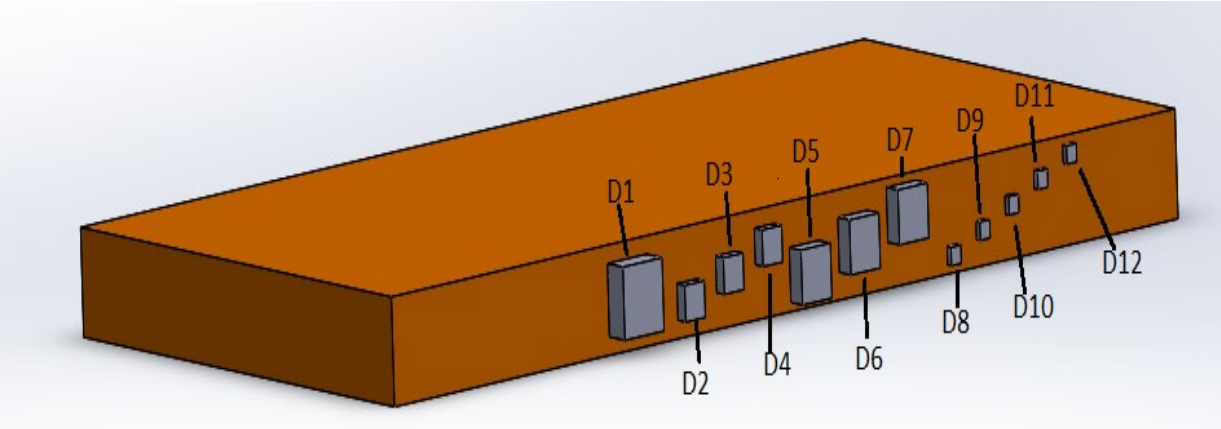

Figure 5-33: Position of various sized defects at the weld joint region of thick SS plates.

Table 5-9: Size of defects in thick SS plates.

Defects	Side length of the square defects (mm)	Location from the top surface (mm)
D1	10	2.5
D2	5	7.5
D3	5	5
D4	5	2.5
D5	7.5	6.25
D6	7.5	3.75
D7	7.5	1.25
D8	2.5	11.25
D9	2.5	8.75
D10	2.5	6.25
D11	2.5	3.75
D12	2.5	1.25

Simulations were also performed on stainless steel thick plates without any defects and temperature data was recorded on the surface of defect locations in both plate models and are compared. Fig. 5-34 shows

the temperature data on the surface location of defect D1 for thick plates with a data path of 20 mm placed symmetrically to defect location. It was clear that the largest defect D1 showed a temperature difference (ΔT) of 160.8 °C at 11.2 sec.

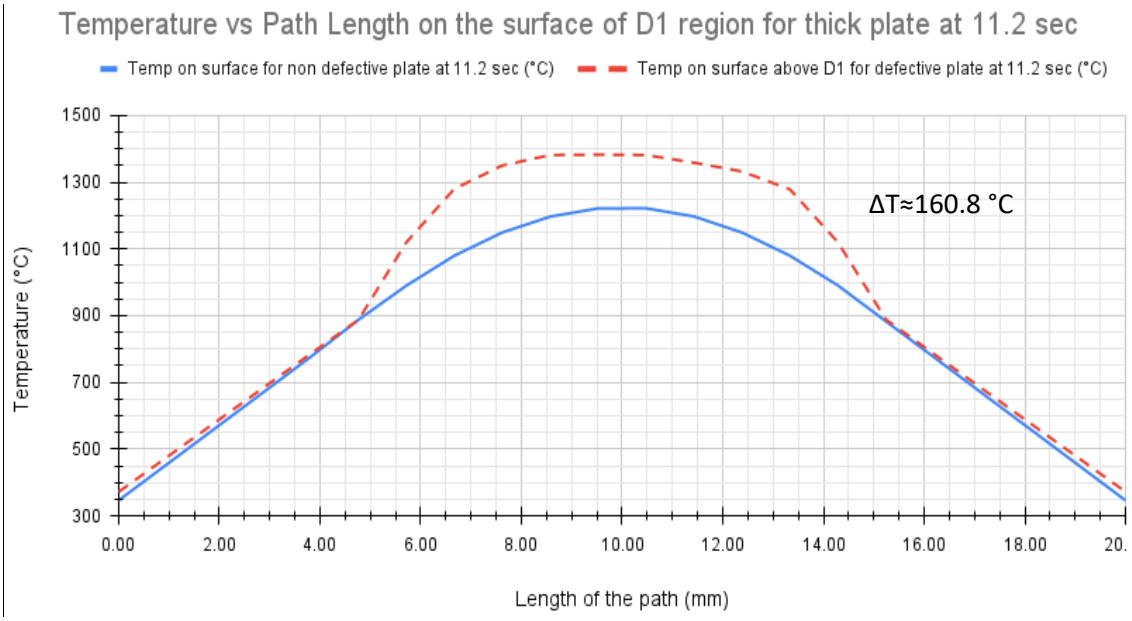

Figure 5-34: Temperature distribution graph between defective and non-defective plates on the surface above D1 at 11.2 sec.

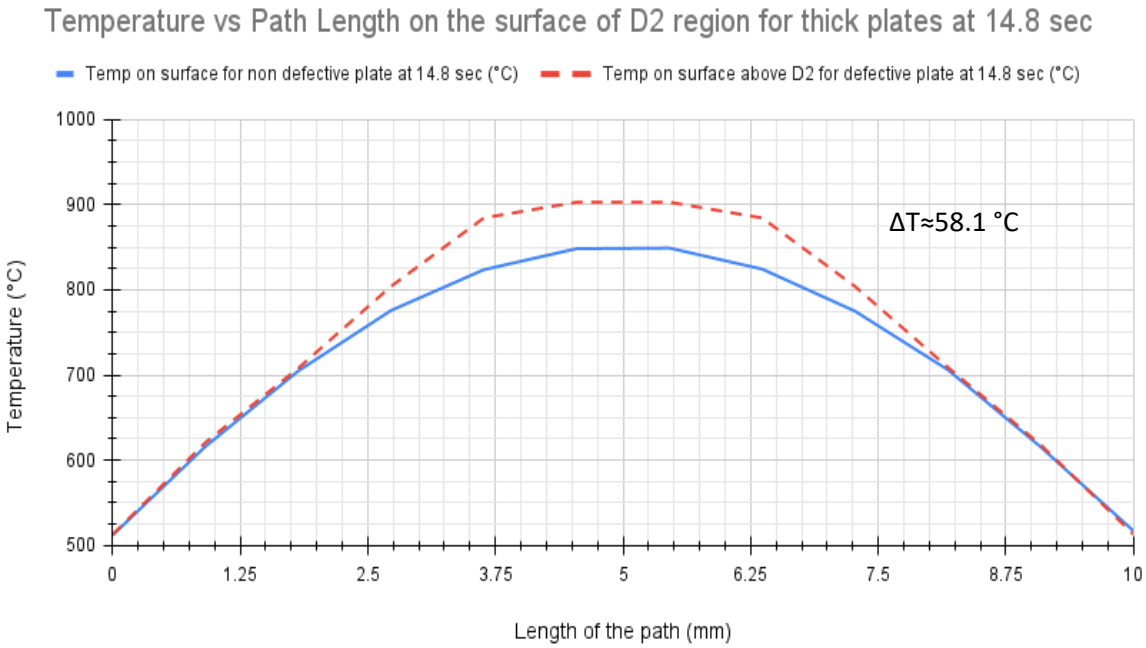

Figure 5-35: Temperature distribution graph between defective and non-defective thick plates on the surface above D2 at 14.8 sec.

From Fig. 5-35 and Fig. 5-36 for defects D2 and D3, it was clear that the deeper defect D2 showed a uniform ΔT on the surface rather than showing a clear contrast which is due to the higher heat transfer rate to the surrounding weld zone for defect D2. However, it can be understood that for deeper defects, their presence can be detected by the TIBWDD system, but not the exact geometrical shape. Also, there is a delay in time at which the defect D2 showed a temperature difference on the surface.

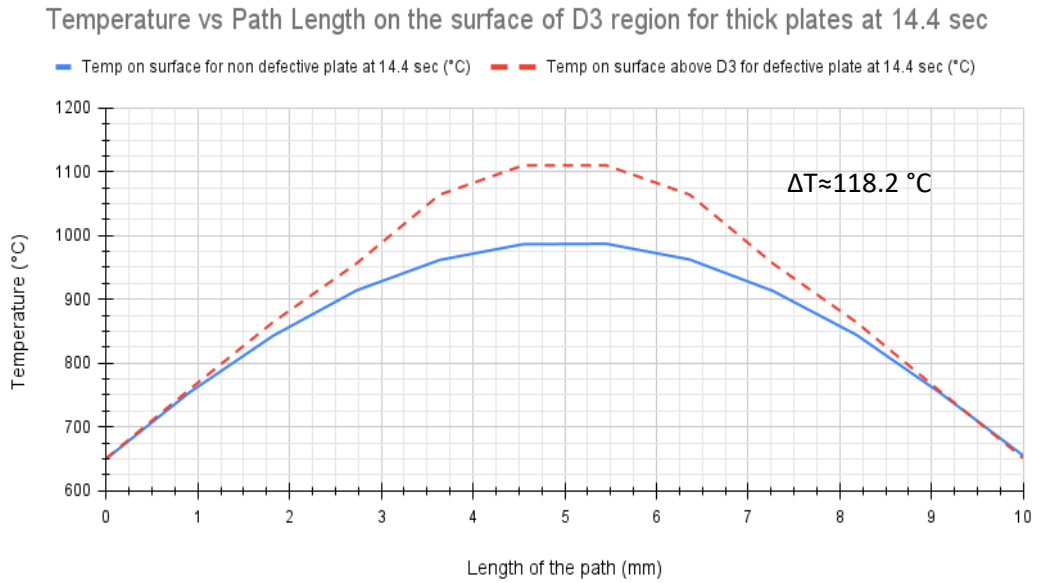

Figure 5-36: Temperature distribution graph between defective and non-defective plates on the surface above D3 at 14.4 sec.

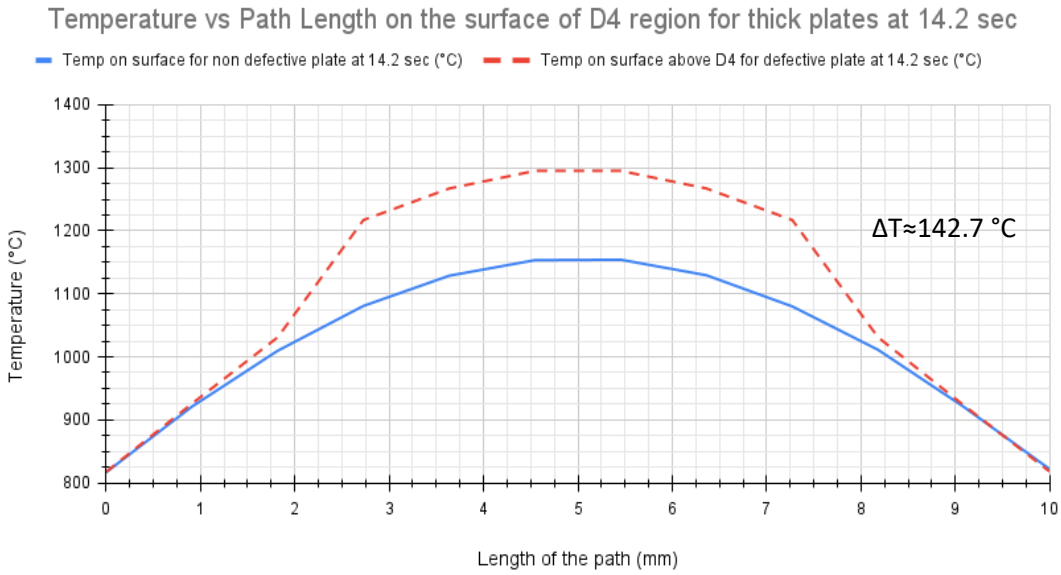

Figure 5-37: Temperature distribution graph between defective and non-defective plates on the surface above D4 at 14.2 sec.

From Fig. 5-37, defect D4, a 5 x 5 mm square defect, located at 2.5 mm from the surface showed a ΔT of 142.7°C. Moreover, this defect being closely located to the surface unlike D2 and D3, showed a clear difference in temperature along with its shape as this could be helpful for the TIBWDD system to find its accurate size unlike for D2. Even though defects D2, D3, and D4 are of same size, results showed that D4 can be detected relatively faster than D2 and D3, by the TIBWDD system as D4 is located deeper from the surface, hence there is a slight time delay for detection. Similarly, the temperature data along the path lines for all other defects were recorded along the welding time for every time step of 0.1 sec. The Table 5-10 below shows the maximum ΔT obtained on the surface at the respective time step during the weld joint cooling phase.

Table 5-10: Defect detection results using 3D Gaussian heat source for thick SS plates.

Defects	Time at which max ΔT was observed on surface (s)	ΔT between defective and non-defective plates(°C)	Detectability by TIBWDD Camera
D1	7.2	160.8	Yes
D2	13.4	58.1	Yes
D3	11.7	118.2	Yes
D4	10.4	142.7	Yes
D5	14.6	73.6	Yes
D6	14.2	121.6	Yes
D7	13.8	152.2	Yes
D8	20.2	2.4	No
D9	19.4	3.8	No
D10	18.9	6.2	No
D11	17.8	12.4	No
D12	17.6	32.4	Maybe

It was clear that the defects that are close to the surface irrespective of their sizes – D1, D4, and D7, except D12, showed sufficient ΔT to be recognized by the TIBWDD system. In case of D12, ΔT obtained (32.4 °C) ≈ ΔT_{min} (30 °C), so chances exist to be detectable. For all tiny defects (D8, D9, D10, D1), the ΔT obtained on surface is less the detectability limit (ΔT_{min}), so it would be hard for TIBWDD system to detect them.

5.3.2.2 Misalignment Defects

Similar to thin plate misalignment defect analysis, simulations had been performed on thick stainless steel plates with dimensions of (50 X 15 X 200) mm. Since misalignment defects were geometry-based defects and not material-based defects, tests had been performed to study if the results were similar to that thin plate analysis. This is to study if there is any influence of heat source model or welding parameters like speed, laser power, and beam radius; for creating a different temperature profile on the surface for defect detection.

1. Step Misalignment:

Simulations had been performed on thick SS plates, with four different step error values between the plates similar to thin plates. Table 5-11 shows the values of the different values of step misalignment errors. 3D Gaussian heat source model is simulated along the weld line with optimized laser welding parameters used in material-based defect study. Fig. 5-38 shows a step misalignment error of 2 mm for thick SS 304L plates.

Table 5-11: Misalignment defects in thick SS plates.

Misalignment models	Error Value
3D-SM-0.5	0.5 mm
3D-SM-1.0	1.0 mm
3D-SM-1.5	1.5 mm
3D-SM-2.0	2 mm

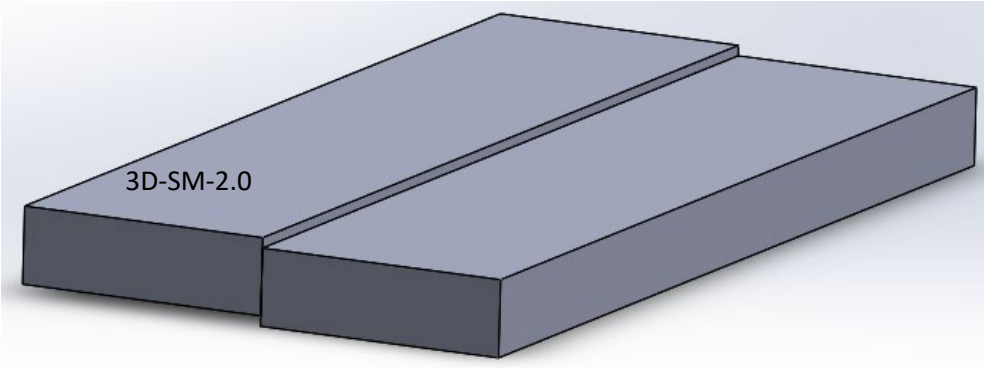

Figure 5-38: Step misalignment defect of 2 mm error along the weld region of thick SS plates.

Temperature data had been recorded using data paths on the surface of step misaligned plates at a distance of 60 mm from the start point. Fig. 5-39 shows the temperature distribution obtained on the surface of different misaligned plates.

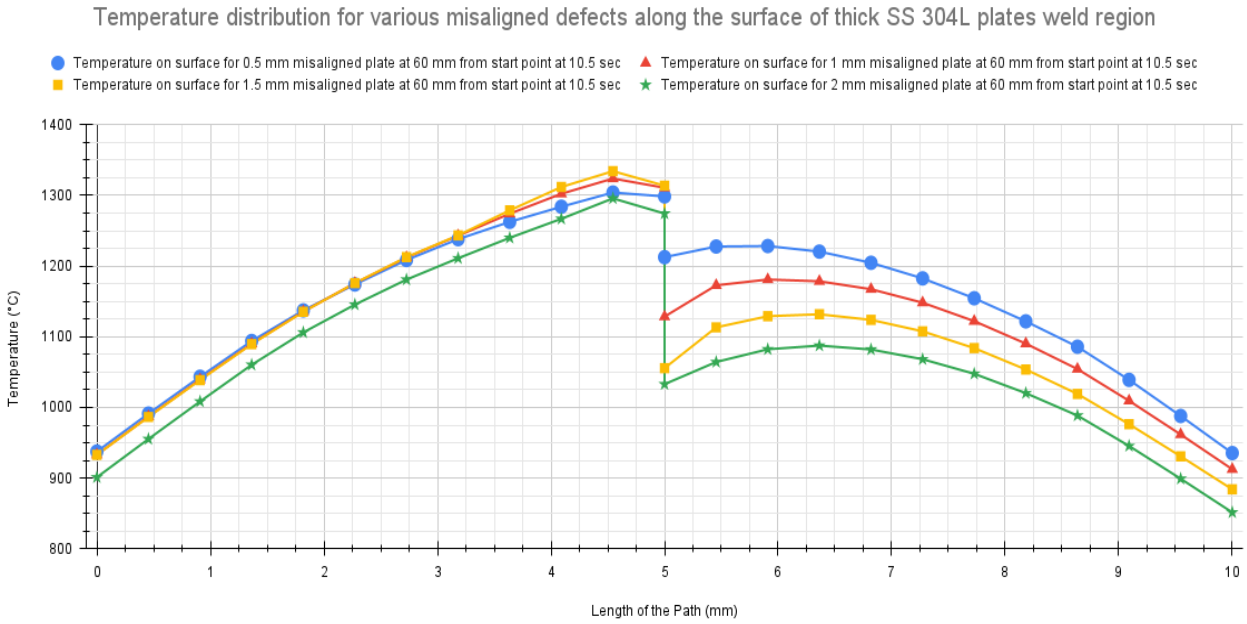

Figure 5-39: Temperature distribution of various step misaligned plates on weld surface of thick SS plates.

Based on the temperature data, the minimum ΔT observed neat weld zone is taken into consideration to evaluate if the TIBWDD system can detect them based on its sensitivity. Table 5-12 shows the minimum ΔT recorded on the surface and shows the extent of detectability. The results showed that all the different step misalignment defects can be easily detected by the TIBWDD system. However, in terms of minimum ΔT obtained on the surface for the IR camera to be able to detect, thick stainless steel plates showed a lower ΔT when compared to thin plates for step misalignment defects.

Table 5-12: Detectability of step misalignment defects in thick SS plates.

Misalignment models	Min ΔT (°C)	Detectability
3D-SM-0.5	70.1	Yes
3D-SM-1.0	129.4	Yes
3D-SM-1.5	182.1	Yes
3D-SM-2.0	187.4	Yes

2. Inclined Misalignment defects:

Similar tests had been conducted on thick plates with inclined step misalignment with an error from 0 mm to 0.5 mm to see at what deflection, noticeable ΔT can be observed on the plate surfaces. 3D Gaussian laser heat source model had been used for this study. Fig. 5-40 shows the inclined misalignment error in thick plates.

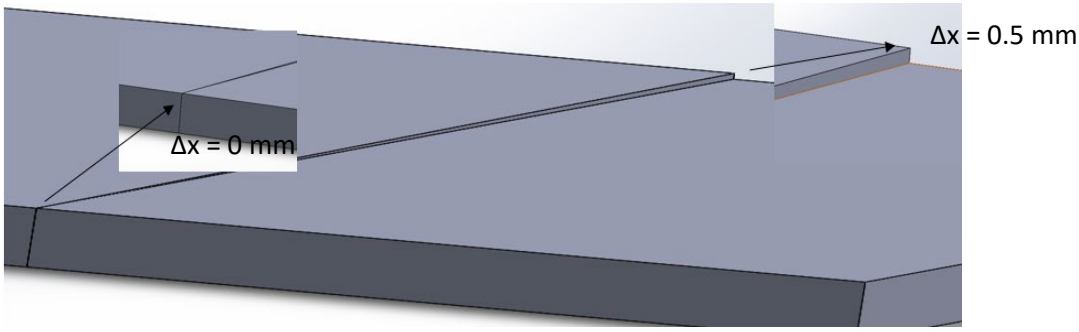

Figure 5-40: Inclined misalignment defect of 0.5 mm error along the weld region in thick SS plates.

Temperature data obtained will be recorded at the weld surface of the plates by the TIBWDD system at every 20 mm at respective time steps with 0.5-sec delay post welding from the start position using data paths. Fig. 5-41 shows the temperature data obtained on the surface of the inclined plates.

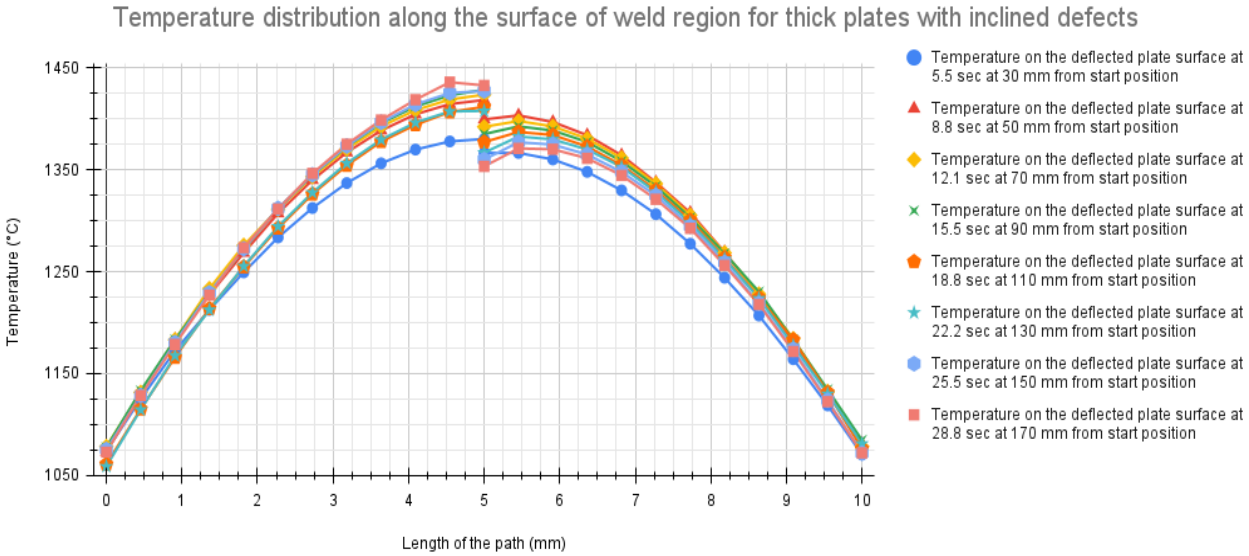

Figure 5-41: Temperature distribution curve of inclined misalignment defects on the surface of thick SS plates at various locations.

The ΔT created by the laser source when falling on inclined plates and considering the sensitivity of the TIBWDD system, the extent to which these defects can be detected is shown in Table 5-13.

Table 5-13: Detectability table for inclined misalignment defects for thick SS plates.

Distance from weld start region (mm)	Plate deflection error (mm)	Min ΔT obtained (°C)	Detectability
30	0.075	9.2	No
50	0.125	12.4	No
70	0.175	18.1	No
90	0.225	21.7	No
110	0.275	19.2	No
130	0.325	24.4	No
150	0.375	41.2	Yes
170	0.425	64.8	Yes

The results showed that for thick plates, sufficient ΔT required for the TIBWDD system did not obtained till deflection error of 0.375 mm, where ΔT obtained (41.2 °C) > ΔT_{min} (30 ° for 1500°).

5.3.2.3 Summary of Defects Detection in thick plates

In can be concluded that for inhomogeneous defects in thick plates, defects from D1 to D7 can be detected by the TIBWDD system as ΔT > ΔT_{min}. For the defects of size 2.5 mm (D8, D9, D10 and D11), except D12, showed ΔT < ΔT_{min}, which the TIBWDD system cannot detect. For defect D12 there is a probability to be detected as ΔT obtained (32.4 °C) ≈ ΔT_{min} (30 °C at 1500 °C).. For step misalignment defects, all defects showed sufficient ΔT > ΔT_{min} to be detectable by the TIBWDD system. Unlike thin plates where inclined misalignment defects were likely to be detected from an error of 0.225 mm, thick plates showed sufficient ΔT value of 41.2 °C till an error of 0.375 mm, is greater than the ΔT_{min} (30 °C), which can be detected by the TIBWDD system. This is because the welding speed is slower, and laser beam radius is larger for thick plates welding compared to thin plates, which results in uniform heat distribution and less ΔT on surface. Moreover, for thick plates welding, the 3D Gaussian model applies heat by volume along the depth unlike for thin plates where 2D Gaussian model is surface based. Therefore the heat flux applied using 3D heat source model is distributed uniform and it couldn't create much ΔT on the surface like thin plates.

Chapter 6. Summary, Main Conclusions, and Recommendations for Future Work

6.1 Summary

The use of IR Camera during online laser welding for obtaining metal temperature – emissivity (ε) correlations and its application for weld defect detection analysis was presented in this work. Three different materials – Stainless Steel (304L), Aluminum (AA 5154), and Low Carbon Steel (A 131 grade) with two different surface finishes – FM (0.25 μm), and RM (2.5 μm) were chosen as they are the most commonly encountered metals for continuous pipe laser welding. A test rig was built to incorporate an IR camera provided by industrial partner for finding temperature – ε correlations for these materials. Tests were conducted at every 50°C from 50°C – 550°C for Al samples and from 50°C – 800°C for SS and LCS samples. High temperature ceramic based emissivity coating was used and served two purposes. First, to act as a reference object of known emissivity (ε=1) and suppress the glare produced on sample surface due to lens. Second, to study the effect of the base material and its surface roughness on the ε produced by the coated surface. The temperature – emissivity data obtained for FM-SS sample is used an input to the IR camera. To assess defect detectability, experiments had been conducted on SS samples with two sets of defects based on δ (depth) and D_h (diameter). These defects have been chosen in discussion with the industrial partner. Numerical simulations for defect detectability using the same parameters and conditions were recreated to see if they can create a sufficient temperature drop on the surfaces that can be within camera detectability limits. Laser welding simulations were conducted using the same set of inhomogeneity defects considered in defect detectability work. Heat source models used for laser welding simulations are validated with numerical and experimental work done by D'Ostuni et al. [34]. Tests were conducted on thick and thin plates for three sets of defects – material based inhomogeneity, step

misalignment and inclined misalignment defects. Temperature data is recorded on plate surfaces during cooling period after welding and studied to identify the possible detectability of various defects based on the camera detectability limits and were presented accordingly.

6.2 Main Conclusions

The conclusion part for this report is divided into three points. The emissivity correlations work, experimental analysis for defect identification using IR camera, and numerical analysis for defect identification during laser welding simulations.

1. The experiments done in this thesis using a built test rig served three purposes. Firstly, temperature – emissivity data of different metals with different surface finishes were determined. Aluminum being the least emissive material due to its highly reflective nature, least change in emissivity was observed from 50°C to 550°C. For FM-Al sample on uncoated surface, the emissivity value showed a slow and consistent increase from 0.098 to 0.172 from 100°C – 550°C. Whereas for coated areas, the value dropped from 1.0 to 0.934 from 50 °C to 150 °C, and then rose to 0.993 till 550 °C. For the RM-Al sample on uncoated surface, emissivity constantly increased from 0.161 to 0.25 from 100°C – 550°C. Similar to FM-AL sample, emissivity over coated areas for RM-Al sample, decreased from 1.0 to 0.954 from 50°C to 150° and then showed a consistent increase till 550 °C where it reached 1.014. Similar results had been observed for stainless steel samples. For FM-SS sample, there is a consistent increase in emissivity from 0.155 to 0.329 from 50°C – 800°C on uncoated areas. Emissivity for coated areas on FM-SS sample decreased from 1.0 to 0.949 at 50 °C to 150 °C, and then showed a consistent increase till it reached 1.029 at 800 °C. The RM-SS sample, on uncoated areas, showed a change in emissivity from 0.178 to 0.369 from 100°C to 800°C, whereas for coated areas it decreased from 1 to 0.945 from 50 °C – 150 °C, and then increasingly reached 1.058 till 800 °C. On the contrary, a different trend had been observed in the case of low carbon steel. For the FM-LCS sample on uncoated areas, the

emissivity value was found to be 0.192 at 100°C, which slowly increased to 350°C to a value of 0.297. However, from 350°C to 550°C, the emissivity of FM-LCS rose steeply from 0.297 to 0.883 and then reached a value of 0.918 at 800 °C. This is due to the high tendency of iron atoms on the surface towards oxidation into ferric ions. As a result of exposure of these ferric atoms with air (oxygen atoms), they combine to form iron oxide (rust) which forms a matte black layer on the surface, which is the reason for high emissivity. For coated areas on FM-LCS sample, the emissivity steadily increased from 0.957 to 1.069 at 100 °C – 800°C. Similar results had been observed with the RM-LCS sample, but with a slightly higher emissivity. Collectively for all the materials based on the results, it can be concluded that the rough finished samples surface showed higher emissivity than fine samples surface. Equations had been developed to fit the emissivity data for all the materials with different surface roughness values. These equations can be used to find accurate ε values at any temperatures between 50°C to 550°C for fine and rough finish aluminum and from 50° to 800°C for both the surface finishes of stainless steel and low carbon steel. Secondly, room for improvement of IR camera's calibration for low carbon steel and stainless steel had been provided for the manufacturer. This was determined by using a high emissivity ceramic based paint provided as a reference object of known emissivity (ε=1). Based on the emissivity values obtained for low carbon steel and stainless steel samples on coated areas, it was found that ε value surpassed 1, which is impossible. The possible reason for this to happen had been studied and it can be result of two cases. First, the pre calibration work done using the IR camera is likely not very accurate and used a grey body (ε<1) as a reference object. Secondly, even though ε>1 is impractical, it can be possible when few particles are in relative isolation and are smaller than dominant's radiation wavelength [43]. Hence, the obtained coated surface emissivity results for low carbon steel and stainless steel can be used as a correction input by the manufacturer to the IR camera to increase its accuracy. Thirdly, based on the temperature – emissivity correlations obtained on coated areas for different materials, an interesting study on

influence of base metal and its surface roughness on the emissivity of a coated surface with a standard emissivity paint is observed. The results showed that the coated areas with rough finished base material exhibits more emissivity than fine finished base material. Coated areas on both FM-Al and RM-Al samples had ε=1 at 50°C, however, at 550°C FM-Al had ε=0.993, but RM-Al had ε=1.014. This difference in ε looks to be minimal, but had a great influence of temperature readings. Also the properties of the base material also had an influence on emissivity of coated surfaces. Both RM-SS and RM-LCS had ε=1 at 50°C on their coated areas, but at 800°C, RM-SS coated surface had ε=1.058 whereas RM-LCS showed higher value of ε=1.095.

2. The second and other important contribution through this work is assessing the use of IRT camera for defect identification in weld zone for real-time continuous pipe welding. Experimental and numerical analysis for defect detection was done on FM-SS samples that were used for emissivity correlation work. Two set of geometrical defects, first set – depth based (δ) and, second set – diameter based (D_h), were drilled into samples from the rear face and tested at the surface of front face for detectability. The emissivity curve obtained for FM-SS sample is used an input for IR camera for temperature measurement. From both experimental and simulation results, for first set of defects samples, the defects located closer to surface – D11 at 3 mm and D13 at 2 mm, both showed sufficient surface temperature drop (ΔT_{exp} & ΔT_{num}) > ΔT_{min} (detectability limit) and were recognized by the IR camera for both with glass wool and without glass wool. However, no traces of the deeper defects D12 and D21 was found as they were located at 4 mm from the surface, as the surface temperature drop recognized both numerically and experimentally (ΔT_{exp} and ΔT_{num}) is less than the camera detectability limit (ΔT_{min}) at subjected temperatures. From the experiments for second set of defects (D_h based) without glass wool, the defects of diameters 1.5 mm and 1.25 mm (WGW-D22 and WGW-D23) showed a sufficient temperature drop ΔT_{exp} (31 °C and 17 °C respectively) that were greater than ΔT_{min} (15.7 °C) required. From simulation results for second set of defects without glass wool, only

defect D22 showed sufficient ΔT_{num} (26.3 °C) > ΔT_{min} (15.7 °C). No traces of D21 and D23 as ΔT_{num} < ΔT_{min}. Whereas for D_h based defects with glass wool, only defect of diameter 1.5 mm (GW-D22) showed sufficient surface temperature drop both numerically and experimentally (ΔT_{exp} & ΔT_{num}) > ΔT_{min} that was detected by IR camera. No traces of other defects as ΔT_{exp} and ΔT_{num} obtained for them are less than ΔT_{min} required. Both experimental and numerical results obtained for studying surface temperature drop on defect samples were in close agreement as maximum temperature deviation between numerical and experimental data (ΔT_{en}) is < 10°C.

3. These set of defects which were assessed and validated before was introduced into stainless steel plates for laser welding simulations for defects assessment analysis for improving weld quality. The emissivity curve obtained experimentally for FM-SS sample was extrapolated till 1450°C and used as a radiation boundary condition for welding analysis. Simulations were performed based on two plate scenarios – thin plates (5 mm in thickness) and thick plates (15 mm in thickness). In this regard, two different moving laser heat source models, 2D and 3D heat source models, were developed based on Gaussian distribution. These results for both 2D and 3D laser heat sources had been validated with the numerical and experimental results provided by D'Ostuni et al. [34]. Then based on welding stainless steel plates, parameters had been chosen from the specification data book of the IPG Photonics YLS 4000-CUT welding machine and optimized accordingly. The weld defect assessment for thin and thick stainless steel plates is as follows:
    i. Material based Inhomogeneity Defects: For thin plates, four different sizes of square defects located at different depths of 1.25mm, 2.5mm, and 3.75 mm from the surface were studied for detectability. Defects located close to the surface within 1.25 mm had shown good ΔT value for detectability with the TIBWDD system. Whereas, defects located at 2.5 mm and 3.75 mm from the surface weren't captured by the TIBWDD system except for defect D5 which showed sufficient ΔT (79°C) > ΔT_{min} (30 °C) which can be captured with the TIBWDD system.

For thick plates, all the defects from D1 to D7 showed $\Delta T > \Delta T_{min}$ that can be detected by the TIBWDD system. For defects of 2.5 mm in square size (D8, D9, D10 and D11), except D12 showed $\Delta T < \Delta T_{min}$ that can detected by TIBWDD system. For defect D12, ΔT obtained on the surface (32.4 °C) is very close to the detectability limit (30 °C), so detectability for D12 is not clear.

ii. Step Misalignment Defects: For both thin and thick plates, all four different errors showed a feasible ΔT value on the surface that can be detected by the TIBWDD system. For instance, thin plates with a 1.5 mm step error showed ΔT = 241.5 °C, whereas in the case of thick plates ΔT = 182.1°C, yet sufficient for the camera to detect. The possible reason for this could be the use of different heat source models. For thin plates, 2D Gaussian model used, is a surface based model where heat flux is applied along surface and does not consider depth. Whereas, for thick plates welding, 3D Gaussian model applies volumetric heat flux considering the depth of laser source at weld region, allowing heat to be distributed evenly and causing less ΔT on surface. Moreover for thick plates welding, the welding speed is slower and laser beam radius is larger, hence allowing more time for heat flux to be distributed evenly which causes less ΔT obtained on surface.

iii. Inclined Misalignment Defects: For thin plates, defect were able to be captured only when the minimum defection error between the stainless steel plates is at least 0.275 mm (ΔT=51.2 °C). For thick plates, they seem to not detectable by the TIBWDD system at least when the deflection error is 0.375 mm (ΔT=41.2 °C). So in this regard, when the TIBWDD system can identify these misalignments in plates, they can send a feedback to the welding system, so that the feed rollers can be adjusted to overcome these issues during continuous pipe welding process.

6.3 Future Recommendations

In this work, calculation of emissivity graph for Al had been done for its entire working temperature scale 50°C – 550°C. However, for LCS and SS samples used in this work, experiments had been conducted only till 800°C due to the limited range of heating cartridges used, and then the results had been extrapolated till their meting temperatures i.e. 1450°C. The primary reason for choosing these cartridges is because they are relatively convenient and inexpensive when compared to other heating methods like induction or infrared heaters. Also, these cartridges were only rated to 800°C and if heated more, they can burn out and damage the setup and test samples. In this connection, further work can be done experimentally using other methods like induction heating to evaluate emissivity for the entire working temperature scale for these metals. Secondly, no laser welding experiments had been performed in this work to assess material and geometry based defects. It would be a good area to research for evaluating material based inhomogeneity defects experimentally. However material-based defects are formed naturally and cannot be created manually, so it would be challenging to produce these defects during experiments.

References

[1] https://www.biologicaldiversity.org/campaigns/americas_dangerous_pipelines/

[2] https://helcom.fi/media/publications/BRISK-BRISK-RU_SummaryPublication_spill_of_oil.pdf

[3] https://www.energyvoice.com/oilandgas/americas/112313/conocophillips-pipeline-spill-near-wildlife-habitat-alberta/

[4] https://www.petrosadid.com/piping/pipe_tube/tubes_manufacturing_process.php

[5] https://muckymariners.com/meo-class-4-subjects/function-4b-meol/auxiliary-machines/2-welding-ndt/welding-ndt-5-12-welding-defects/

[6] http://www.sunnysteel.com/stainless-pipes-tubes.php

[7] https://www.xiris.com/xiris-wi-3000/

[8] https://www.optris.global/optris-xi-400

[9] Maldague, Xavier. (2000). Applications of Infrared Thermography In Nondestructive Evaluation. Trends Opt. Nondestructive Testing. 10.1016/B978-008043020-1/50040-5.

[10] Tse P., “Advancement in Condition Monitoring and Its Management”, Proceedings of the Building Management Systems: Modern Application, Education and Training Developments in China(Mainland), Hong Kong and Macau, Paper 12-1, Nov. 24, 2009, Hong Kong.

[11] Tse P. and Wang X., “Application of ultrasonic guided waves for quantitative characterization of defects in pipeline”, International Conference on Utility Management and Safety (ICUMAS), March 1-4, 2009, Hong Kong, pp. 247-252.

[12] Barreira, Eva & Bauer, Elton & Mustelier, N & Freitas, (2015). Measurement of materials emissivity – Influence of the procedure.

[13] Chang-Da. Wen and I. Mudawar, "Modelling the Effects of Surface Roughness on the Emissivity of Aluminum Alloys," *International Journal of Heat and Mass Transfer*, vol. 49, no. 23-24, pp. 4279-4289, 06/07/2006.

[14] Liu, Y.F., Hu, Z.L., Shi, D.H. *et al.* Experimental Investigation of Emissivity of Steel. *Int J Thermophys* **34,** 496–506 (2013). https://doi.org/10.1007/s10765-013-1421-3.

[15] H. Wang et al. "Measurement technology for material emissivity under high temperature dynamic heating conditions," *Measurement*, vol. 46, no. 10, pp. 4023-4031, 12/08/2013.

[16] U. Sreedhar, C.V. Krishnamurthy, Krishnan Balasubramaniam, V.D. Raghupathy, S. Ravisankar, Automatic defect identification using thermal image analysis for online weld quality monitoring, Journal of Materials Processing Technology, Volume 212, Issue 7, 2012, Pages 1557-1566, ISSN 0924-0136, https://doi.org/10.1016/j.jmatprotec.2012.03.002.

[17] Washer G, Connor R, Looten D. Performance Testing of Inspectors to Improve the Quality of Nondestructive Testing. *Transportation Research Record*. 2014; 2408(1):107-113. Doi:10.3141/2408-12

[18] Shen, Gongtian & Li, Tao. (2007). Infrared thermography for high-temperature pressure pipe. Insight. 49. 151-153. 10.1784/insi.2007.49.3.151.

[19] K. Schaumberger, M. Beck, J. Saffer, F. Kaufmann, J. Ermer, S. Roth, M. Schmidt, Improving process reliability by means of detection of weld seam irregularities in copper via thermographic process monitoring, Procedia Manufacturing, Volume 36, 2019, Pages 58-63, ISSN 2351-9789, https://doi.org/10.1016/j.promfg.2019.08.009.

[20] Venkatraman, B., M. Menaka, M. Vasudevan, and Baldev Raj. "Thermography for online detection of incomplete penetration and penetration depth estimation." In *Proceedings of Asia-Pacific Conference on NDT*. 2006.

[21] Ranjit, S., Kang, K. & Kim, W. Investigation of lock-in infrared thermography for evaluation of subsurface defects size and depth. *Int. J. Precis. Eng. Manuf.* **16,** 2255–2264 (2015). https://doi.org/10.1007/s12541-015-0290-z.

[22] Goldak, J., Chakravarti, A. & Bibby, M. A new finite element model for welding heat sources. *Metall Mater Trans B* **15,** 299–305 (1984). https://doi.org/10.1007/BF02667333.

[23] Capriccioli, Andrea & Frosi, Paolo. (2009). Multipurpose ANSYS FE procedure for welding processes simulation. Fusion Engineering and Design. 84. 546-553. 10.1016/j.fusengdes.2009.01.039.

[24] Prasad, V.M. & Varghese, V. & Suresh, M. & Kumar, (2016). 3D Simulation of Residual Stress Developed During TIG Welding of Stainless Steel Pipes. Procedia Technology. 24. 364-371. 10.1016/j.protcy.2016.05.049.

[25] Dean Deng, HidekazuMurakawa, Numerical simulation of temperature field and residual stress in multi-pass welds in stainless steel pipe and comparison with experimental measurements, Journal of Computational Materials Science 37, 2006, p. 269 – 277.

[26] Mr. Suresh Akella, Mr. Vemanaboina Harinadh, Mr. Yaggadi Krishna, and Mr. Ramesh Kumar Buddu. "A Welding Simulation of Dissimilar Materials SS304 and Copper" Procedia Materials Science, vol. 5, 2014. doi:10.1016/j.mspro.2014.07.490.

[27] Nikanorov, A.; Baake, E.; Brauer, H.; Weil, C.: Approaches for Numerical Simulation of High Frequency Tube Welding Process. International Conference on Heating by Electromagnetic Sources 2013 (HES-13), May 22nd-24th 2013.

[28] https://www.mitutoyo.com/wp-content/uploads/2015/08/Surftest_SJ210.pdf

[29] https://www.aremco.com/wp-content/uploads/2018/05/A05_S2_18_Emissivity.pdf

[30] Frederick O. Bartell, "Cavity Emissivities Greater Than One," Proc. SPIE 0520, Thermosense VII: Thermal Infrared Sensing for Diagnostics and Control, (20 March 1985).

[31] Kim, Choong S. *Thermophysical properties of stainless steels*. No. ANL-75-55. Argonne National Lab., Ill. (USA), 1975.

[32] Guo-ming, Han et al. “Dynamic simulation of the temperature field of stainless steel laser welding.” *Materials & Design* 28 (2007): 240-245.

[33] Milan Turňa, Bohumil Taraba, Petr Ambrož, Miroslav Sahul, Contribution to Numerical Simulation of Laser Welding, Physics Procedia, Volume 12, Part A, 2011, Pages 638-645, ISSN 1875-3892, https://doi.org/10.1016/j.phpro.2011.03.080.

[34] K R, Balasubramanian & Shanmugam, N. & Naidu, Buvanashekaran.G & Sankaranarayanasamy, (2008). Numerical and Experimental Investigation of Laser Beam Welding of AISI 304 Stainless Steel Sheet. Advances in Production Engineering & Management. 3. 93-105.

[35] Kim, K., Lee, J. & Cho, H. Analysis of pulsed Nd:YAG laser welding of AISI 304 steel. *J Mech Sci Technol* **24,** 2253–2259 (2010). https://doi.org/10.1007/s12206-010-0902-6.

[36] Kumar, P., Sinha, A.N. Studies of temperature distribution for laser welding of dissimilar thin sheets through finite element method. *J Braz. Soc. Mech. Sci. Eng.* **40,** 455 (2018). https://doi.org/10.1007/s40430-018-1380-5.

[37] Jayanthi, A., K. Venkatramanan and K. S. Kumar. “MODELING AND SIMULATION FOR WELDING OF AISI 316 L STAINLESS STEELS USING PULSED Nd : YAG LASER.” (2017).

[38] Zeng, Z.; Li, X.; Miao, Y.; Wu, G.; Zhao, Z. Numerical and experiment analysis of residual stress on magnesium alloy and steel butt joint by hybrid laser-TIG welding. Comput. Mater. Sci. 2011, 50, 1763–1769.

[39] D’Ostuni, Sonia; Leo, Paola; Casalino, Giuseppe. 2017. "FEM Simulation of Dissimilar Aluminum Titanium Fiber Laser Welding Using 2D and 3D Gaussian Heat Sources" *Metals* 7, no. 8: 307. https://doi.org/10.3390/met7080307.

[40] https://www.gophotonics.com/products/lasers/ipg-photonics/29-152-yls-4000.

[41] Srivatsava, A. *Moving Heat Source ACT Extension*. Ansys Inc. 26 February 2016.

[42] https://youtu.be/1aFCljGagpE.

[43] V. A. Golyk, M. Krüger, and M. Kardar, "Heat radiation from long cylindrical objects," Phys. Rev. E 85(4), 046603 (2012).